МИНИСТЕРСТВО НАУКИ И ВЫСШЕГО ОБРАЗОВАНИЯ РОССИЙСКОЙ ФЕДЕРАЦИИ
ФЕДЕРАЛЬНОЕ ГОСУДАРСТВЕННОЕ АВТОНОМНОЕ ОБРАЗОВАТЕЛЬНОЕ УЧРЕЖДЕНИЕ
ВЫСШЕГО ОБРАЗОВАНИЯ
«НАЦИОНАЛЬНЫЙ ИССЛЕДОВАТЕЛЬСКИЙ ЯДЕРНЫЙ УНИВЕРСИТЕТ «МИФИ»
(НИЯУ МИФИ)

Отчет о «Научно-исследовательской деятельности аспиранта и подготовке к защите диссертации на соискание ученой степени кандидата наук» за шестой семестр

«Исследование физических оснований и космомикрофизических проявлений моделей асимметричной скрытой массы»

Аспирант — Д. О. Сопин
Научная специальность — 1.3.15 «Физика атомных ядер и элементарных частиц, физика высоких энергий»

Научный руководитель, д.ф.-м.н., проф. _____ М. Ю. Хлопов

Москва 2026

ОГЛАВЛЕНИЕ

1 ВВЕДЕНИЕ

По данным коллаборации PLANCK [1] относительная энергетическая плотность вещества во Вселенной составляет $\Omega_m = 0.315$. При этом барионная плотность оказывается значительно меньше данной величины: $\Omega_b = 0.0493$. Существование скрытой массы (англ. «hidden mass» или «dark matter», сокращённо — DM), объясняющее столь существенную разницу, подтверждается многочисленными наблюдениями и астрофизическими данными, однако природа и динамические характеристики DM остаются неустановленными. Таким образом, как экспериментальные поиски, так и теоретическое изучение кандидатов на роль частиц-переносчиков скрытой массы по-прежнему исключительно **актуальны**.

На сегодняшний день предложено множество моделей, претендующих на решение данной проблемы. Одной из них является модель тёмных атомов в виде X-гелия ($X^{-2n}(He^{+2})_n$). Составные частицы данного типа должны возникать в ряде расширений СМ, предсказывающих формирование стабильных тяжёлых состояний X^{-2n}.

Тёмные атомы должны формироваться на этапе нуклеосинтеза путём последовательного захвата лёгких ядер тяжёлыми частицами. Новые процессы могут значительно повлиять на состав первичной плазмы. Возможность формирования в этих условиях аномальных изотопов и перепроизводства лития [2] представляет серьёзную проблему для рассматриваемой модели. В то же время возникающие вследствие взаимодействия двух тёмных атомов молекулоподобные структуры не изучены и также могут представлять интерес.

Целью данной работы является построение модели формирования тёмных атомов на ранних этапах эволюции Вселенной. Для её достижения необходимо решить несколько теоретических **задач**:

- Разработать модель внутреннего строения тёмных атомов, позволяющую выявить стабильные соединения и определить их энергетические

параметры.

- Составить карту ядерных реакций с участием тёмных атомов и определить их скорости при заданных температурах.
- Найти зависимость концентраций частиц, составляющих первичную плазму, от температуры.

Таким образом, **в перспективе** данное исследование должно дать описание механизмов возникновения скрытой массы в форме X-гелия. Также в ходе работы могут быть получены теоретические ограничения на существование многозарядных частиц X^{-2n}. **Научная новизна** исследования определяется отсутствием на текущий момент такого рода описания.

Представленный далее текст отчёта разделён на несколько глав. В главе 2 представлены результаты модельно независимого рассмотрения сфалеронных переходов. С их использованием проведено более глубокое исследование рассмотренных ранее моделей. Найдены ограничения на массу, соответствующие современным данным по лептонной асимметрии. В главе **??** описывается расчёт скорости реакций процесса нейтрализации тёмных атомов. Обсуждаются некоторые особенности модифицированного первичного нуклеосинтеза, предсказываемые моделью. В Приложении представлен список публикаций за 6 семестр. Тексты статей приложены.

2 МНОГОЗАРЯДНЫЕ ЧАСТИЦЫ

Для определения связи между возможными концентрациями частиц-переносчиков скрытой массы и их массой необходимо изучить особенности закалки сфалеронных переходов с учётом данных о лептонной асимметрии [3]:

$$\left|\frac{L}{B}\right| = \left|\frac{n_l - n_{\bar{l}}}{n_b - n_{\bar{b}}}\right| < 6.67 \cdot 10^6. \tag{2.1}$$

Для всех расширений Стандартной Модели (СМ) могут быть выписаны уравнения для плотностей барионного и лептонного чисел:

$$B = (10 + 2\sigma_t)\mu_{uL} + 6\mu_W, \tag{2.2}$$

$$L = 4\mu + 6\mu_W, \tag{2.3}$$

где μ_{uL}, μ_W и μ —химические потенциалы, соответственно, стандартных левого u-кварка, W^- бозона и трёх левых нейтрино: $\mu = \sum\limits_i \mu_{\nu_i L}$. Химический потенциал бозона Хиггса в нарушенной фазе $\mu_0 = 0$.

Все аналогичные уравнения сводятся к линейной комбинации химических потенциалов стабильной частицы и W^- бозона с коэффициентами, также являющимися линейными комбинациями весовых функций $\sigma\left(\frac{m}{T_*}\right)$. Как следствие, полная система уравнений разделяется на две подсистемы. Первая

$$\begin{pmatrix} a_{BB} & 0 & 0 & 0 & b_{BW} \\ 0 & a_{LL} & 0 & 0 & b_{LW} \\ 0 & 0 & a_{B'B'}\sigma_{B'} & 0 & b_{B'W}\sigma_{B'} \\ 0 & 0 & 0 & a_{L'L'}\sigma_{L'} & b_{L'W}\sigma_{L'} \\ c_{QB} & c_{QL} & c_{QB'}\sigma_{B'} & c_{QL'}\sigma_{L'} & d_1\sigma_{B'} + d_2\sigma_{L'} + d_3 \end{pmatrix} \cdot \begin{pmatrix} \mu_B \\ \mu_L \\ \mu_{B'} \\ \mu_{L'} \\ \mu_W \end{pmatrix} = \begin{pmatrix} B \\ L \\ B' \\ L' \\ 0 \end{pmatrix}, \tag{2.4}$$

где B' и L' — плотности новых барионного и лептонного чисел, $\{\sigma_j\}$ обозначает множество весовых функций, коэффициенты a_{ij}, b_{ij}, c_{ij} и d_k — числа,

первый индекс отражает тип уравнения, второй —химический потенциал, перед которым он стоит. Она позволяет исключить все химические потенциалы.

В более общем виде:

$$\begin{pmatrix} a_{11} & 0 & 0 & \cdots & 0 & b_1 \\ 0 & a_{22} & 0 & \cdots & 0 & b_2 \\ 0 & 0 & a_{33} & \cdots & 0 & b_3 \\ \vdots & \vdots & \vdots & \ddots & \vdots & \vdots \\ 0 & 0 & 0 & \dots & a_{n-1,n-1} & b_{n-1} \\ c_1 & c_2 & c_3 & \cdots & cn-1 & d \end{pmatrix} \cdot \begin{pmatrix} \mu_1 \\ \mu_2 \\ \mu_3 \\ \vdots \\ \mu_{n-1} \\ \mu_n \end{pmatrix} = \begin{pmatrix} A_1 \\ A_2 \\ A_3 \\ \vdots \\ A_{n-1} \\ 0 \end{pmatrix}, \tag{2.5}$$

где веса включены в коэффициенты. Её решения

$$\mu_i = \frac{A_i}{a_{ii}} + \frac{b_i}{a_{ii}} \frac{\sum\limits_{j=1}^{n-1} \frac{c_j}{a_{jj}} A_j}{d - \sum\limits_{j=1}^{n-1} \frac{c_j}{a_{jj}} b_j}, \qquad \mu_n = -\frac{\sum\limits_{j=1}^{n-1} \frac{c_j}{a_{jj}} A_j}{d - \sum\limits_{j=1}^{n-1} \frac{c_j}{a_{jj}} b_j} \tag{2.6}$$

Сфалеронное уравнение $\sum s_i \mu_i = 0$ может быть представлено как

$$\sum_{i=1}^{n-1} \frac{1}{a_{ii}} \left(s_i d - s_n c_i + \sum_{j=1}^{n-1} \frac{b_j}{a_{jj}} \left(s_j c_i - c_j s_i \right) \right) \cdot A_i = 0, \tag{2.7}$$

или переписано в форме

$$\begin{aligned} &(f_{1B}\sigma_{B'} + f_{2B}\sigma_{L'} + f_{3B})B + (f_{1L}\sigma_{B'} + f_{2L}\sigma_{L'} + f_{3L})L + \\ &+ \frac{1}{\sigma_{B'}}(f_{1B'}\sigma_{B'} + f_{2B'}\sigma_{L'} + f_{3B'})B' + \frac{1}{\sigma_{L'}}(f_{1L'}\sigma_{B'} + f_{2L'}\sigma_{L'} + f_{3L'})L' = 0, \end{aligned} \tag{2.8}$$

где f_{ij} — численные коэффициенты. Отличие в коэффициентах перед стандартными и новыми плотностями чисел приводит к тому, что отношение плотностей L'/B' слабо зависит от L/B.

В наиболее же удобной форме:

$$\frac{B'}{B}+\frac{\frac{1}{a_{44}}\left(\sum\limits_{j=1}^{4}\frac{b_j}{a_{jj}}\begin{vmatrix}c_4 & s_4\\ c_j & s_j\end{vmatrix}-\begin{vmatrix}c_4 & s_4\\ d & s_5\end{vmatrix}\right)}{\frac{1}{a_{33}}\left(\sum\limits_{j=1}^{4}\frac{b_j}{a_{jj}}\begin{vmatrix}c_3 & s_3\\ c_j & s_j\end{vmatrix}-\begin{vmatrix}c_3 & s_3\\ d & s_5\end{vmatrix}\right)}\frac{L'}{B}=$$
$$=-\frac{\frac{1}{a_{22}}\left(\sum\limits_{j=1}^{4}\frac{b_j}{a_{jj}}\begin{vmatrix}c_2 & s_2\\ c_j & s_j\end{vmatrix}-\begin{vmatrix}c_2 & s_2\\ d & s_5\end{vmatrix}\right)}{\frac{1}{a_{33}}\left(\sum\limits_{j=1}^{4}\frac{b_j}{a_{jj}}\begin{vmatrix}c_3 & s_3\\ c_j & s_j\end{vmatrix}-\begin{vmatrix}c_3 & s_3\\ d & s_5\end{vmatrix}\right)}\left(\frac{L}{B}+\frac{\frac{1}{a_{11}}\left(\sum\limits_{j=1}^{4}\frac{b_j}{a_{jj}}\begin{vmatrix}c_1 & s_1\\ c_j & s_j\end{vmatrix}-\begin{vmatrix}c_1 & s_1\\ d & s_5\end{vmatrix}\right)}{\frac{1}{a_{22}}\left(\sum\limits_{j=1}^{4}\frac{b_j}{a_{jj}}\begin{vmatrix}c_2 & s_2\\ c_j & s_j\end{vmatrix}-\begin{vmatrix}c_2 & s_2\\ d & s_5\end{vmatrix}\right)}\right) \tag{2.9}$$

Из этого выражения видно, например, что выбором разности масс между новыми барионной и лептонной составляющими можно подавить (или усилить) коэффициент $\gamma(\sigma_i)$, стоящий перед L'/B за счёт $\frac{a_{33}}{a_{44}} \sim \frac{\sigma_{B'}}{\sigma_{L'}}$. В частности, при $m_{L'} < m_{B'}$: $\gamma(\sigma_i) \to 0$ быстрее, чем σ_i. Правая же часть равенства подавляется множителем $\sigma_{B'}$.

Дополнительные уравнения, получаемые из условий на химические потенциалы будут однородны и линейны по плотностям чисел.

Последним уравнением второй подсистемы является условие отношения энергетических плотностей:

$$\sum_{i=3}^{n-1}\frac{m_i}{m_b}\left|\frac{A_i}{B}\right|=\frac{\Omega_{DM}}{\Omega_b}. \tag{2.10}$$

В случае $n-1=4$, т.е двухкомпонентного сценария,скрытая масса почти полностью обеспечивается более лёгкой, в то время как тяжёлая в большей степени связана с отношением L/B.

Действительно, решая его в общем виде получаем:

$$\left(1\pm_{L'}\mp_{B'}\frac{m_{B'}}{m_{L'}}\frac{\sigma_{B'}}{\sigma_{L'}}\gamma'\right)\frac{B'}{B}=-\alpha'\sigma_{B'}\left(\frac{L}{B}+\beta\right)\mp_{L'}\frac{m_b}{m_{L'}}\frac{\sigma_{B'}}{\sigma_{L'}}\frac{\Omega_{\rm DM}}{\Omega_b}, \tag{2.11}$$
$$\frac{L'}{B}=\pm_{L'}\left(\frac{m_b}{m_{L'}}\frac{\Omega_{\rm DM}}{\Omega_b}\mp_{B'}\frac{m_{B'}}{m_{L'}}\frac{B'}{B}\right), \tag{2.12}$$

где знаки $\pm_i$ соответствуют знакам соответствующих отношений плотно-

стей, $\mp_i$ — противоположны им, $\alpha(\sigma_i) = \alpha'\sigma_{B'}$ и $\gamma(\sigma_i) = \gamma'\frac{\sigma_{B'}}{\sigma_{L'}}$. При $m_{B'} > m_{L'}$ функция $\frac{\sigma_{B'}}{\sigma_{L'}} \to 0$, быстрее всех и наоборот становится доминирующим слагаемым при $m_{B'} < m_{L'}$. Потому

$$\frac{B'}{B} \to \begin{cases} -\alpha'\sigma_{B'}\left(\frac{L}{B} + \beta\right), & \\ \pm_{B'}\frac{m_b}{m_{B'}}\frac{\Omega_{\text{DM}}}{\Omega_b}, & \end{cases} \qquad \frac{L'}{B} \to \begin{cases} \pm_{L'}\frac{m_b}{m_{L'}}\frac{\Omega_{\text{DM}}}{\Omega_b}, & m_{B'} \gg m_{L'} \\ -\alpha'\sigma_{L'}\left(\frac{L}{B} + \beta\right), & m_{B'} \ll m_{L'} \end{cases} \tag{2.13}$$

В случае же равных масс $\frac{\sigma_{B'}}{\sigma_{L'}} \sim 1$ вне зависимости от статистики, характерной для частиц. При одноимённых знаках новых плотностей, отношения B'/B и L'/L не определены. Действительно, благодаря разным статистикам при $m \lesssim m^{\text{крит}}$ весовые функции отличаются достаточно, чтобы считать конечным выражение в скобках в левой части равенства.

2.1 ТЕХНИЦВЕТОВАЯ МОДЕЛЬ

Применим полученный результат к пробной модели. В первую очередь рассмотрим техницветовую модель (WTC) [4–9]. В таком случае система уравнений имеет вид:

- плотности технибарионного и технилептонного чисел

$$\begin{aligned} TB =& \frac{2}{3}(\sigma_{UU}\mu_{UU} + \sigma_{UD}\mu_{UD} + \sigma_{DD}\mu_{DD}) = \\ =& \frac{2}{3}(\sigma_{UU} + \sigma_{UD} + \sigma_{DD})\mu_{UU} + \frac{2}{3}(\sigma_{UD} + 2\sigma_{DD})\mu_W, \end{aligned} \tag{2.14}$$

$$TL = 2(\sigma_E + \sigma_N)\mu_{NL} + 2\sigma_E\mu_W, \tag{2.15}$$

- сохранение электрического заряда

$$\begin{aligned} Q = 0 =& \left((y_{WTC} + 1)\sigma_{UU} + y_{WTC}\sigma_{UD} + (y_{WTC} - 1)\sigma_{DD}\right)\mu_{UU} - \\ & - \left((3y_{WTC} - 1)\sigma_N + (3y_{WTC} + 1)\sigma_E\right)\mu_{NL} + \\ & + 2(2\sigma_t + 1)\,\mu_{uL} - 2\mu + \\ & + \left(y_{WTC}\sigma_{UD} + 2(y - 1)\sigma_{DD} - (3y_{WTC} + 1)\sigma_E - 18\right)\mu_W, \end{aligned} \tag{2.16}$$

- сфалеронное уравнение

$$3(\mu_{uL} + 2\mu_{dL}) + \mu + \frac{1}{2}\mu_{UU} + \mu_{DD} + \mu_{NL} = 0; \tag{2.17}$$

$$9\mu_{uL} + \mu + \frac{3}{2}\mu_{UU} + \mu_{NL} + 8\mu_W = 0. \tag{2.18}$$

Общий масштаб масс техничастиц и возможность менять значение зарядового параметра y_{WTC} приводят к многокомпонентному сценарию скрытой массы. Таким образом, наиболее упрощённый вид системы:

$$\begin{cases} \frac{TB}{B} + \gamma(\sigma_i)\frac{TL}{B} = -\alpha(\sigma_i)\left(\frac{L}{B} + \beta(\sigma_i)\right) \\ m_{UU}\left|\frac{TB}{B}\right| + m_N\left|\frac{TL}{B}\right| = m_b\frac{\Omega_{DM}}{\Omega_b}, \end{cases} \tag{2.19}$$

где использовано предположение, что из двух технилептонов именно N стабилен (обратный случай ничем существенно не отличается и может быть описан в тех же терминах). Функции $\alpha(\sigma_i)$, $\beta(\sigma_i)$ и $\gamma(\sigma_i)$ определены положительно. Чередование знаков y_{WTC} оказывается не существенно: все слагаемые, где возникает этот параметр экспоненциально подавлены весом σ_{UU} по сравнению с остальными.

Далее, рассмотрим отношения TB/B и TL/B, а также TB/TL. При определённых знаках зарядов это, потенциально, позволяет отбросить часть допустимой области.

Таким образом, при решении системы уравнений (2.19) относительно L/B знаки согласованы на отрезках, где

$$\frac{\Omega_b}{\Omega_{DM}}\alpha(\sigma_i)\left(\frac{L}{B} + \beta(\sigma_i)\right) \in \begin{cases} \left[-\frac{1}{m_{UU}}; -\frac{\gamma(\sigma_i)}{m_N}\right]. & (+,+) \\ \left[-\frac{1}{m_{UU}}; \frac{\gamma(\sigma_i)}{m_N}\right], & (+,-) \\ \left[-\frac{\gamma(\sigma_i)}{m_N}; \frac{1}{m_{UU}}\right], & (-,+) \\ \left[\frac{\gamma(\sigma_i)}{m_N}; \frac{1}{m_{UU}}\right]. & (-,-) \end{cases} \tag{2.20}$$

В скобках даны знаки отношений $\left(\frac{TB}{B}; \frac{TL}{B}\right)$. Если они отличаются друг от друга, то L/B должно иметь значения, вблизи точки $L/B = -\beta(\sigma_i)$. В приближении равных масс $m_{UU} = m_{UD} = m_{DD}$, $m_N = m_E$ и $\sigma_{UU} = \sigma_N$ или, что почти то же при заданных масштабах аргумента, $m_{UU} = m_N$: $\alpha(\sigma_i) = \sigma_{UU}/3$, $\beta(\sigma_i) \equiv 3$, $\gamma(\sigma_i) \equiv 1/3$, из чего следует, что эти области

экспоненциально быстро расширяются с увеличением массы частиц за счёт падения величины $\alpha(\sigma_i)$. При $m_{UU}^{\text{крит}} \approx 3.6\,\text{ТэВ}$ ($\pm 0.1\,\text{ТэВ}$ в зависимости от рассматриваемого края отрезка) все разрешённые наблюдениями значения ($\left|\frac{L}{B}\right| \leq 6.6 \cdot 10^6$) оказываются включены в неё. В случае одинаковых знаков, решение существует при $\gamma(\sigma_i) - \frac{m_E}{m_{UU}} < 0$, что выполняется в приближении равных масс. При этом область, вместо расширения, сдвигается вдоль оси L/B от точки $L/B = -\beta(\sigma_i)$ в отрицательном направлении для $(+,+)$ и положительном для $(-,-)$. Масса $m_{UU}^{\text{крит}}$ отражает момент, когда области перестают пересекаться.

Отношение TB/TL для сочетания знаков $(\pm_1, \pm_2)$ имеет вид

$$\frac{TB}{TL} = -\frac{m_N \alpha(\sigma_i)\left(\frac{L}{B} + \beta(\sigma_i)\right) \pm_2 \gamma(\sigma_i)\frac{\Omega_{DM}}{\Omega_b}}{\pm_1 \pm_2 m_{UU}\alpha(\sigma_i)\left(\frac{L}{B} + \beta(\sigma_i)\right) \pm_2 \frac{\Omega_{DM}}{\Omega_b}} \tag{2.21}$$

и пробегает интервал $[0; \pm\infty)$ на отрезках (2.20). В рамках модели это означает, что в случае одинаковых знаков перепроизводства аномальных изотопов не происходит лишь если массы частиц близки к $m_{UU}^{\text{крит}}$. Тогда, выбором знака y_{WTC} можно подавить число частиц с положительным зарядом. В случае же различных знаков, при $m_{UU} < m_{UU}^{\text{крит}}$, отношение TB/TL, действительно, может принимать любые значения, тогда как при $m_{UU} > m_{UU}^{\text{крит}}$ оно экспоненциально быстро сходится к своему значению при $L/B = 0$, т.е. к $TB/TL = 1/3$.

Таким образом, хотя общих ограничений установить нельзя, случаи $(+,+)$ и $(-,-)$ почти полностью исключаются (за исключением ближайшей окрестности $m_{UU} = m_{UU}^{\text{крит}} \approx 3.6\,\text{ТэВ}$). Для $(+,-)$ и $(-,+)$ же удаётся оценить отношение концентраций компонент скрытой массы для случая $m_{UU} > m_{UU}^{\text{крит}}$.

2.2 МОДЕЛЬ С ТЯЖЁЛЫМ ЧЕТВЁРТЫМ ПОКОЛЕНИЕМ

В случае модели с тяжёлым четвёртым поколением [10–13] система уравнений имеет вид [14]:

- плотности барионного и лептонного чисел новых частиц

$$FB = 2(\sigma_U + \sigma_D)\mu_{UL} + 2\sigma_D\mu_W, \tag{2.22}$$

$$FL = 2(\sigma_N + \sigma_E)\mu_{NL} + 2\sigma_E\mu_W. \tag{2.23}$$

- условия сохранения зарядов

$$\begin{aligned} Q = 0 = {} & 2(2\sigma_{UL} - \sigma_{DL})\mu_{UL} + 2(2\sigma_t + 1)\mu_{uL} - \\ & -2\sigma_E\mu_{NL} - 2\mu - 2(\sigma_D + \sigma_E - 10)\mu_W, \end{aligned} \tag{2.24}$$

$$Y = 0 = 2(\sigma_N + \sigma_E)\mu_{NL} - 2(\sigma_U + \sigma_D)\mu_{UL} + 2(\sigma_E - \sigma_D)\mu_W \tag{2.25}$$

Связь химических потенциалов, следующая из свойств сфалеронного перехода:

$$9\mu_{uL} + \mu + 3\mu_{UL} + \mu_{NL} + 8\mu_W = 0. \tag{2.26}$$

Решение может быть представлено в виде связи отношений плотностей чисел:

$$\frac{FB}{B} = -\alpha(\sigma_i)\ \left(\frac{L}{B} + \beta(\sigma_i)\right), \tag{2.27}$$

где функции α и β зависят при фиксированной T_* только от масс частиц:

$$\alpha \approx \frac{\sigma_U(3\,\sigma_U^2 + 26\,\sigma_U + 19)}{16\,\sigma_U^2 + 116\,\sigma_U + 60}, \quad \beta \approx \frac{9\,\sigma_U^2 + 74\,\sigma_U + 61}{3\,\sigma_U^2 + 26\,\sigma_U + 19}. \tag{2.28}$$

Здесь было использовано приближение равных масс $\sigma_E = \sigma_D = \sigma_U$ и упрощение $\sigma_N = 1, \sigma_t = 1$ для наглядности.

Если $f \cdot 100\%$ плотности скрытой массы обеспечена кластерами $\bar{U}\bar{U}\bar{U}$, то

$$\frac{\Omega_{DM}}{\Omega_b} \approx f\frac{3m_U}{m_b}\ \left|\frac{FB}{B}\right|. \tag{2.29}$$

На рисунке 2.1 представлено графическое решение уравнения (2.29) для разных значений L/B. Минимальное значение данного параметра, подобрано так, что примерно соответствует $3m_U \sim 1060\,\text{ГэВ}$: $L/B \approx -3$. Крайняя правая линия, соответствующая максимальному значению лептонной асимметрии, даёт оценку максимальной массы тёмного атома: $m_{\text{ANO-He}} \sim 10.5\,\text{ТэВ}$. Графики на правой панели построены в логарифмическом мас-

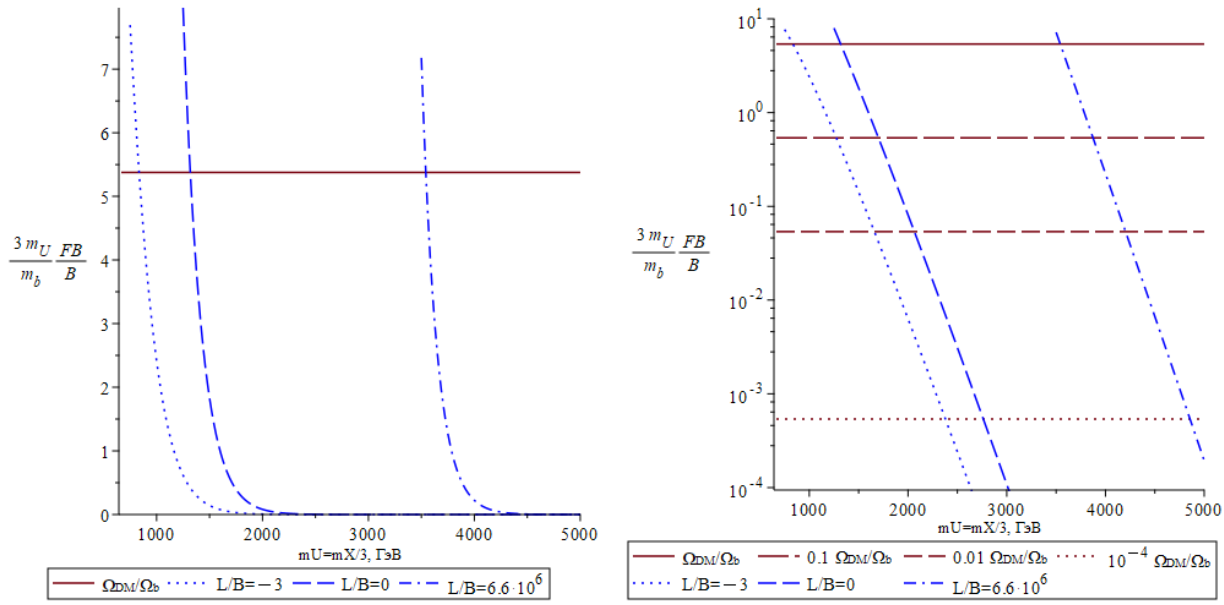

Рисунок 2.1 — Графическое решение уравнения (2.29), задающие пределы масс ANO-гелия.

штабе и отображают ограничения для случая, если ANO-гелий обеспечивает лишь долю от полной плотности скрытой массы. Значение $m_{\text{ANO-He}}$ смещается в большую сторону примерно на 1 ТэВ за порядок.

3 СЕЧЕНИЯ ЗАХВАТА ЛЁГКИХ ЯДЕР

Описание последовательного захвата лёгких ядер многозарядными частицами требует рассмотрения нескольких типов реакций:

$$X + N_1 \to XN_1 + \gamma, \tag{3.1}$$
$$XN_1 + N_2 \to XN_3 + \gamma/N_4, \tag{3.2}$$
$$XN_1 + XN_2 \to XN_3X + \gamma/N_4, \tag{3.3}$$

где N_i — некоторое лёгкое ядро.

3.1 ПЕРВЫЙ ЭТАП

3.1.1 ВИД СЕЧЕНИЙ ПЕРВОГО ЭТАПА

Сечения фоторазрушения σ_γ и радиационной рекомбинации на основное состояние σ_{rr} для частиц в произвольном потенциале:

$$\sigma_\gamma = \frac{4\pi}{3}\frac{Z_N}{Z_X}\frac{r_B}{m_N}\frac{\eta^3}{1+\eta^2}\left|\int \rho^2 R_{\varkappa 1}(\rho)\partial_\rho R_{10}(\rho)d\rho\right|^2, \tag{3.4}$$

$$\begin{aligned}\sigma_{rr} &= \frac{2\pi}{3}\frac{Z_N}{Z_X}\frac{1}{m_N^3 r_B}\eta(1+\eta^2)\left|\int \rho^2 R_{\varkappa 1}(\rho)\partial_\rho R_{10}(\rho)d\rho\right|^2 = \\ &= \frac{4\pi}{3}\frac{Z_N}{Z_X}\frac{E_\gamma}{m_N^2 r_B^2 k^3}\left|\int \rho^2 R_{\varkappa 1}(\rho)\partial_\rho R_{10}(\rho)d\rho\right|^2,\end{aligned} \tag{3.5}$$

где, как и ранее, $\eta = Z_1 Z_2 \alpha\sqrt{\frac{\mu_{12}}{2E}} = \frac{1}{kr_B}$ — параметр Зоммерфельда, для которого положено $\mu_{12} = \frac{m_N m_X}{m_N + m_X} \approx m_N$, радиальные части волновых функций $R_{\varkappa 1}(\rho)$ и $R_{10}(\rho)$ определены в терминах безразмерных параметров $\rho = r/r_B$, $\varkappa = kr_B$ и нормированы как

- $\int |R_{n_0 l}(r)|^2 r^2 dr = \int |R_{n_0 l}(\rho)|^2 r_B^3 \rho^2 d\rho = 1 \Rightarrow R_{n_0 l}(r) = \frac{1}{r_B^{3/2}} R_{n_0 l}(\rho)$ —

для дискретного спектра;

- $\int |R_{kl}(r)|^2 r^2 dr = \int |R_{\varkappa l}(\rho)|^2 r_B^3 \rho^2 d\rho = 2\pi\delta(k'-k) = 2\pi r_B \delta(\varkappa'-\varkappa) \Rightarrow R_{n_0 l}(r) = \frac{1}{r_B} R_{n_0 l}(\rho)$ — для непрерывного спектра.

Таким образом, скорость радиационного захвата лёгкого ядра на основное состояние может быть определена как двойной интеграл:

$$\langle \sigma_{rr} v \rangle = \frac{2\sqrt{2\pi}}{3} \frac{Z_N}{Z_X} \frac{1}{m_N^4 r_B^5} \frac{1}{(m_N T)^{3/2}} \cdot \cdot \int \frac{1+\eta^2}{\eta^4} \exp\left(-\frac{1}{2 m_N r_B^2 T} \frac{1}{\eta^2}\right) \left| \int \rho^2 R_{\varkappa 1}(\rho) \partial_\rho R_{10}(\rho) d\rho \right|^2 d\eta. \tag{3.6}$$

3.1.2 УРАВНЕНИЕ ШРЁДИНГЕРА

Относительная внутренняя простота изотопов водорода (p, d, t) и гелия (^{3}He, ^{4}He) позволяет рассматривать их как однородно заряженные сферы, что приводит к сферически-симметричному потенциалу вида

$$V(\rho) = 2 m_N r_B^2 U(\rho) = \begin{cases} -\frac{1}{a}\left(3 - \frac{\rho^2}{a^2}\right), & \rho < a; \\ -\frac{2}{\rho}, & \rho > a. \end{cases} \tag{3.7}$$

Уравнение Шрёдингера в естественных единицах ($\hbar = 1$)

$$\left(\frac{1}{2m_N}\nabla^2 - U(r)\right)\Psi = -E\Psi \tag{3.8}$$

может быть преобразовано к более удобной для использования форме:

$$\partial_\rho^2 P(\rho) + \left(V(\rho) - \frac{l(l+1)}{\rho^2}\right) P(\rho) + \varepsilon P(\rho) = 0, \tag{3.9}$$

где выделена радиальная часть волновой функции $\Psi(r) = R(r)\, Y(\theta, \phi) = \frac{P(r)}{r} Y(\theta, \phi)$, введено обозначение $\varepsilon = 2 m_N r_B^2 E$, радиальная переменная ρ и импульс $\varkappa$ безразмерны.

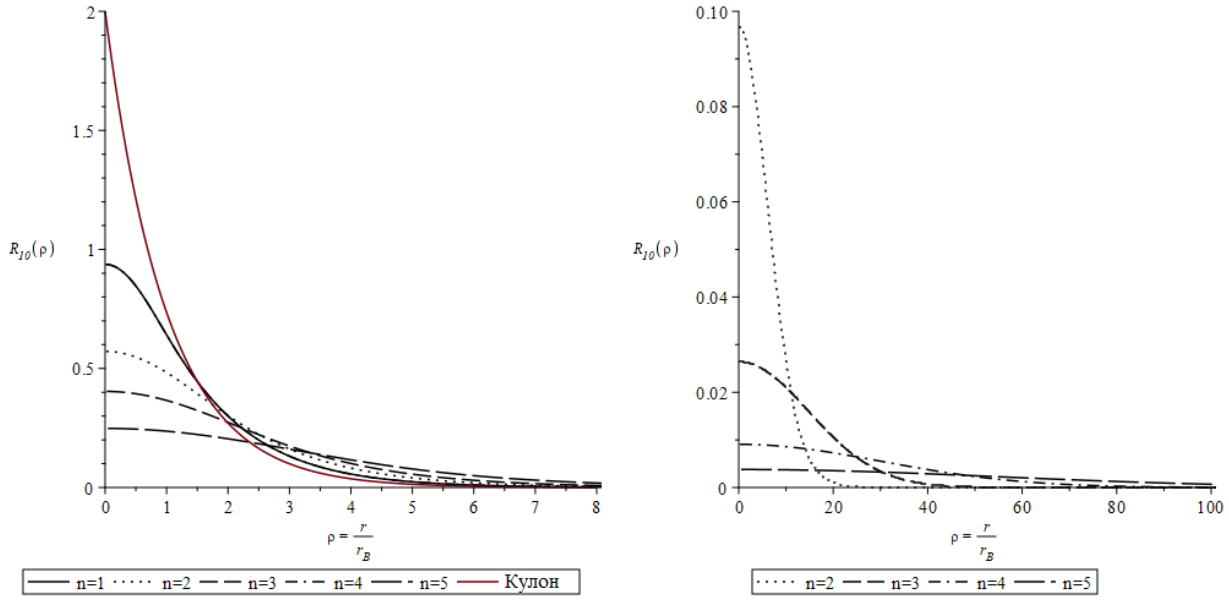

Рисунок 3.1 — Собственные функции уравнения (3.9) для тёмных ионов X–^{4}He (слева) и тёмных атомов $(XN)^0$ (справа).

3.1.2.1 Дискретный спектр

Примеры волновых функций дискретного спектра, полученных численным решением этого уравнения при разных зарядах ядра с граничными условиями

$$P(0) = 0, \qquad P(\rho_{\max}) = 0, \tag{3.10}$$

где $\rho_{\max}$ подбирается для достижения требуемой точности в каждом отдельном случаи, представлены на Рисунке 3.1. На левой панели изображены волновые функции связанных состояний вида X–^{4}He.

В таблицах 3.1—3.5 приведены характерные размеры для различных систем XN, а также их энергии связи, полученные при решении уравнения (3.9) $E_{XN}^{\text{ОЗС}}$. Для сравнения в таблице также указаны энергии связи для кулоновского и чисто осцилляторного потенциалов.

p						
$2n$		2	4	6	8	10
Радиусы	R, Фм	0.841 [15]				
	r_B, МэВ$^{-1}$	0.073	0.037	0.024	0.018	0.015
	a	0.058	0.115	0.173	0.230	0.288
E_{XN}	$E_{XN}^{\text{Кулон}}$, МэВ	0.100	0.400	0.900	1.599	2.500
	$E_{XN}^{\text{ОЗС}}$, МэВ	0.100	0.396	0.883	1.550	2.388

Таблица 3.1 — Характерные радиусы и энергии связи для Xp.

d						
$2n$		2	4	6	8	10
Радиусы	R, Фм	2.127 [15]				
	r_B, МэВ$^{-1}$	0.037	0.018	0.012	0.009	0.007
	a	0.291	0.583	0.873	1.165	1.456
E_{XN}, МэВ	$E_{XN}^{\text{Кулон}}$	0.200	0.799	1.798	3.196	4.994
	$E_{XN}^{\text{Осциллятор}}$	—	—	—	0.604	1.762
	$E_{XN}^{\text{ОЗС}}$	0.191	0.701	1.439	2.343	3.371

Таблица 3.2 — Характерные радиусы и энергии связи для Xd.

t						
$2n$		2	4	6	8	10
Радиусы	R, Фм	1.7591 [16]				
	r_B, МэВ$^{-1}$	0.0244	0.0122	0.008	0.006	0.005
	a	0.361	0.721	1.082	1.443	1.803
E_{XN}, МэВ	$E_{XN}^{\text{Кулон}}$	0.299	1.197	2.692	4.787	7.479
	$E_{XN}^{\text{Осциллятор}}$	—	—	0.288	1.666	3.176
	$E_{XN}^{\text{ОЗС}}$	0.280	1.005	2.023	3.243	4.609

Таблица 3.3 — Характерные радиусы и энергии связи для Xt.

^{3}He						
$2n$		2	4	6	8	10
Радиусы	R, Фм	1.970 [17]				
	$r_B, 10^{-3}\,\text{МэВ}^{-1}$	12.20	6.10	4.07	3.05	2.44
	a	0.808	1.615	2.423	3.230	4.037
E_{XN}, МэВ	$E_{XN}^{\text{Кулон}}$	1.196	4.786	10.768	19.142	29.910
	$E_{XN}^{\text{Осциллятор}}$	—	1.894	4.767	7.888	11.164
	$E_{XN}^{\text{ОЗС}}$	0.978	3.095	5.742	8.692	11.841

Таблица 3.4 — Характерные радиусы и энергии связи для X^3He.

^{4}He						
$2n$		2	4	6	8	10
Радиусы	R, Фм	1.678 [15; 18]				
	$r_B, 10^{-3}\,\text{МэВ}^{-1}$	9.19	4.60	3.06	2.30	1.84
	a	0.913	1.826	2.739	3.652	4.566
E_{XN}, МэВ	$E_{XN}^{\text{Кулон}}$	1.588	6.352	14.291	25.406	39.698
	$E_{XN}^{\text{Осциллятор}}$	—	2.713	6.195	9.950	13.878
	$E_{XN}^{\text{ОЗС}}$	1.256	3.892	7.130	10.712	14.510

Таблица 3.5 — Характерные радиусы и энергии связи для X^4He.

В таблице 3.6 приведены энергии связи, найденные для изотопа ^{56}Fe, рассчитанные для осцилляторного потенциала и потенциала, полученного из распределения Ферми (2pF) для заряда:

$$V(\rho) = \frac{2}{a^3 r_B^2}\left(\frac{1}{r_B\rho}\int\limits_0^{r_B\rho}\frac{r^2}{1+\exp((r-r_N)/b)}dr + \int\limits_{r_B\rho}^{\infty}\frac{r}{1+\exp((r-r_N)/b)}dr\right), \tag{3.11}$$

где b — параметр диффузности. Для расчёта использованы значения параметров $r_N = 4.111$ фм и $b = 0.558$ [19] (верхний ряд). Расчёт для второго набора параметров, представленных в [19] ($r_N = 4.106$ фм и $b = 0.519$) приводит к отличию энергий до нескольких десятков МэВ (см. нижний

ряд Таблицы 3.6).

^{56}Fe					
$2n$	2	4	6	8	10
$E_{XN}^{\text{Осциллятор}}$, МэВ	23.638	47.958	72.391	96.881	121.409
E_{XN}^{2pF}, МэВ	59.116	122.934	187.681	252.918	318.471
	63.251	131.708	201.197	271.232	341.617

Таблица 3.6 — Энергии связи для X–^{56}Fe.

В случае лёгких ядер, введу меньших масштабов системы, отличия менее существенны: неопределённость достигает лишь сотен кэВ.

На рисунке 3.2 показаны отличия модулей радиальных частей волновых функций возбуждённых состояний ($l = 0$, слева: $n_0 = 2$, справа: $n_0 = 3$) системы X–^{4}He при $n = 1$ (верхний ряд) и $n = 5$ (нижний ряд).

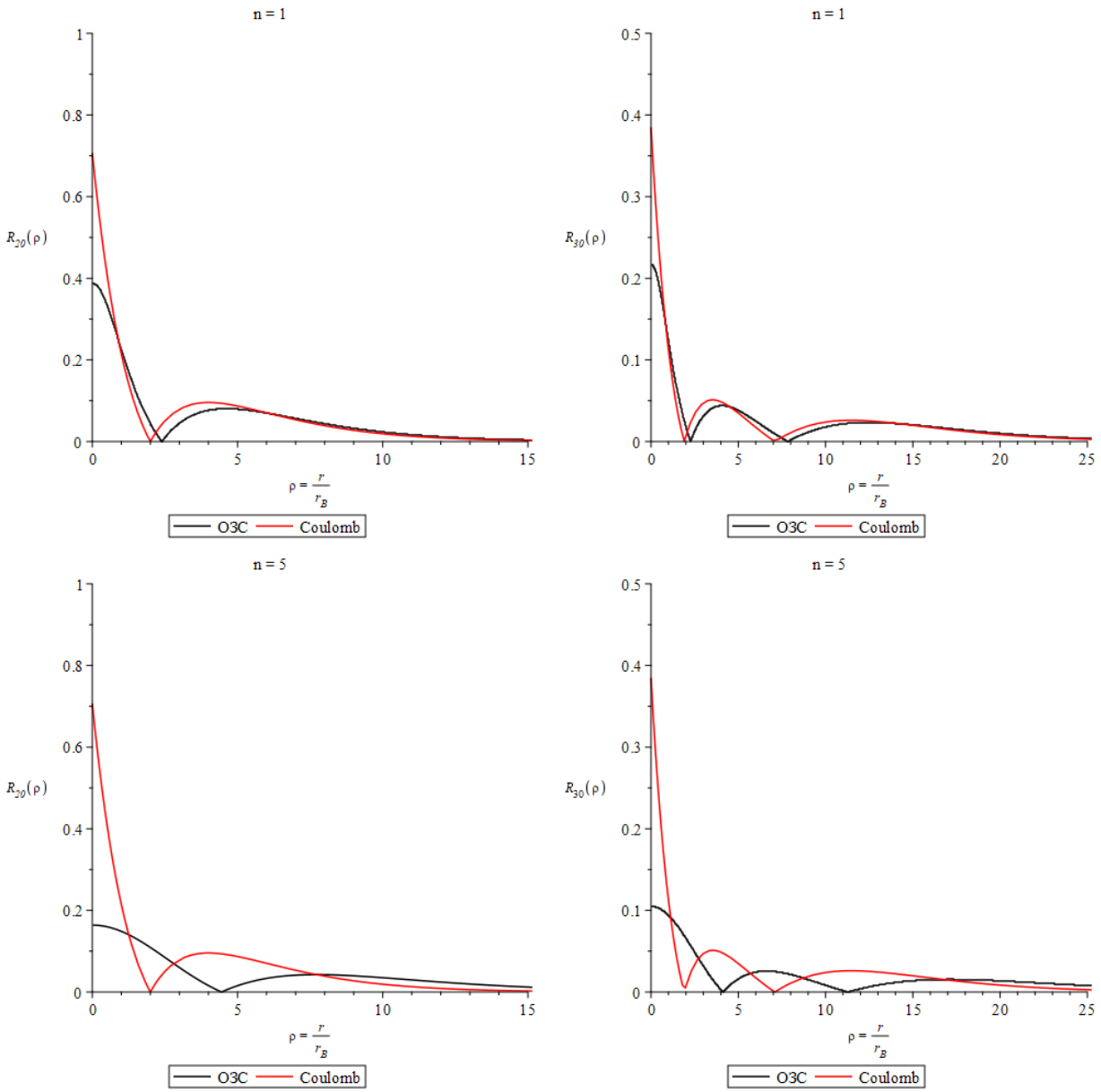

Рисунок 3.2 — Волновые функции возбуждённых состояний ($l = 0$, слева: $n_0 = 2$, справа: $n_0 = 3$) системы X–^{4}He при $n = 1$ (верхний ряд) и $n = 5$ (нижний ряд)

Соответствующие энергии связи $E_{XN}^{(n_0,n)}$:

$n = 1$: $E_{XN}^{(2,1)} = 0.357\,\text{МэВ}$, $E_{XN}^{(3,1)} = 0.164\,\text{МэВ}$;
$n = 5$: $E_{XN}^{(2,5)} = 6.063\,\text{МэВ}$, $E_{XN}^{(3,5)} = 3.156\,\text{МэВ}$.

3.1.2.2 Непрерывный спектр

Для непрерывного спектра уравнение (3.9) необходимо решить для набора заранее заданных энергий, достаточного для последующего численного

интегрирования. Предполагая максвелловское распределение по энергиям, таковым интервалом можно считать $[0.01T; 10T]$, где для нуклеосинтеза $T = 5 - 100\,\text{кэВ}$. Использованы начальные условия

$$P(\rho_{\min}) = \rho_{\min}^{l+1}, \qquad \partial_\rho P(\rho_{\min}) = (l+1)\rho_{\min}^{l}, \tag{3.12}$$

при $l = 1$, $\rho_{\min} = 10^{-3}\,a$. Полученные волновые функции нормировались условием, подразумевающим кулоновское асимптотическое поведение:

$$P\left(\rho \gg \frac{2}{\varkappa^2}\right) \to 2\sin\left(\varkappa\rho + \frac{1}{\varkappa}\ln(2\varkappa\rho) - \frac{\pi}{2}l + \delta_l\right), \tag{3.13}$$

где фаза δ_l определяется фитированием решения на больших значениях ρ.

На Рисунке 3.3 представлено сравнение кулоновских и ОЗС радиальных волновых функций непрерывного спектра системы X^4He для зарядов $n = 1$ (сверху) и $n = 5$ (снизу) при минимальной $E = 5 \cdot 10^{-5}\,\text{МэВ}$ (слева) и максимальной $E = 1\,\text{МэВ}$ (справа) рассматриваемых энергиях.

На рисунке 3.4 приведены наиболее отличные от кулоновских волновые функции непрерывного спектра системе X^{-2n}–t. Хотя разница всё ещё заметна, она значительно уступает в своей выраженности той, что наблюдается для ядер гелия.

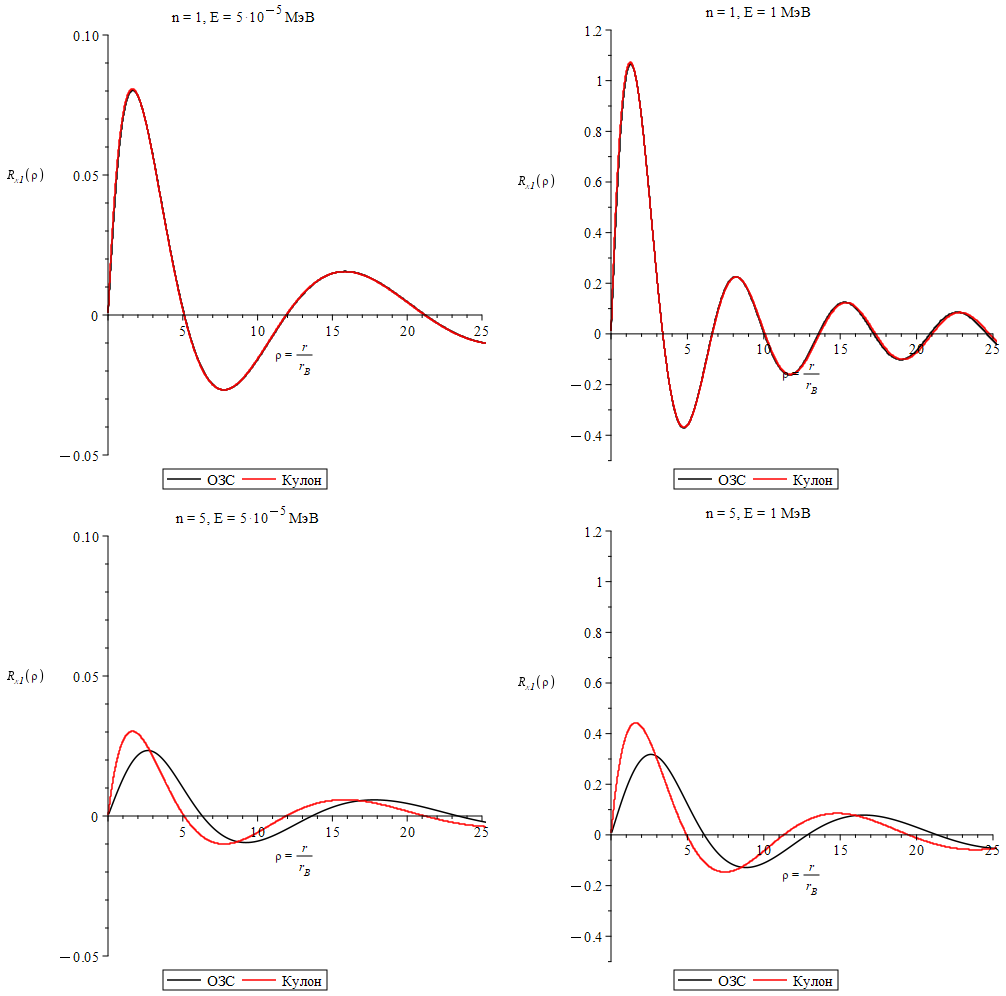

Рисунок 3.3 — Волновые функции непрерывного спектра системы X^{-2n}–^{4}He для $n = 1$ (сверху) и $n = 5$ (снизу) при $E = 10^{-5}$ МэВ (слева) и $E = 1$ МэВ (справа)

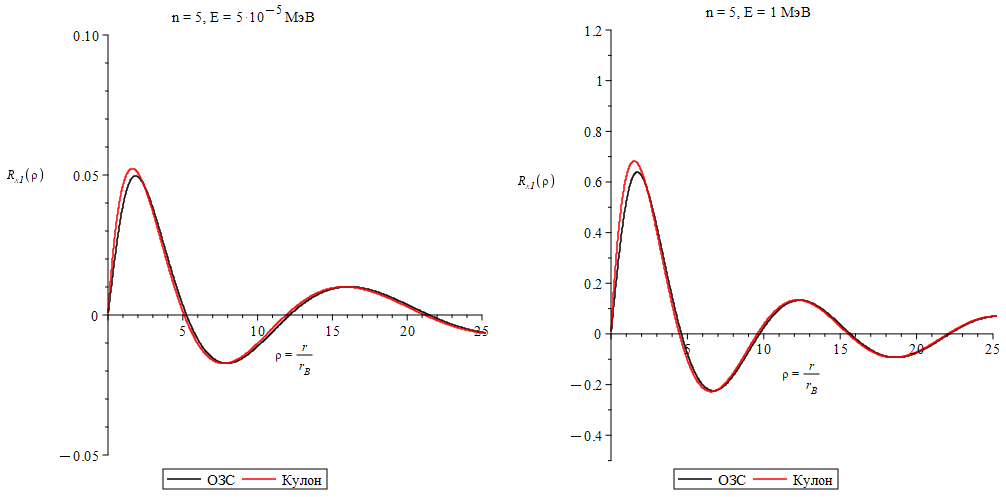

Рисунок 3.4 — Волновые функции непрерывного спектра системы X^{-2n}–t для $n = 5$ при $E = 10^{-5}$ МэВ (слева) и $E = 1$ МэВ (справа)

3.1.3 РЕЗУЛЬТАТЫ ВЫЧИСЛЕНИЙ СКОРОСТЕЙ

3.1.3.1 Основное состояние

На рисунке 3.5 представлены графики скоростей рассматриваемых процессов как функции от температуры для разных значений зарядового параметра. На рисунке 3.6 показаны те же сечения, но при фиксированных значениях заряда тяжёлой частицы. На последних двух графиках также можно увидеть разницу в масштабах между скоростями, рассчитанными для кулоновского и ОЗС потенциала. Действительно, из-за малых размеров протона эти функции достаточно близки друг к другу. На рисунке 3.7 наблюдаемое отклонение охарактеризовано количественно. Изображены графики функции $R(T) = \dfrac{\langle\sigma v\rangle^{\text{Кулон}}_{\text{аналит.}} - \langle\sigma v\rangle^{\text{ОЗС}}_{\text{числ.}}}{\langle\sigma v\rangle^{\text{Кулон}}_{\text{аналит.}}} \cdot 100\%$.

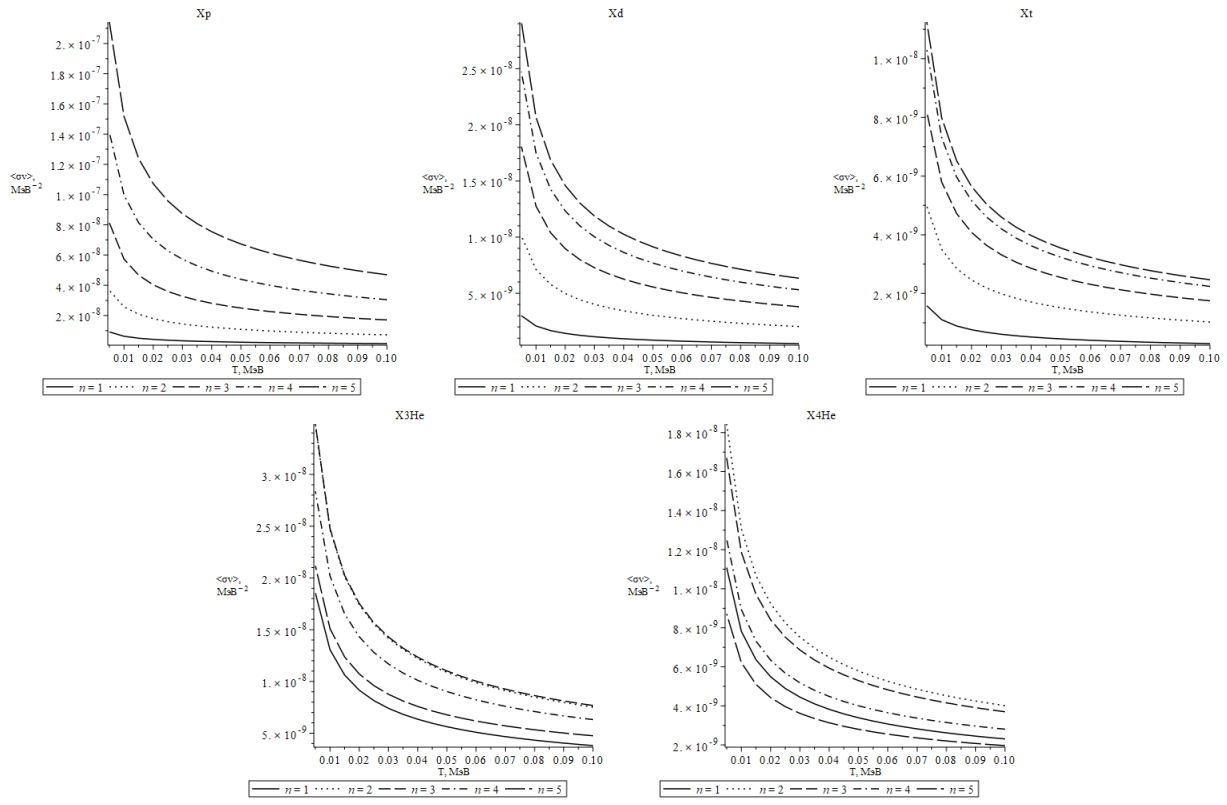

Рисунок 3.5 — Скоростей образования XN при разных значениях зарядового параметра n

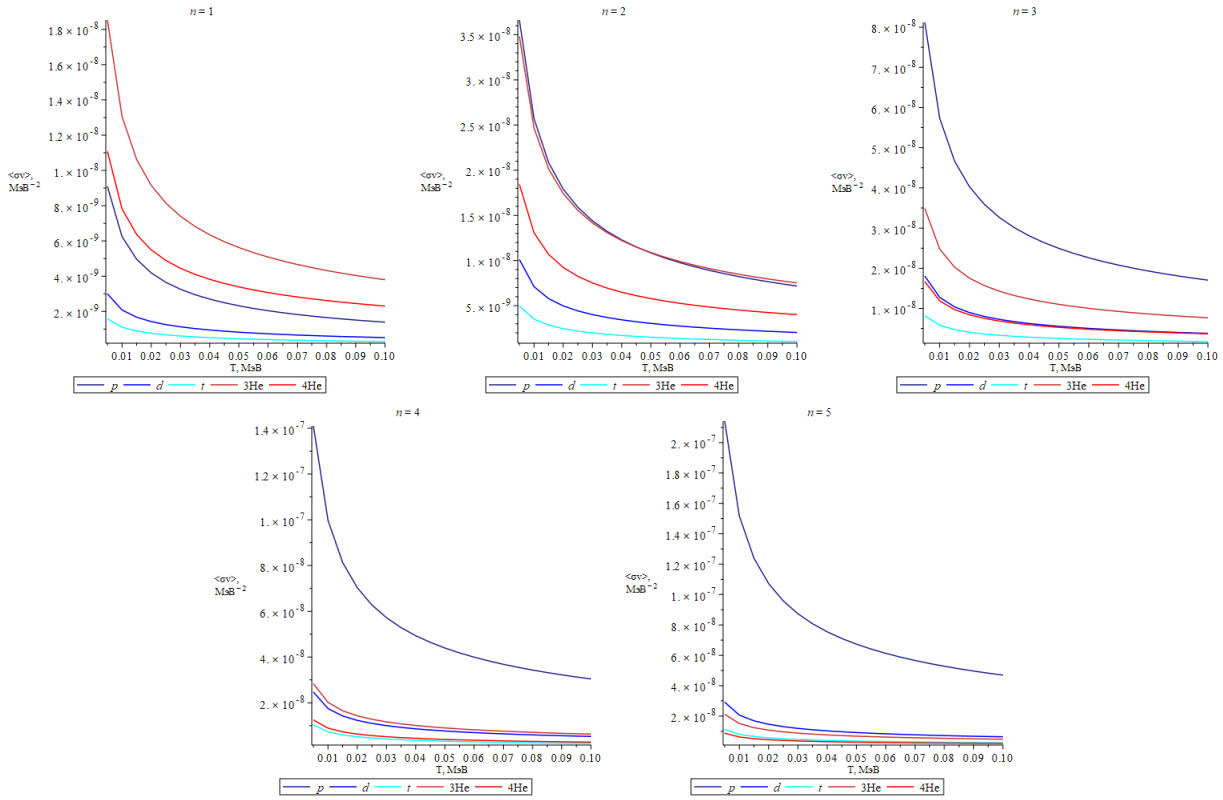

Рисунок 3.6 — Скоростей образования XN при фиксированных значениях зарядового параметра n

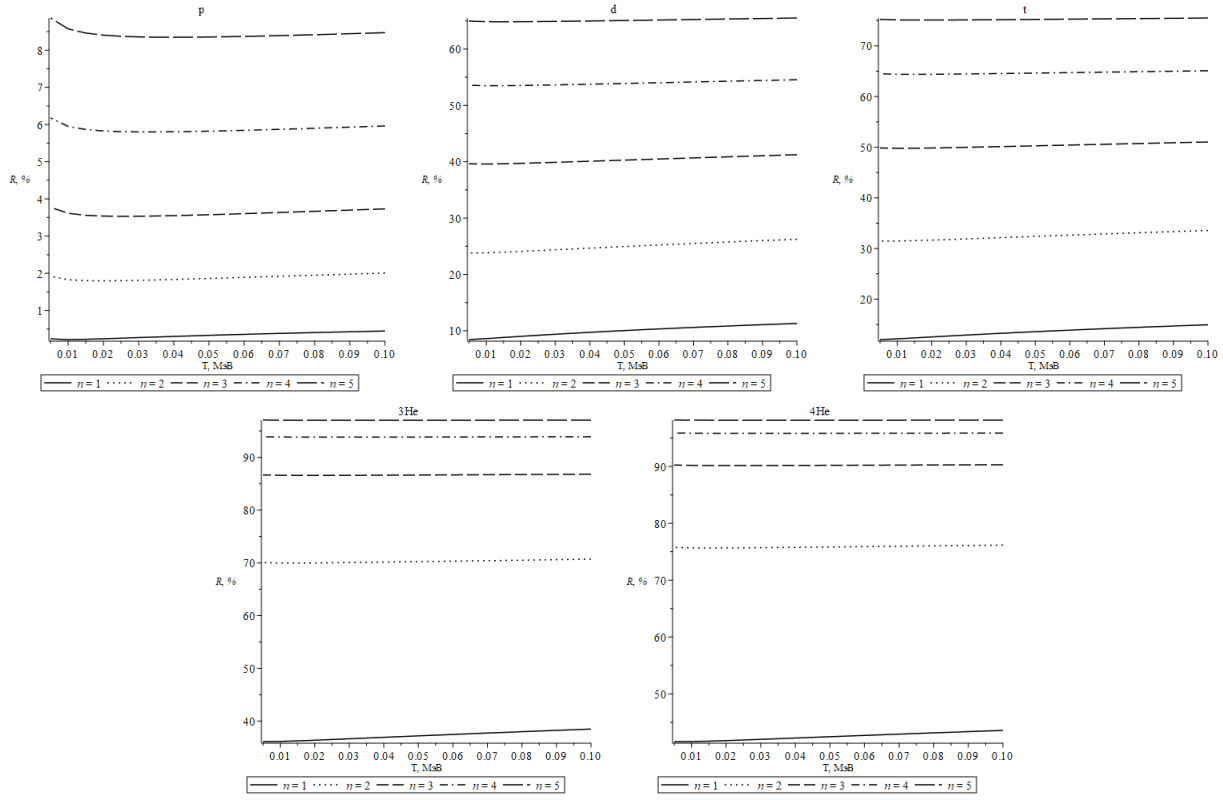

Рисунок 3.7 — Отклонение от приближения точечных частиц

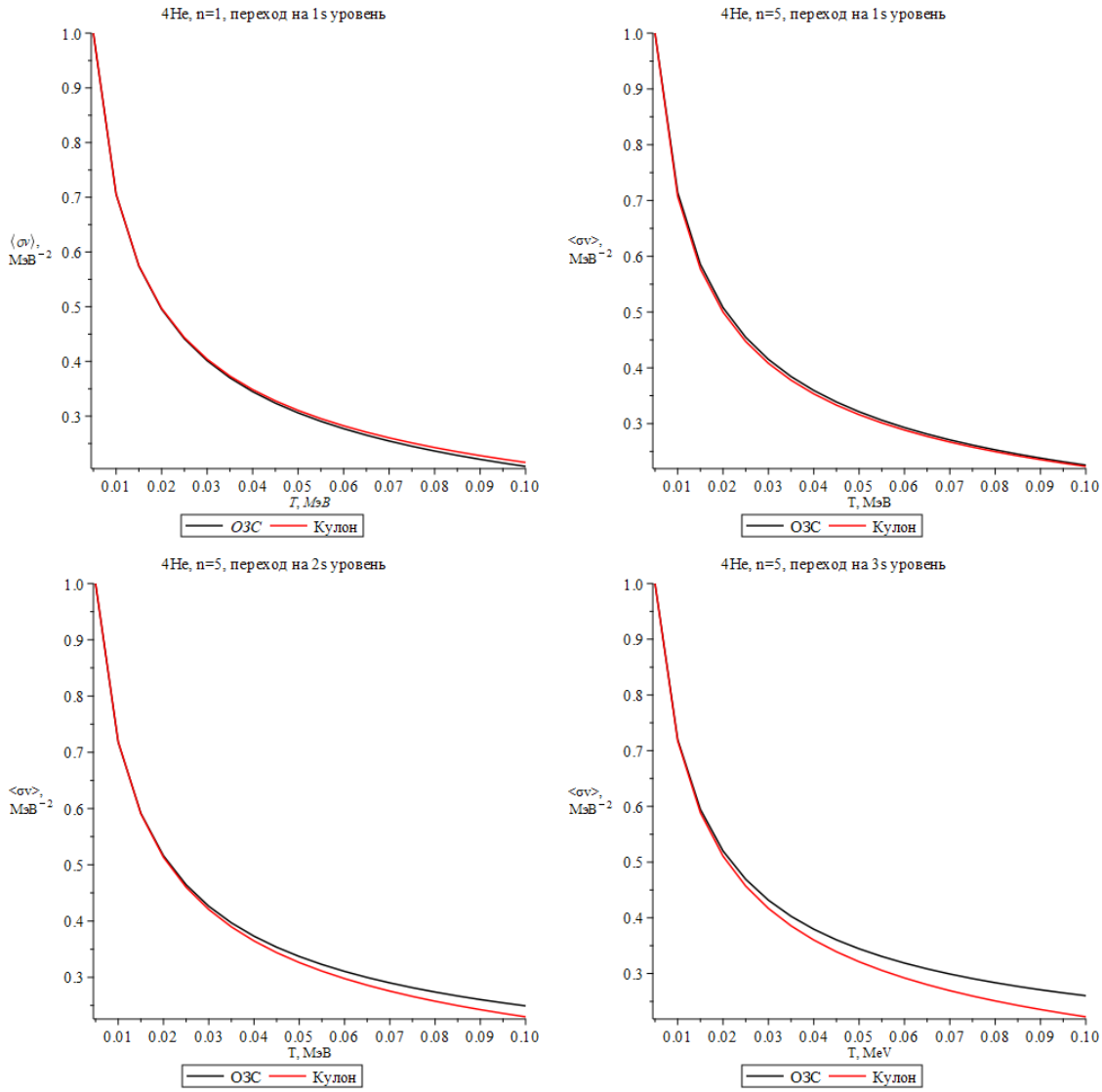

Рисунок 3.8 — Сравнение сечений захвата на основное состояние как функций температуры

3.1.3.2 Учёт возбуждённых состояний

Строгий учёт возбуждённых состояний системы XN требует суммирования всех соответствующих сечений захвата. На рисунке 3.8 сравниваются $\langle \sigma v \rangle^{\text{Кулон}}_{\text{аналит.}}$ и $\langle \sigma v \rangle^{\text{ОЗС}}_{\text{числ.}}$ для X–^{4}He. Их, значения при $T = 5\,$кэВ приняты за единицу. В нижнем ряду 3.8 показаны аналогичные сечения для переходов на возбуждённые уровни $2s$ (слева) и $3s$ (справа).

Следует также обратить внимание изменение абсолютной величины. Отношение $\frac{\langle \sigma v \rangle^{\text{ОЗС}}}{\langle \sigma v \rangle^{\text{Кулон}}}(T = 5\,\text{кэВ})$ при $n = 5$ для переходов на уровни ($1s$, $2s$, $3s$) принимает значения, соответственно, $\approx (0.0183, 0.2393, 0.2789)$.

3.2 ПРОЦЕССЫ, ИМЕЮЩИЕ АНАЛОГИ

В данном разделе рассмотрен вопрос о получении скорости реакций типа (3.2) или (3.3) на основе экспериментальных данных для их стандартного аналога

$$N_1 + N_2 \to N_3 + \gamma/N_4. \tag{3.14}$$

Основная идея заключается в том, что сечения процессов с участием скалярного X^{-2n} отличаются лишь массами и зарядами участвующих частиц. В таком случае, неизвестное сечение может быть оценено из явного вида отношения $\sigma_X(E)/\sigma_o(E)$.

Данное приближение применимо в случае, если спин тяжёлой частицы равен $s_X = 0$. Тогда, очевидно, спин-зависимые слагаемые потенциалов остаются неизменными. Более того, предлагаемая оценка должна работать лучше в реакциях с тяжёлыми ядрами, для которых характерно ядерное насыщение, приводящая к меньшей выраженности кулоновских деформаций. Это подтверждается оценками с использованием метода Хартри-Фока для бозонов.

Данная задача, хотя и подразумевает относительно низкие энергии, может быть решена только в рамках релятивистской квантовой механики. Сечение реакции $(2 \to 2)$ в СЦИ в общем виде может быть найдено как ([20], §64)

$$\begin{aligned}\sigma_{2\to2} &= \int (2\pi)^4\, \delta^{(4)}(P_i - P_f)\, |M_{fi}|^2\, \frac{1}{4p_i(\varepsilon_1+\varepsilon_2)} \prod_f \frac{d^3p_f}{(2\pi)^3 2\varepsilon_f} = \\ &= \int \delta(\varepsilon_i - \varepsilon_f)\, \left|M^\theta_{fi}\right|^2 \frac{1}{16\pi}\, \frac{1}{p_i(\varepsilon_1+\varepsilon_2)\varepsilon_3\varepsilon_4}\, p_f^2 dp_f,\end{aligned} \tag{3.15}$$

где P_i, P_f — 4-импульсы начального и конечного состояний, p_i, p_f — модули соответствующих 3-импульсов, ε_j — релятивистские энергии. Во второй строке принято обозначение $\left|M^\theta_{fi}\right|^2 = \int |M_{fi}|^2\, d\phi_f d(\cos\theta_f)$.

Возможны два случая: возникновение массивной частицы N_4, далее обозначаемый как $4N$ и радиационный захват, обозначаемый $3N\gamma$.

$(4N)$: Переходя к интегрированию по энергии и, затем к нерелятивистско-

му пределу:

$$\varepsilon_f^2 \approx \mu_f^2 + p_f^2 \Rightarrow p_f dp_f = \varepsilon_f d\varepsilon_f \approx (\mu_f + E_f) dE_f,$$

где E_f — кинетическая энергия конечного состояния. Тогда, имея введу, что $\delta(\varepsilon_i - \varepsilon_f) = \delta(E_i + Q - E_f)$, Q — выделяемая в реакции энергия,

$$\begin{aligned}\sigma_{4N} &= \frac{1}{16\pi} \left|M_{fi}^{\theta}\right|^2 \frac{\varepsilon_f p_f}{p_i(\varepsilon_1 + \varepsilon_2)\varepsilon_3\varepsilon_4} \approx \\ &\approx \frac{1}{16\pi} \left|M_{fi}^{\theta}\right|^2 \sqrt{\frac{\mu_f}{\mu_i}} \sqrt{\frac{E_i + Q}{E_i}} \frac{\mu_f + E_i + Q}{(m_1 + m_2 + E_i)} \\ &\qquad \cdot \frac{1}{(m_3 + \frac{\mu_f}{m_3}(E_i + Q))(m_4 + \frac{\mu_f}{m_4}(E_i + Q))} \approx \\ &\approx \frac{1}{16\pi} \left|M_{fi}^{\theta}\right|^2 \frac{\mu_f \sqrt{\mu_f \mu_i}}{m_1 m_2 m_3 m_4} \sqrt{\frac{E_i + Q}{E_i}}.\end{aligned} \tag{3.16}$$

Последнее равенство получено «в нулевом приближении»: везде, где это возможно, пренебрегается кинетической энергией и энерговыделением по сравнению с массами частиц.

$(3N\gamma)$: Введу отсутствия у фотона массы, аккуратное интегрирование требует работы с аргументом δ-функции:

$$\begin{aligned}\delta(\varepsilon_i - \varepsilon_f) &= \delta\left(Q + E_i - \frac{p_f^2}{2m_3} - p_f\right) = \\ &= \frac{1}{\sqrt{1 + 2\frac{E_i + Q}{m_3}}} \delta\left(p_3 - m_3\left(-1 + \sqrt{1 + 2\frac{E_i + Q}{m_3}}\right)\right).\end{aligned}$$

При переходе к нерелятивистскому пределу корни следует разлагать как минимум до слагаемых второго порядка. В таком случае $p_f \approx$

$E_i + Q$ и

$$\begin{aligned}\sigma_{3N\gamma} &= \frac{1}{16\pi}\left|M_{fi}^{\theta}\right|^2 \frac{1}{\sqrt{1+2\frac{E_i+Q}{m_3}}}\frac{p_f}{p_i(\varepsilon_1+\varepsilon_2)\varepsilon_3} \approx \\ &\approx \frac{1}{16\pi}\left|M_{fi}^{\theta}\right|^2 \frac{1}{\sqrt{1+2\frac{E_i+Q}{m_3}}}\frac{\sqrt{1+2\frac{E_i+Q}{m_3}}-1}{\sqrt{2m_iE_i}(m_1+m_2+E_i)} \\ &\qquad\qquad \cdot \frac{1}{\left(2+\frac{(E_i+Q)}{m_3}-\sqrt{1+2\frac{E_i+Q}{m_3}}\right)} \approx \\ &\approx \frac{\sqrt{2}}{32\pi}\left|M_{fi}^{\theta}\right|^2 \frac{\sqrt{\mu_i}}{m_1m_2m_3}\frac{E_i+Q}{\sqrt{E_i}}\end{aligned} \tag{3.17}$$

Вероятность процесса, а значит и M_{fi}^{θ}, должна факторизовываться на часть, описывающую ядерную реакцию $M_{fi}^{\theta,\text{nuclear}}$ и часть, связанную с кулоновским взаимодействием и (3.19) вероятностью оказаться в зоне реакции:

$$\left|M_{fi}^{\theta}\right|^2 = \left|M_{fi}^{\theta,\text{nuclear}}\right|^2 \cdot |\psi(0)|^2, \tag{3.18}$$

где

$$|\psi(0)|^2 = \begin{cases} \frac{2\pi\eta}{\exp(2\pi\eta)-1}, & \text{для поля отталкивания;} \\ \frac{2\pi\eta}{1-\exp(-2\pi\eta)}, & \text{для поля притяжения;} \\ 1, & \text{при отсутствии кулоновского взаимодействия.} \end{cases} \tag{3.19}$$

Таким образом, отношение для реакции с многозарядной частицей X^{-2n} и без неё имеет вид

$$\frac{\sigma_X}{\sigma} = \begin{cases} \frac{\mu_f^X}{\mu_f}\sqrt{\frac{\mu_i^X\mu_f^X}{\mu_i\mu_f}}\frac{m_1m_3}{m_1^Xm_3^X}\sqrt{\frac{E_i+Q_X}{E+Q}}\frac{\eta_X}{\eta}\frac{|1-\exp(\pm 2\pi\eta)|}{|1-\exp(\pm 2\pi\eta_X)|_X}, & 4N \\ \sqrt{\frac{\mu_i^X}{\mu_i}}\frac{m_1m_3}{m_1^Xm_3^X}\frac{E_i+Q_X}{E_i+Q}\frac{\eta_X}{\eta}\frac{|1-\exp(\pm 2\pi\eta)|}{|1-\exp(\pm 2\pi\eta_X)|_X}, & 3N\gamma \end{cases} \tag{3.20}$$

Используя его, скорость реакции может быть найдена как

$$\langle\sigma v\rangle_X = \sqrt{\frac{8}{\pi T^3}}\int \frac{\sigma_X}{\sigma}\sigma(E)\exp\left(-\frac{E}{T}\right)EdE. \tag{3.21}$$

Сечение стандартного аналога $\sigma(E)$ может быть найдено из экспериментальных данных аппроксимацией аналогичным интегралом с подстановкой $\sigma(E) = \frac{S(E)}{E}\exp(2\pi\eta)$, и $S(E) = a_0 + a_1 E + a_2 E^2$, со свободными параметрами a_i.

СПИСОК ЛИТЕРАТУРЫ

1. Planck 2018 results. VI. Cosmological parameters / and N. Aghanim [et al.] // Astron. Astrophys. — 2020. — Vol. 641. — A6.
2. *Akhmedov E.*, *Pospelov M.* BBN catalysis by doubly charged particles // JCAP. — 2024. — Vol. 08. — P. 028. — arXiv: 2405.06019 [hep-ph].
3. Precision big bang nucleosynthesis with improved Helium-4 predictions / C. Pitrou [et al.] // Physics Reports. — 2018. — Vol. 754. — P. 1–66. — ISSN 0370-1573.
4. *Gudnason S. B.*, *Kouvaris C.*, *Sannino F.* Towards working technicolor: Effective theories and dark matter // Physical Review D. — 2006. — Vol. 73, no. 11. — ISSN 1550-2368.
5. Minimal walking technicolor: Setup for collider physics / R. Foadi [et al.] // Physical Review D. — 2007. — Vol. 76, no. 5. — ISSN 1550-2368.
6. *Sannino F.* Conformal Dynamics for TeV Physics and Cosmology. — 2009. — arXiv: 0911.0931 [hep-ph].
7. *Gudnason S. B.*, *Kouvaris C.*, *Sannino F.* Dark matter from new technicolor theories // Physical Review D. — 2006. — Vol. 74, no. 9.
8. *Khlopov M. Y.*, *Kouvaris C.* Composite dark matter from a model with composite Higgs boson // Physical Review D. — 2008. — Vol. 78, no. 6.
9. *Khlopov M. Y.*, *Kouvaris C.* Strong interactive massive particles from a strong coupled theory // Physical Review D. — 2008. — Vol. 77, no. 6.
10. *Khlopov M. Y.* New symmetries in microphysics, new stable forms of matter around us. — 2006. — arXiv: astro-ph/0607048 [astro-ph].
11. Effects of new long-range interaction: Recombination of relic Heavy neutrinos and antineutrinos / K. M. Belotsky [et al.]. — 2005. — arXiv: astro-ph/0504621 [astro-ph].

12. *Belotsky K.*, *Khlopov M.*, *Shibaev K.* Stable quarks of the 4th family? — 2008. — arXiv: 0806.1067 [astro-ph].

13. *Belotsky K. M.*, *Khlopov M. Y.*, *Shibaev K. I.* Composite Dark Matter and its Charged Constituents. — 2006. — arXiv: astro-ph/0604518 [astro-ph].

14. *Beylin V. A.*, *Khlopov M. Y.*, *Sopin D. O.* Charge Asymmetry of New Stable Families in Baryon Asymmetrical Universe // Symmetry. — 2023. — Vol. 15, no. 3. — ISSN 2073-8994.

15. *Antognini A.*, *Kottmann F.*, *Pohl R.* Laser spectroscopy of light muonic atoms and the nuclear charge radii // SciPost Phys. Proc. — 2021. — P. 021.

16. *Angeli I.*, *Marinova K.* Table of experimental nuclear ground state charge radii: An update // Atomic Data and Nuclear Data Tables. — 2013. — Vol. 99, no. 1. — P. 69–95. — ISSN 0092-640X.

17. The helion charge radius from laser spectroscopy of muonic helium-3 ions / K. Schuhmann [et al.] // Science. — 2025. — Vol. 388, no. 6749. — P. 854–858. — eprint: https://www.science.org/doi/pdf/10.1126/science.adj2610.

18. Measuring the α-particle charge radius with muonic helium-4 ions / J. Krauth [et al.] // Nature. — 2021. — Vol. 589. — P. 527–531.

19. *De Vries H.*, *De Jager C. W.*, *De Vries C.* Nuclear charge and magnetization density distribution parameters from elastic electron scattering // Atom. Data Nucl. Data Tabl. — 1987. — Vol. 36. — P. 495–536.

20. *Берестецкий В. Б.*, *Лифшиц Е. М.*, *Питаевский Л. П.* Квантовая электродинамика. Т. 4 / под ред. Е. М. Лифшиц. — 2-е изд. — Москва : Наука, 1989. — С. 728. — (Теоретическая физика). — ISBN 5-02-014422-3. — Авторы: В. Б. Берестецкий, Е. М. Лифшиц, Л. П. Питаевский.

ПРИЛОЖЕНИЕ

СПИСОК СТАТЕЙ И ДОКЛАДОВ, ОПУБЛИКОВАННЫХ ЗА ШЕСТОЙ СЕМЕСТР

Статьи:

- A Dark Atom Solution for Direct Dark Matter Investigation. Universe/P. Belli, R. Bernabei, V.A. Beylinet al. // Universe. 2026. Vol. 12, No. 4. Article 116 https://doi.org/10.3390/universe12040116

Доклады:

- Interaction of heavy multiply charged particles with light nuclei during Big Bang nucleosynthesis, The 3rd International Online Conference on Universe, Satellite Workshop, 4-6 и 9 марта, онлайн

universe

MDPI

Article

A Dark Atom Scenario for Direct Dark Matter Investigation

Pierluigi Belli [1,2,†], Rita Bernabei [1,2,†], Vitaly Beylin [3,†], Timur Bikbaev [4,5,†], Artem Kharakhashyan [4,†], Maxim Khlopov [3,*,†], Vladimir Korchagin [4,†], Andrey Mayorov [5,†] and Danila Sopin [4,5,*,†]

1 Istituto Nazionale di Fisica Nucleare (INFN), Sezione Roma Tor Vergata, I-00133 Rome, Italy; pierluigi.belli@roma2.infn.it (P.B.)
2 Dipartimento di Fisica, Università di Roma "Tor Vergata", I-00133 Rome, Italy
3 Virtual Institute of Astroparticle Physics, 75018 Paris, France
4 Institute of Physics, Southern Federal University, Stachki 194, Rostov-on-Don 344090, Russia; bikbaev.98@bk.ru (T.B.); aharahashyan@sfedu.ru (A.K.)
5 Institute of Nuclear Physics and Engineering, National Research Nuclear University MEPhI, Moscow 115409, Russia; mayorov.a.g@gmail.com
* Correspondence: khlopov@apc.univ-paris7.fr (M.K.); sopin@sfedu.ru (D.S.)
† These authors contributed equally to this work.

Abstract

This paper extensively explores the concept of dark atoms, hypothetical stable lepton-like particles with a charge of $-2n$ (where n is any natural number) that form neutral bound states with n primordial helium nuclei. The discussion begins with the introduction of multiply charged stable particles. Next, the formation and evolution of dark atoms are examined, followed by a review of related constraints. The capture of dark atoms by the Earth and implications for direct dark matter search are subsequently discussed. Then, the quantum-mechanical description of bound states between dark atoms and ordinary nuclei is addressed. Moreover, procedures for systematic comparisons with this model, which have general interest, are presented considering the DAMA published results on the dark matter annual and diurnal modulation signatures as a benchmark.

Keywords: composite dark matter; stable charged particles; dark atoms; low-energy bound state; annual modulations; diurnal modulations; DAMA/LIBRA experiment; anomalous isotopes

1. Introduction

The cosmological paradigm requires dark matter (DM) as dominant matter component in the Universe; this is further supported, e.g., by investigations on large-scale structures formation, on behavior of galaxies, on gravitational lensing, and on anisotropy of cosmic microwave background. A large DM candidate particle zoology beyond the standard models of fundamental interactions has been made available for investigations on their nature, dynamic characteristics and observability. When candidates arisen by extension of the Standard Model (SM) of electroweak and strong interactions of elementary particles are considered, the non-baryonic nature of DM implies the existence of new stable forms of nonrelativistic matter, whose stability assumes that they have new conserved charges, which SM particles do not have, reflecting a new strict symmetry that extends the SM symmetry. In this article, the dark atom scenario for dark matter is discussed in some detail, outlining its peculiarities. A dark atom consists of the new heavy particle X^{-2n} (without or with strongly suppressed QCD interaction) with even negative charge and nuclei of ^{4}He, bound by ordinary electromagnetic Coulomb force. This scenario does not

Academic Editors: Ivan De Martino, Kazuharu Bamba and Panayiotis Stavrinos

Received: 19 January 2026
Revised: 6 March 2026
Accepted: 9 April 2026
Published: 15 April 2026

involve new physics, with the exception of X^{-2n}, and reduces the effects of dark atoms on the nuclear interaction of their nuclear shells. Multiple charged stable particles arise in several possible extensions of the Standard Model as, e.g., the model of a minimal walking technicolor (WTC) [1–6], considered here. In the latter model, the existence of additional heavy fermions with new gauge interaction is assumed, and the Higgs boson physics is formulated in terms of a single scalar doublet describing the Higgs boson as a composite particle. This similarly leads to a new approach revealing the composite nature dark matter. This WTC approach becomes of special interest since, if the SUSY energy scale corresponds to much higher energies than the electroweak scale, the problems of the Standard Model (divergence of the Higgs boson mass and the origin of the electroweak energy scale) may need a non-supersymmetric solution, which may be provided by models of a composite Higgs boson. The basic description of the dark atom model is given in [7] and references therein. In this paper, the dark atom model is discussed in detail, focusing in particular on the relevant parameters in light of the annual and diurnal DM modulation signatures. As a benchmark, we consider the already published results from the ultra-low-background (ULB) experimental setups DAMA/NaI, DAMA/LIBRA–phase1, and DAMA/LIBRA–phase2. Notably, these experiments, spanning over 22 independent annual cycles and different detector configurations, confirm an annual modulation effect, satisfying all the requirements of this signature, at more than 13 σ C.L.; see [8–10] and references therein. A wide literature (see, e.g., in publications list of [10]) is available discussing the realization and features of these setups, the possible sources of systematic uncertainties, and, to some extent, comparisons with other experiments employing different target materials and/or other approaches (e.g., those relying on background subtraction based on inherently uncertain background models). The published results on the investigation of the diurnal modulation signature [11], as well as the measured energy spectrum reported in [12], are also considered.

For completeness, we briefly comment on the recent results of ANAIS-112 and COSINE-100 [13] (see also [8]). Although these collaborations state that their setups are the same as DAMA/LIBRA because they use NaI(Tl) crystals, the experiments differ substantially in detector characteristics, setup configurations and operational procedures, exposure, background conditions, and data-analysis methods [8]. Among other differences, their total accumulated exposures are significantly smaller than that accumulated by DAMA/LIBRA, implying lower statistical sensitivity and less precise control of uncertainties. Moreover, in the few-keV region relevant for the DAMA signal, their counting rates ($\simeq$2–5 counts/day/kg/keV) are considerably higher than those of DAMA/LIBRA ($\simeq$0.5–1.0 counts/day/kg/keV) and exhibit a strong time dependence, making the extraction of a small annual modulation signal more challenging. Additional differences arise from the experimental sites: COSINE-100 and ANAIS-112 operate with a smaller overburden than Gran Sasso National Laboratory, resulting in different residual cosmic-ray fluxes and background levels. Furthermore, the determination of efficiencies associated with event-selection cuts in COSINE-100 and ANAIS-112 introduces non-negligible systematic uncertainties that can affect sensitivity to a small modulation effect. In view of these differences, the DAMA results used in this paper, covering both the annual and diurnal modulation signatures, as well as additional analyses, can be regarded as a benchmark for studies of the dark atom model across its possible detection strategies. On the other hand, the procedures discussed here are of general relevance and applicability to the field. In particular, in regards to the DAMA benchmark, their application shows that the dark atom framework consistently accounts for the observed DAMA annual modulation while remaining compatible with the absence of modulation signals in experiments based on heavy nuclei.

Furthermore, we also recall that other significant activities employing different target materials and experimental strategies are ongoing, such as XENON-nT [14] and CDMS [15], while for NaI-based detectors the SABRE experiment [16] is currently in preparation. Finally, it should be emphasized that the DAMA effect remains compatible with a wide range of theoretical models, particularly in view of the substantial uncertainties that persist in astrophysical, nuclear, and particle-physics aspects [10].

This paper provides a detailed description of the dark atom scenario, including model-independent signatures and their possible interconnected analyses. The resulting methodology and framework can be of even broader interest than the specific applications discussed here. With the above-described aim, this paper is organized as follows:

1. Section 2 is dedicated to aspects and properties of Multiple charged stable particles, discussing: (i) New stable quarks; (ii) Multiple charged leptons; (iii) Charged constituents of composite Higgs boson.
2. Section 3 is dedicated to dark atom formation and evolution, discussing: (i) Balance of baryon asymmetry and electroweak charged particle excess; (ii) Capture by primordial helium—formation of dark atoms and problem of anomalous isotopes overproduction.
3. Section 4 is dedicated to experimental constraints on the properties of multiply charged heavy particles and generally the dark atom model.
4. Section 5 is dedicated to dark atom capture by Earth and Direct dark matter search, discussing (i) Monte Carlo Simulations; (ii) Annual and diurnal modulations of the signal.
5. Section 6 is dedicated to the quantum mechanical description of the bound states of dark atom with the nuclei of matter, discussing (i) Binding of the nucleus of substance to a dark atom in the total effective interaction potential of the OHe–nucleus system; (ii) Calculation of the radiative capture cross-section in the OHe–nucleus system.
6. Section 7 is dedicated, as a benchmark, to a comparison with the published experimental results of DAMA: (i) Annual modulation; (ii) Diurnal modulation; (iii) High-energy gamma rays.
7. Section 8 addresses the constraints of the dark atom model parameters derived by applying the DAMA results as a benchmark.
8. Section 9 is dedicated to conclusions.

2. Multiple Charged Stable Particles

2.1. New Stable Quarks

Elementary (at a certain level) particles of matter, fermions, are either neutral (with zero electric charge) or have electric charges $q = \pm 1$. However, when forming bound systems (atoms, molecules, clusters), composite (not necessarily stable) objects with electric charges $|q| > 1$ are possible—these are ionized atoms or molecules. More precisely, within the Standard Model (SM) only fundamental neutrinos are absolutely neutral. Objects which participate in strong interaction are composite and fractionally charged quarks are those initial "building blocks" from which neutral and charged complexes can be built including multi-particle states with charges $|q| >> 1$. However, these obvious statements should be overcome when considering extensions of the SM which is inevitable bearing in mind the SM generic problems mentioned in the Introduction.

Let us note right away that the understanding and studying of the existence of fundamental objects with large charges have led to experimental searches for hypothetical (multi- or milli-charged) particles (see [17–24] and references within) with charges $|q| >> 1$. The main goal of searching for these objects is to study the traces of their interaction with matter, which are distinctive due to the high ionizing ability of these particles. They can be observed in specific astrophysical events in our Galaxy and found in cosmic rays generating

unusual extensive air showers (EAS) in the Earth atmosphere; manifestations of such particles can be detected by ground-based observatories such as LHAASO, Augier, IceCube, Baksan and Baikal observatories, and others [25–28]. Besides the ATLAS detector, special experimental setup, MoEDAL, was used also at LHC to search signals of multi-charged particles (experiment MoEDAL [17,20,29]). Note, however, that the results of these searches did not demonstrate any obvious traces of multi-charged particles establishing only some limitations on their masses for various charges.

New heavy (vector-like) quarks, $m_Q > m_t$, can result from various BSM scenarios-grand unified, little Higgs or hypercolor [30–34]. In the models with a fourth family of quarks [35–37] or with an additional heavy singlet quark [38,39], probable problems with the Higgs boson parameters can be substantially decreased if the mixing of the SM quarks with the new ones is small. Stability or decay channels of new heavy mesons and baryons, i.e., charged bound states like $Q\bar{Q}$ or QQQ, would be analyzed in more detail. However, this study is not yet completed.

In any case, such new fundamental or composite objects from the SM extensions could be stable or long lived to avoid unwanted signals in the well-studied energy regions and be interpreted as possible hidden mass carriers. As of recent, there are no clear signals generated by heavy (at $O($ TeV$)$ scale) multi-charged states from colliders, ground-based experimental setups or from space telescopes.

Additional vector-like quarks arise in hypercolor models and their masses should be lighter than the scale of hypercolor confinement if an analogy with the QCD is used. Further, formation and manifestations of H-mesons and H-baryons can be considered in the framework of linear $\sigma-$ model predicting some interesting phenomena at colliders and in astrophysics due to special type of multi-component dark matter [33]. However, an emerging of heavy unstable states with $|q| > 1$ in the H-color scheme is not considered. Note that stable exotic H-mesons with $|q| = \pm 1/2$ arise in $SU(6) \to Sp(6)$ generalization of hypercolor [34]; their bound (stable?) multi-charged or neutral states can be produced at early stages of evolution, but this question was not studied in detail. Nevertheless, some interest in the SM extension of such type is maintained, for example, in the consideration of the 2HDM model with additional heavy vector-like quarks [33,40–44].

There is also an interesting scenario with the fourth family of new leptons where the Higgs should be composite (this construction emerges from walking technicolor [1–6] considered with different possibilities to mix standard fermions with the new one). In this way, meta-stable heavy charged leptons can be introducedm and possible signals of such objects have been described [45,46].

Now, we can refer to the modified gauge group $SU(3) \times SU(2) \times SU(2)' \times U(1)$ where the SM fermions can be converted to the so called terafermions by operation of the CP transformation. This left–right symmetric model (it is referred also as the sinister model [47]) where the numbers of ordinary and tera-fermions are equal contains heavy gauge W, Z bosons due to the CP breaking which is naturally introduced in the Higgs $SU(2) \times SU(2)$ doublets. Additional (tera)fermions are also massive. Dirac neutrinos are provided by small mass resulting from seesaw, and so, as a result of this doubling of the number of fermions, we obtain some set of new heavy objects—the lightest fundamental terafermions which are stable (teraelectron and teraquark, U, with electric charge $q_U = 2/3$ and mass $m_U \sim$ (1–3) TeV) and new massive composite states, like terahelium; it is formed by electromagnetic interaction.

We remind that the search of heavy (multi-)charged new states, fundamental or bounded, is based on the analysis of ionization losses (and corresponding radiation) of a charged particle which is moved in some media. The quantitative characteristics of such signals strongly depend on the value of electric charge, mass, velocity and structure of such

object which can be neutral but is formed by bounded charged components. In this way, the candidates for the dark matter can be built as well: they can be made from terafermions in the sinister models, for example. However, the most elaborated, detailed, and interesting in terms of the link to results of the DAMA experiments, considered here as a benchmark, is the dark atom model based on the Walking Technicolor extension of the SM [5–7].

2.2. Multiple Charged Leptons

So, new heavy quarks emerging from various scenarios not only participate in strong and EW interactions but can form charged bound states with $|q| > 1$. At the same time, in the SM extensions, other new fermions can appear, namely charged leptons. For example, almost-commutative geometry generates two heavy fermions with $|q| = 2$ which do not change the SM characteristics because the mixing of them with the SM light fermions can be made very small. The new leptons should be (nearly) stable with large masses which are generated without using the Higgs mechanism. If the additional (electromagnetic) $U(1)$ symmetry is exact, such leptons will be absolutely stable, and then some manifestations of such particles can be seen in experiments [17,48]. New fermions with opposite charges can bound forming specific neutral "atoms" which can be considered as the hidden mass candidates.

A lot of interesting possibilities follow from the technicolor model, especially if we consider its extended variant, more exactly the so-called Walking Technicolor. Here, the gauge technicolor couplings vary slowly ("walk") in some energy ranges; as a result, dangerous FCNC are absent at leading order and the model can be used for the ordinary mesons and techni-meson description. Moreover, the light (in a comparison with the techni-scale) Higgs boson find one's niche in this SM extension. The minimal WTC [49,50] operates with U, D techniquarks transforming under $SU(2)$ technicolor gauge group, global $SU(4)$ symmetry breaks to $SO(4)$, so the EW symmetry breaks down by the chiral condensate of techni-quarks. Heavy techni-mesons are bound states UU, UD, DD with non-zero techni-baryon numbers [51] and the lightest techni-baryon can be stable (see also the akin hypercolor model with the stable lightest hyperpion [52]). Importantly, the WTC model allows for techni-baryon-specific values of electric charges: n, $n \pm 1$ where n is an arbitrary real number.

In addition, the minimal WTC model contains an additional generation of leptons, techni-electron and techni-neutrino, which have the following hypercharges: $3y/2$, $((3y \pm 1)/2$. So, in the special case $y = 1$, the UU state and the new lepton have $q = 2$ and the minimal WTC predicts an existence of two stable doubly-charged particles, the technibaryon and the technilepton with masses significantly exceeding the EW scale. Stability of new mesons and leptons is determined by possibility of mixing these techni-particles with the SM generations. For example, the mixing between new heavy neutrino and light standard neutrinos can be strongly forbidden; nevertheless, heavy new leptons can mix with standard leptons. Then, for the case of large mass of new neutrino, new charged lepton is nearly stable. So, new fermions from the additional fourth generation can possess large charges and be nearly stable at the same time. Note that possible problems with Higgs boson can be diminished considering the Higgs boson as composite particle made from these new objects.

2.3. Charged Constituents of Composite Higgs Boson

It is an old idea to introduce the Higgs boson as some composite state instead of an elementary scalar using dynamical symmetry at a scale higher than the EW symmetry breaking one. In fact, models of the composite Higgs (CHM) originate from the various SM extensions where new fermions and/or bosons arise as a consequence of additional

symmetry at some high energy scale (∼(1–10) TeV) [53]. Some of these new degrees of freedom can be the Higgs boson components bounded by new (strong) interactions. Then, known quadratic ultra-violet divergences in the Higgs boson mass should be eliminated by contributions of the new strong interactions at some high energy scale.

New (heavy) particles not only work as strongly bounded parts of the Higgs scalar but can form new mesons and baryons. Some traces (direct or not) of such particles (techni-quarks, -leptons and their bound states, new mesons and baryons), in principle, can be observed at colliders, other grounded or underground setups, or manifested in astrophysical events which can be seen at space telescopes as some direct or indirect fingerprints of new particles [5,6,49,51,54].

Signals from possible events generated by such objects of BSM physics depend on the way of the Higgs composite state arising: as a bound state produced, for instance, in the Technicolor framework, or resulted from the extended symmetry breaking (as a Goldstone boson) [55–59]. Certainly, the Technicolor scheme is sufficiently different from its initial variant having known problems with the top-quark mass and unobserved signals from flavor-changing neutral currents (FCNC); the path to the modern TC passes through the extended technicolor to the walking TC model which is free from these old defects and has somewhat other strong dynamics at high energy scale. These new strong interactions operate on a scale higher than that of the EW and QCD condensates, $v = 246$ GeV; then the model symmetry is close to the conformal one.

As estimated, new TC states can be manifested starting at the scale ∼ (1–10) TeV. An important feature of the presence of heavy charged techni-fermions is their ability to form some (possibly neutral and stable) bound states with ions and/or nucleus of matter [60] (see also Section 1). Another way to have the light Higgs boson in the theory with additional high scale is to consider the vacuum state which is misaligned with the EW vacuum, so the new energy scale is sufficiently higher that the EW one [57]. Here, a composite sector consists of hyperquarks which are charged under an asymptotically free hypercolour gauge group. Further, at a high scale of compositeness, bilinear hyperquark condensates emerge and the global symmetry breaks to some subgroups. It means that to obtain light (in comparison with the new energy scale) Higgs boson, the global symmetry breaking results in a number of Nambu–Goldstone bosons produced. So, the Higgs boson is one of these states which should obtain nonzero mass when the Higgs state is transformed to pseudo-Nambu–Goldstone after the EW symmetry breaking. Note that in the extended TC, we also tried to keep both heavy top-quark and light Higgs boson using the so-called fine-tuning of the model parameters. So, in this scheme, the Higgs boson can also be considered as the composite object appearing in the framework of the new strong dynamics with the techniparticles participation.

Summarizing, in various scenarios to replace the elementary Higgs scalar with some compound state, the SM extensions should operate with the extended symmetry groups, global and/or gauged, where the symmetry breaking can result in the (pseudo-) Nambu–Goldstone boson emerging which can be interpreted as the light Higgs. Or, considering other ways, this scalar can be formed by new charged components from various modifications of the TC.

Importantly, all possible schemes of the Higgs boson compositeness simultaneously add to the EW scale standard particles some new objects at higher scale, for example, heavy charged techni-quarks and techni-leptons in the WTC. These new objects, which are used for the Higgs boson construction, should be manifested in some processes at colliders or in astrophysics events and taken into account for the EW Peskin–Tackeuchi parameters. They can form unique neutral stable states. Such objects, so-called dark atoms, can be considered as the hidden mass candidates [60].

3. Dark Atom Formation and Evolution

3.1. Balance of Baryon Asymmetry and Electroweak Charged Particle Excess

A necessary condition for dark atom formation is an excess of negatively charged particles over the corresponding antiparticles. In this context, the process of sphaleron transitions may be considered as the main way to produce the required density of new heavy particles. While it is well known that sphaleron transitions cannot be the only source of the baryon asymmetry, this non-perturbative process may nevertheless play a significant role in related mechanisms. Indeed, new heavy families described in the previous section have weak charges, and consequently they should participate in sphaleron processes. After the formation of particle excess over the antiparticle at very high temperatures (the mechanism is not important), sphaleron transitions, as the last baryon number violating process, should provide the observed ratio of densities of light and heavy species. This scenario has been described for the case of the SM [61] and WTC model [5,6,62]. In [62], the model with a successive fourth generation was also considered.

Number densities can be expressed in the form of linear combinations of chemical potentials, which depend on the masses of the particles and the temperature. For instance, the baryon number density is defined as

$$\begin{aligned} B = \frac{6}{gT^2}(n_b - n_{\bar{b}}) = \frac{6}{gT^2}\sum_i \frac{1}{6} g\, T^3\, \frac{\mu_i}{T}\, \sigma\left(\frac{m_i}{T}\right) = \\ = \frac{1}{3}\cdot 3\cdot (2+\sigma_t)(\mu_{uL}+\mu_{uR}) + \frac{1}{3}\cdot 3\cdot 3\cdot (\mu_{dL}+\mu_{dR}), \end{aligned} \tag{1}$$

where in the first line the summation is carried out over all flavors of quarks. Their masses are included in equations as the argument $z = \frac{m}{T}$ of the weight functions

$$\sigma(z) = \begin{cases} \frac{6}{4\pi^2}\int_0^\infty \mathrm{d}x\, x^2 \left(\cosh\left(\frac{1}{2}\sqrt{x^2+z^2}\right)\right)^{-2}, & \text{for fermions;} \\ \frac{6}{4\pi^2}\int_0^\infty \mathrm{d}x\, x^2 \left(\sinh\left(\frac{1}{2}\sqrt{x^2+z^2}\right)\right)^{-2}, & \text{for bosons} \end{cases} \tag{2}$$

showing the particular species of particles in equilibrium. However, in the SM sphaleron, transitions freeze out at $T_* \approx 131\,\mathrm{GeV}$ [63], which is sufficiently high to neglect all SM particle masses except only the t- quark [5]. The resulting system of equations is complemented by the electric charge neutrality conditions and the relations among the chemical potentials obtained from electroweak processes (decays and sphaleron transitions). The exact kind and number of these conditions depend not only on the model but also on the temperature. For instance, the temperature of the standard electroweak phase transition (EWPT) is $T_c = 159$ GeV [63], which is quite close to T_*. The modifications of the electroweak sector assumed by composite Higgs models should change both temperatures. Therefore, it may be useful to consider both cases (standard $T_c > T_*$ and modified $T_c < T_*$). Also, a new charge conservation law adds an equation to the system.

In this paper, only the system of equations for the standard $T_c > T_*$ case is written out to demonstrate the described idea. The standard baryon and lepton number densities can be found as [5,6,61]

$$B = (10+2\sigma_t)\mu_{uL} + 6\mu_W, \tag{3}$$

$$\begin{aligned} L = \sum_i (\mu_{\nu_i L} + \mu_{\nu_i R} + \mu_{iL} + \mu_{iR}) = \\ = 4\mu + 6\mu_W, \end{aligned} \tag{4}$$

where $\mu_{iR/L}$ are the chemical potentials of right/left particles of i flavor, μ_W corresponds to the W^- boson and $\mu = \sum \mu_{\nu_i L}$. The additional conditions are $\mu_{iR} = \mu_{iL} \pm \mu_0$ and $\mu_i = \mu_j + \mu_W$, where $\mu_0 = 0$ in the $SU(2)$-broken phase. Similar conditions can be found for new particle families if the new number densities (forth/techni baryon and lepton numbers) are introduced. Conditions of neutrality assume zero density of charges: $Q = \sum_i \sigma_i \mu_i = 0$, $Y = \sum_i \sigma_i \mu_i = 0$ for electric and new $U(1)$ (if it is included in the model) charges. Sums are over all charged particles. The last equation describes the sphaleron transitions:

$$3(\mu_{uL} + 2\mu_{dL}) + \mu + (\mu_{UL} + 2\mu_{DL}) + \mu_{NL} = 0. \tag{5}$$

In WTC model, it is more convenient to use another form of this condition, where $\mu_{UL} + 2\mu_{DL} \to \frac{1}{2}\mu_{UU} + \mu_{DD}$. In the case of the model with additional generation, one should consider heavy quarks to write down a correct Y-neutrality condition. However, there is no new $U(1)$ symmetry in the technicolor model, and, consequently, the chemical potentials of bound states of techniquarks could be found.

The solution to the resulting system of equations is a ratio of number densities as a function of masses, temperature, ratios of other numbers and some model parameters. For instance, the model with the fourth generation gives

$$\frac{FB}{B} = -\alpha(\sigma_i)\left(\frac{L}{B} + \beta(\sigma_i)\right), \tag{6}$$

where α and β are functions of all weight functions. In the simplest approximation ($\sigma_E = \sigma_D = \sigma_U, \sigma_N = 1, \sigma_t = 1$), they look like

$$\alpha = \frac{\sigma_U(3\,\sigma_U^2 + 26\,\sigma_U + 19)}{16\,\sigma_U^2 + 116\,\sigma_U + 60}, \quad \beta = \frac{9\,\sigma_U^2 + 74\,\sigma_U + 61}{3\,\sigma_U^2 + 26\,\sigma_U + 19}. \tag{7}$$

Because the first of them decreases exponentially, the masses of new particles cannot be too high to describe the observed ratio of dark and baryonic matter densities, which could be found as

$$\frac{\Omega_{DM}}{\Omega_b} = \frac{3m_U}{m_b}\left|\frac{FB}{B}\right|, \tag{8}$$

where $m_b \approx 0.931\,\text{GeV}$ is a baryon mass. This is shown in Figure 1. The approximation $\sigma_E = \sigma_D = \sigma_U, m_N = 50\,\text{GeV}$ was used. The observed ratio $\frac{\Omega_{DM}}{\Omega_b}$ is denoted by the red line, whereas the right-hand side of (8) is plotted for different values of the $\frac{L}{B}$ ratio. The lowest value $\frac{L}{B} = -3$ is set based on the experimental limits on the masses of new charged particles $m_{UUU} > 1060\,\text{GeV}$ [64]. The highest value $\frac{L}{B} = \frac{n_b - n_{\bar{b}}}{n_l - n_{\bar{l}}} \approx 6.6 \cdot 10^6$ follows from the modern restrictions on lepton asymmetry [65]. Therefore, the approximate upper limit on the ANO-helium mass could be set:

$$m_{\text{ANO-He}} \lesssim 11\,\text{TeV}. \tag{9}$$

Similar calculations for the WTC model are complicated due to the lack of an Y-neutrality equation and multi-component nature of dark matter (technibaryones and technileptones). Therefore, the system of equations reduces only to

$$\begin{aligned} &\frac{TB}{B} + \gamma(\sigma_i)\frac{TL}{B} = -\alpha(\sigma_i)\left(\frac{L}{B} + \beta(\sigma_i)\right), \\ &\frac{m_{UU}}{m_b}\left|\frac{TB}{B}\right| + \frac{m_{N/E}}{m_b}\left|\frac{TL}{B}\right| = \frac{\Omega_{DM}}{\Omega_b}. \end{aligned} \tag{10}$$

Since the charges of the new particles depend on model parameters, several cases can be considered. First of all, it is possible to find the allowed L/B ratio values for different combinations of density signs. So

$$\frac{L}{B} = -\beta(\sigma_i) - \frac{\delta}{\alpha(\sigma_i)} \frac{m_b}{m_{N/E}} \frac{\Omega_{\rm DM}}{\Omega_b}, \tag{11}$$

where for signs (TB,TL):
$(+-)$ $\delta \in [-\frac{m_{N/E}}{m_{UU}}, \gamma(\sigma_i)]$;
$(-+)$ $\delta \in [-\gamma(\sigma_i), \frac{m_{N/E}}{m_{UU}}]$;
$(\pm\pm)$ δ is in region with borders $\{\pm\gamma(\sigma_i), \pm\frac{m_{N/E}}{m_{UU}}\}$.

If the signs of the densities differ, these regions include the experimentally allowed one $|L/B| < 6.6 \cdot 10^7$ at high masses. Furthermore, the allowed values of the ratio $\frac{TB}{TL}$ reduce to $-\gamma(\sigma_i)$ exponentially fast, which means that the left side of the first equation in (10) vanishes. However, this does not give any constraints on masses.

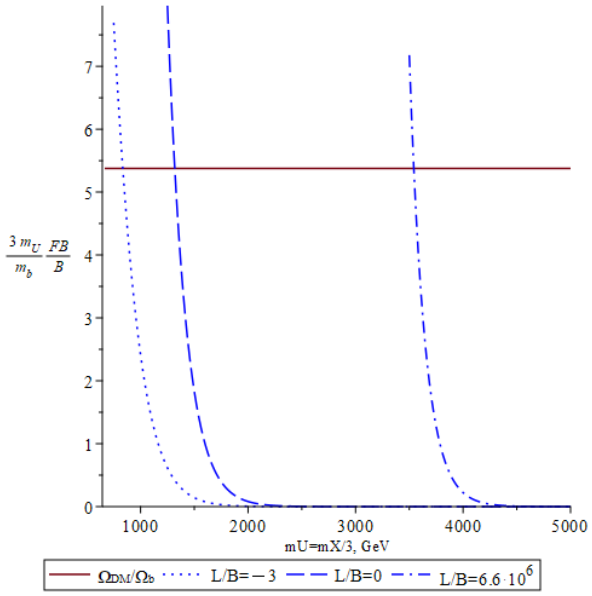

Figure 1. Dependence of number densities on mass of new heavy quark.

If the signs of the densities are the same, the allowed regions become non-overlapping at high masses. Therefore, the restrictions can be found. In the simplest assumption ($\sigma_{UU} = \sigma_{UD} = \sigma_{DD} = \sigma_N = \sigma_E$) the particles cannot be heavier than $m_{\rm crit} \approx 3.6\,$TeV. Moreover, the positively charged component should be strongly suppressed, which is possible only at the boundary of the allowed parameter region.

In summary, the mass constraints obtained from the sphaleron transitions depend strongly on the model. If the number of equations in the system is enough, the upper limit can be set using the modern lepton asymmetry data. Because of the exponential suppression (or growth [62]) of the density ratio caused by particles falling out of thermodynamic equilibrium, the maximal mass value cannot be arbitrarily large.

3.2. Capture by Primordial Helium—Formation of Dark Atoms and Problem of Anomalous Isotopes Overproduction

After the generation of an excess of negatively charged particles X^{-2n}, the dark atom's nuclear shell should be formed. The description of such dark recombination is complicated, on the one hand, by the multi-stage nature of the process at high charges and on the other by the necessity of accounting for the finite nuclear size. Unfortunately, these two features

cannot be considered separately. Therefore, the interaction of heavy X^{-2n} with light nuclei produced at the nucleosynthesis stage should be considered first.

There are four types of $2 \to 2$ reactions possible:

$$N^1 + N^2 \to N^3 + \gamma/N^4, \tag{12}$$

$$X + N \to XN + \gamma, \tag{13}$$

$$XN^1 + N^2 \to XN^3 + \gamma/N^4, \tag{14}$$

$$XN^1 + XN^2 \to X_2N^3 + \gamma/N^4. \tag{15}$$

Here, N^i denotes an ordinary light nucleus. Reactions of the first type are standard and therefore their properties are well established experimentally. The evolution of concentrations is described by standard Big Bang nucleosynthesis theory (SBBN) (see the book [66] for example). Reactions (13) are the first stage of dark atom recombination. The type of nucleus captured at the beginning should determine the further chain of reactions (14). The interaction (15) of two bound states of heavy core X^{-2n} should be rare due to the low expected concentration of such particles. In all three types (13)–(15) one can see the possibility of charged bound state overproduction. There should be distinguished negatively charged states (dark ions), neutral particles (dark atoms) and anomalous isotopes with a positive electric charge.

The reactions should affect the primordial concentrations of ordinary nuclei. A similar effect is well described in the case of singly negatively charged particles [67–69]. The results were extrapolated on doubly charged states [70]. In both cases, the overproduction of primordial metals and anomalous isotopes is expected. The processes in the nuclear shell of the *O*He dark atom leading to the catalytic formation of helium from deuterium were considered in [71]. However, the result of modified nucleosynthesis may significantly depend on the value of the X^{-2n} electric charge. It could be shown with the qualitative estimation of the temperatures of dark atom recombination. Let us assume that all DM density of the Universe is provided by heavy multicharged particles. The second assumption is that the first stage of dark recombination (13) with one of $N \in \{p, d, t, {}^3\mathrm{He}, {}^4\mathrm{He}\}$ becomes possible due to the high-energy photon density drops sufficiently. Only the XN_i dark ions are produced because all other reactions are neglected. Then the analogue of the Saha equation could be written:

$$n_N(T) = \frac{g_X g_N}{g_{XN}} \left(\frac{m_N T}{2\pi E_{XN}} \right)^{3/2} \exp\left(-\frac{E_{XN}}{T} \right), \tag{16}$$

where g_i are the number of spin degrees of freedom of particles, E_{XN} is the dark ion binding energy. The solution to this equation

$$T_{\mathrm{rec}} \approx E_{XN} \cdot \left(\ln\left(\frac{g_X g_N}{g_{XN}} \left(\frac{m_N}{2\pi E_{XN}} \right)^{3/2} \frac{m_b\, T_0^3}{\rho_c\, \Omega_b} \frac{1}{Y_N} \right) \right)^{-1} \tag{17}$$

depends on the usual constants like the baryonic density of the Universe Ω_b and N nucleus mass m_N, parameters that can be calculated with SBBN theory (concentration $Y_N = \frac{n_N}{n_b}$ at temperature T_0) and unknown values g_X, E_{XN}. However, spin coefficients are not significant, as they are under the logarithm.

Binding energies of dark ions should be estimated numerically. In the general case, it is necessary to solve the eigenvalue problem for the Schrodinger equation, which describes

the atom with a finite-sized nucleus. For the first estimation, the oscillator potential [72] can be used:

$$V(r) = \begin{cases} -\dfrac{Z_X Z_N \alpha}{2R_N}\left(3 - \dfrac{r^2}{{R_N}^2}\right), & r < R_N \\ -\dfrac{Z_X Z_N \alpha}{r}, & r > R_N \end{cases} \quad (18)$$

Therefore, the nucleus in a shell of the dark atom is modeled as a uniformly charged sphere of radius R_N, whose value for light elements is well known experimentally [73–76]. Such a system can be characterized by the ratio of radii $a = \frac{R_N}{r_B} = Z_X Z_N \, \alpha \, m_N \, R_N$. Two parameter regions are usually distinguished [60,72]: $0 < a < 1$—Bohr-like dark atoms and $a > 1$ when the system is more like a quantum spherical oscillator (or Thomson's plum pudding). However, in practice, significant deviations from the Bohr pattern occur already at $a \sim 0.3$. The tables with the particular ground state energies of the five isotopes under consideration are presented in Tables 1–5.

Table 1. Properties of X^{-2n}–p bound states.

		p				
	q	2	4	6	8	10
Radii	R_N, Fm			0.841 [73]		
	r_B, MeV^{-1}	0.073	0.037	0.024	0.018	0.015
	a	0.058	0.115	0.173	0.230	0.288
E_{XN}	E_{XN}^{Coulomb}, MeV	0.100	0.400	0.900	1.599	2.500
	E_{XN}^{Sphere}, MeV	0.100	0.396	0.883	1.550	2.388

Table 2. Properties of X^{-2n}–d bound states.

		d				
	q	2	4	6	8	10
Radii	R_N, Fm			2.127 [73]		
	r_B, MeV^{-1}	0.037	0.018	0.012	0.009	0.007
	a	0.291	0.583	0.873	1.165	1.456
E_{XN}, MeV	E_{XN}^{Coulomb}	0.200	0.799	1.798	3.196	4.994
	$E_{XN}^{\text{Oscillator}}$	—	—	—	0.604	1.762
	E_{XN}^{Sphere}	0.191	0.701	1.439	2.343	3.370

Table 3. Properties of X^{-2n}–t bound states.

		t				
	q	2	4	6	8	10
Radii	R_N, Fm			1.7591 [74]		
	r_B, MeV^{-1}	0.0244	0.0122	0.008	0.006	0.005
	a	0.361	0.721	1.082	1.443	1.803
E_{XN}, MeV	E_{XN}^{Coulomb}	0.299	1.197	2.692	4.787	7.479
	$E_{XN}^{\text{Oscillator}}$	—	—	0.288	1.666	3.176
	E_{XN}^{Sphere}	0.280	1.005	2.023	3.242	4.608

Table 4. Properties of X^{-2n}–^{3}He bound states.

		^{3}He				
	q	2	4	6	8	10
Radii	R_N, Fm			1.970 [75]		
	$r_B, 10^{-3}\,\mathrm{MeV}^{-1}$	12.20	6.10	4.07	3.05	2.44
	a	0.808	1.615	2.423	3.230	4.037
E_{XN}, MeV	$E_{XN}^{\mathrm{Coulomb}}$	1.196	4.786	10.768	19.142	29.910
	$E_{XN}^{\mathrm{Oscillator}}$	—	1.894	4.767	7.888	11.164
	E_{XN}^{Sphere}	0.978	3.094	5.740	8.690	11.837

Table 5. Properties of X^{-2n}–^{4}He bound states.

		^{4}He				
	q	2	4	6	8	10
Radii	R_N, Fm			1.678 [73,76]		
	$r_B, 10^{-3}\,\mathrm{MeV}^{-1}$	9.19	4.60	3.06	2.30	1.84
	a	0.913	1.826	2.739	3.652	4.566
E_{XN}, MeV	$E_{XN}^{\mathrm{Coulomb}}$	1.588	6.352	14.291	25.406	39.698
	$E_{XN}^{\mathrm{Oscillator}}$	—	2.713	6.195	9.950	13.878
	E_{XN}^{Sphere}	1.256	3.891	7.130	10.708	14.506

Using any simple nuclear potential to describe the X–N system, one does not take into account changes in the internal structure of the nucleus. Indeed, at high values of the a-parameter the Coulomb repulsion should be suppressed due to charge screening. Changes in the structure of the nucleus have not been considered earlier. The modern methods of nuclear physics allow for the simulation of ordinary light nuclei with good agreement with experiment (see [77–81]). However, such a study is beyond the scope of this paper, and therefore it is reasonable to make the simplest assessment. It could be suggested that the screening effect leads to an increase in the binding energy $E_{XN} \to E_{XN} + Q$, where Q is the energy difference between the ground state of the free and bound nucleus. Simultaneously, the mass of the nucleus in the shell of the dark atom should decrease: $m_N \to m_N - Q$. Assuming that all Coulomb repulsion is compensated, it can be set $Q \approx 0.711 \frac{Z(Z-1)}{A^{1/3}}$.

The calculated dark ion recombination temperatures are shown in Table 6. There are both charge screening assumptions used for helium. The first number corresponds to the state with ordinary structure (E_{XN} and m_N) and the second one is found in the case of full Coulomb compensation. The difference between these two values is about 30 keV. For most charges of heavy core X^{-2n}, there is no significant difference (colored gray). Since the bound state with a modified structure is harder to destroy, OHe begins to form earlier (colored blue), which can lead to changes in the final concentrations of particles. At low values of the charge parameter $n \leq 3$, capturing of hydrogen becomes possible after helium formation and therefore should be suppressed due to low concentration of unbound X-particles. However, if $n = 4$, two processes ($X + \mathrm{H} \to \ldots$ and $X + \mathrm{He} \to \ldots$) start to compete (colored orange). Finally, at high values of the charge parameter $n \geq 5$, hydrogen capturing as the first stage of dark atom recombination dominates (colored red) because it starts before helium formation. This may be an indication of the overproduction of oddly charged bound states, which is a significant problem. The interpretation of this

effect is difficult due to the multi-stage dark recombination at high charges. The accurate consideration of all reactions with dark ions is required.

Table 6. Temperatures of the first stage of dark atom recombination calculated with Saha formula. The color shows different scenarios (see the description in text).

n	T_{rec}, keV				
	p	d	t	^{3}He	^{4}He
1	3	4	6	22–46	36–64
2	12	16	21	73–98	119–147
3	29	34	42	139–164	223–253
4	51	56	69	214–239	342–372
5	81	83	99	294–320	470–501

A rigorous calculation of dark matter particles implies solving the system of kinetic equations for an expanding Universe. Consequently, the problem is reduced to the estimation of the cross-sections of radiative recombination σ_{rr} and photoionization σ_γ reactions. They should be averaged over the maxwellian distribution by the energy of the incident nucleus.

However, different reaction types require distinct approaches. For instance, the first steps (13) are similar to the ordinary hydrogen atom recombination with scaled masses and charges. The analytical Stobbe formula ([82] and references within) can be used for ground state photoionization:

$$\sigma_\gamma = \frac{2^9\pi^2}{3}\frac{Z_N}{Z_X}\frac{r_B}{m_N}\frac{\eta^8}{(1+\eta^2)^4}\frac{\exp\left(-4\eta\arctan(\eta^{-1})\right)}{1-\exp\left(-2\pi\eta\right)}, \tag{19}$$

where $\eta = (r_B p_N)^{-1}$, p_N is a moment of the nucleus, and $r_B = (Z_X Z_N \alpha m_N)^{-1}$. The cross-section of recombination may be obtained by detailed balance

$$\sigma_{rr} = \frac{2E_\gamma^2}{p_N^2}\sigma_\gamma = \frac{1}{2m_N^2 r_B^2}\frac{(1+\eta^2)^2}{\eta^2}\sigma_\gamma. \tag{20}$$

Moreover, the transitions to excited states can be taken into account using the rescaled semiclassical Kramer's formula [82]:

$$\langle\sigma_{rr}v\rangle = \frac{2^5}{3}\sqrt{\frac{\pi}{3}}\frac{Z_N}{Z_X}\frac{1}{m_N^4 r_B^2}\sqrt{\frac{E_{XN}^{\text{Coulomb}}}{T}}\left(\ln\left(\frac{E_{XN}^{\text{Coulomb}}}{T}\right)+\gamma\right), \tag{21}$$

where $\gamma = 0.5772$ is an Euler constant. Unfortunately, this approximation is valid only for Bohr-like dark atoms. If the charge values are high, a finite-size nucleus significantly affects the cross-section. Then, for the recombination in the ground state, it can be calculated numerically:

$$\langle\sigma_{rr}v\rangle = \frac{2\sqrt{2\pi}}{3}\frac{Z_N}{Z_X}\frac{1}{m_N^4 r_B^5}\frac{1}{(mT)^{3/2}}\int\frac{1+\eta^2}{\eta^4}\exp\left(-\frac{1}{2m_N r_B^2 T}\frac{1}{\eta^2}\right)\left|\int\rho^2 R_{p_N 1}(\rho)\partial_\rho R_{10}(\rho)d\rho\right|^2 d\eta, \tag{22}$$

where $\rho = r/r_B$, $R_{kl}(\rho)$ and $R_{n_{st}l}(\rho)$ are the radial wave parts of the functions. The Schrödinger equation with a spherically symmetric potential should describe the system with sufficient accuracy.

The treatment of third-type reactions (14) is complicated by the presence of nuclear interaction. Accounting for the structure of nuclei and spins requires computationally

intensive numerical calculations. However, for most processes, the first estimation of the reaction rate may be made with an approximation of the scalar X^{-2n} and the unchanged form of nuclei. Then, it is necessary to consider only the vanishing (or suppressed) Coulomb barrier. Experimental values of cross-sections scaled by an inverted exponential factor would provide a qualitative understanding of BBN outcomes. Nevertheless, there remains a small subset of reactions that lack standard analogues. First of all, it is the process of bound state formation with the ^{8}Be nucleus. There are two stages of helium capture. The additional reaction with ^{4}He may lead to the catalyzed production of XC bound states or free carbon via a process analogous to the stellar triple-α reaction. A similar situation may arise for the proton-rich isotopes of beryllium, boron and carbon. Such reactions should be especially important at high values of the charge parameter n and demonstrate that reaction networks for different charge values may differ not only due to additional recombination stages but also through the opening of new intermediate reactions and changes in the rates of all other processes. The formation of ^{5}Li nucleus in the shell dark atom is suppressed. The simple estimation of the nuclear binding energy shows that even full compensation of Coulomb repulsion is not enough to make this isotope stable. Only the ion-like bound state without nuclear fusion (XHe)p is possible if $n \geq 4$. The calculation of the corresponding cross-sections is nontrivial. As has already been mentioned, the analogical three-body problems were considered for singly charged stable particles [69]. The obtained rates were rescaled for the doubly charged state ($n = 1$) by stripping off the Coulomb barrier [70]. The overproduction of both anomalous isotopes and primordial metals was predicted.

The interaction of two dark ions (15) may be significant only for low values of heavy core mass and high temperatures. Indeed, it is possible if at least

$$n_{XN}\langle\sigma v\rangle t \approx \frac{3}{4\pi}\sqrt{\frac{5}{\pi g_*}}\frac{\rho_c\,\Omega_{DM}^{\rm now}\,m_{Pl}}{T_{\rm now}^3}\cdot\frac{T}{m_X}\langle\sigma v\rangle > 1, \tag{23}$$

where m_{Pl} is the Planck mass and g_* is the number of ultrarelativistic degrees of freedom at the considered temperature. Otherwise, such processes freeze out. For a typical nuclear cross-section

$$\sigma \approx 10^{-25}\,\mathrm{cm}^2, \tag{24}$$

it occurs earlier than a sufficient number of dark ions are formed.

3.3. Dark Atom Scenario of Large-Scale Structure Formation

At the Radiation Dominance (RD) stage momentum and energy exchange between dark atoms and cosmic plasma, the dark atom component should be kept in thermal equilibrium with plasma and radiation. In this period, radiation pressure converts dark atom density fluctuations in acoustic waves. It leads to slight suppression of the small-scale fluctuations. This suppression is not as effective as strong power-law suppression due to free streaming of few keV mass particles in ordinary Warm Dark Matter (WDM) scenarios. At temperatures $T < 1$ keV, energy transfer in the interaction of dark atoms with plasma becomes ineffective, since $n_b\sigma(m_p/m_o)vt < 1$, where n_b is baryon density, m_p and m_o are correspondingly masses of proton and dark atom, and σ is given by Equation (24). Then, decoupling of dark atom gas from plasma and radiation takes place, making dark atoms Warmer than Cold dark matter [83].

The dark atom gas does not follow baryonic matter in formation of astrophysical objects, since, e.g., in the Galaxy averaged baryonic matter density makes it transparent for dark atoms. However, any baryonic density nonhomogeneity with size R and number density n_m satisfying the condition $n_m\sigma R > 1$, where σ is given by Equation (24), is opaque for dark atoms. Dark atoms behave as collisionless gas at the galactic scales [83] but

they can be captured by any dense baryonic nonhomogeneity, in which the condition $n_m\sigma(m_p/m_o)R > 1$ is satisfied. This condition is evidently satisfied for stars and planets and all the dark atoms from halo, which enter them, are captured.

During stellar evolution, all the dark atoms captured by star can merge with nuclei and after SN explosion ordinary nuclei can be accompanied by anomalous component, in which nuclei are merged with dark atoms. If over 10^7 years, the star passes a stage of the red giant with a radius of surface of about 10^{13} cm, it captures at this stage the dark atom flux about $10^4/(\text{cm}^2\text{s})$, which gives the total amount of dark atoms of about 10^{45}. In the star, together, there are present about 10^{55} ordinary nuclei before a Supernova explosion. After explosion, these anomalous nuclei are accelerated together with ordinary nuclei and the ratio of anomalous to ordinary nuclear component should be of order 10^{-10}, which may be within the reach of the AMS02 experiment.

4. Experimental Constraints on Dark Atoms

The key assumption of the dark atom model is the existence of a heavy multi-charged composite particle X^{-2n}. Such states can be produced in electroweak processes at high-energy colliders. Therefore, it is possible to set direct constraints on the particle's mass and charge values. For instance, the results of the LHC searches for heavy, long-lived multi-charged particles are summarized in Table 7. The minimal X^{-2n} masses depend on the charge, but it can generally be assumed that $m_X \geq$ 2–3 TeV. The ATLAS [64] signal efficiency does not allow for setting constraints in the case $n \geq 4$. For this reason, the results on R-hadron searches [19,21] cannot be directly applied to the dark atom scenario. In the case of small charges, the restrictions are not much stricter ($m > 2.27$ TeV gluino R-hadrons). However, the analysis of the Full MoEDAL Detector provides mass limits for particles with electric charge in the range $10e$ to $400e$ [17]. For X^{-10}, which was considered in the previous section, it is only $m_X >$ 300–790 GeV. The proper analysis accounting for the positronium-like annihilation of heavy particles sets constraints on such charges that can be significantly strengthened [20]. For instance, depending on the spin of X $m_X >$ 2000–2800 GeV for $n = 4$. Similar analysis was not carried out for $n \geq 5$ in the literature. Therefore, it can only be assumed that, in this case, the mass of the multiply charged particle should be greater than 3 TeV.

Table 7. The minimal X^{-2n} masses allowed by the LHC data [18,20,64].

$2n$	2	4	6	8	10
m_X, GeV	1060 [64]	1520 [64]	1600 [64]	∼2800 [20]	790 [18]

The neutral bound state $X^{-2n}(^4\text{He}^{++})_n$ is a finite-size composite object that interacts with ordinary matter through both nuclear forces and an induced electromagnetic dipole moment. Consequently, the results of the Strongly Interacting Massive Particle (SIMP) search can be applied to dark atoms [84,85]. In particular, the expected dark atom masses and the cross-sections of elastic interaction with ordinary matter fall within the sensitivity reach of the XQC experiment. This X-ray calorimeter collected about 100 s of data [86] that were analyzed in terms of the elastic coherent scattering of point-like particles. However, it was pointed out [87] that dark atoms should be incoherent, and these particles may give rise to less than 0.1 of the expected background events. Moreover, the XQC sensitivity decreases at high masses. Further research confirms that such analysis is inapplicable to finite-size particles [88,89]. Nevertheless, changes should not be significant if there is a light nucleus in the shell of a dark atom [90]. For high values of heavy core X^{-2n} charge, and in the case of anomalous isotope scattering, the resonant suppression of the elastic cross-section is possible. A more accurate estimate is needed for the probability that a dark

atom produces a discernible signal in the XQC detector. However, it cannot be high because of the short duration of that experiment.

In regards to the direct dark matter particle searches, the results of most experiments are interpreted within the framework of recoil nuclei. However, this approach is not applicable to the dark atom model. Indeed, due to the high (nuclear) elastic cross-section value, such bound state would lose energy rapidly; therefore, the production of recoil nuclei in underground detectors is extremely unlikely. Moreover, at atomic scales, dark atoms look like neutral particles. The Van der Waals interactions are expected to be strongly suppressed due to the small size of the object. Only in nuclear-scale processes may the dipole character of this bound state become significant. For a similar reason, constraints on millicharged particles [91] cannot be applied directly. The interaction of dark atoms with the atomic electron shell and crystal lattice was not rigorously considered. Therefore, constraining this model using recoil electron search results (in particular [92] or [93]) remains a task for future research.

The strongest experimental constraints may be obtained from searches for anomalous isotopes [94–97] and primordial metals [65]. Samples of seawater, atmospheric gases, and terrestrial metals were examined for the presence of such particles using various methods. These searches have not yielded any candidates for superheavy isotopes of light elements (H, He, Li, Be, B, C, O, F, Na). Constraints on concentrations in relation to ordinary nuclei at the level of 10^{-10}–10^{-23} depending on the mass and charge were set. In light of the ongoing discussion, it is particularly interesting that the concentration of anomalous sodium (both types of bound states: $(XN)^{+11}$ and $(XN)^{0}$-Na) is limited to less than 10^{-12} of the total particle number [94]. However, the correct theoretical prediction of the abundance of such particles requires a treatment of the reactions of nuclear fusion in cosmological nucleosynthesis, astrophysical processes and terrestrial matter that is currently lacking.

The modified Big Bang nucleosynthesis has already been partially discussed in the previous section. The interaction of dark atoms with light nuclei may lead to the overproduction of heavy particles with non-compensated electric charge. Nevertheless, the formation of such states is a multi-stage process for all values of the charge parameter n. The large number of stages leads to the prolongation of the overall dark atom recombination timescale. Accordingly, anomalous isotope production may be suppressed if the heavy core has a high charge. Additionally, the formation of positively charged states should be partially compensated by exchange reactions and processes involving shell fragmentation $XN_1 + N_2 \rightarrow XN_3 + N_4 + \ldots$. Although this mechanism leads to another problem: an excess of primordial metals. The case of doubly charged particles O^{--} has been extensively studied in the literature [70]. The huge enhancement of lithium and beryllium isotope concentrations, arising due to nuclear fusion of the dark atom shell with deuterium and helium-3, represents a major challenge to the model. However, if $n > 1$, the energy release in these reactions may be insufficient to produce free nuclei.

Generally, dark atoms act as a sink for light nuclei during Big Bang nucleosynthesis. In the simplest case of the bound state of a doubly charged particle OHe, the concentration of free primordial helium should decrease by at least $\Delta Y_p = 4\frac{m_b}{m_X}\frac{\Omega_{\rm DM}}{\Omega_b} \sim 10^{-2}$–$10^{-3}$. Such a deviation could be detected. Indeed, this cosmological parameter is known from the spectra of ordinary atomic recombination with high accuracy: $Y_p = 0.2448 \pm 0.0033$ [98]. The similar estimation for helium-3 yields the same result. Combined with uncertainties from fragmentation processes, this indicates that reproducing the observed primordial elemental abundances in the dark atom model may require fine-tuning of parameters. Not only mass and charge, but also the baryon-to-photon ratio should be varied. Moreover,

careful consideration of all reactions is necessary to set the correct constraints. The theoretical predictions required for this remain a task for future work.

Dark atoms may be ionized in high-energy astrophysical processes (accretion onto black holes, blazars, supernovae). It leads not only to a specific spectrum but also to the flow of anomalous isotopes. Indeed, a temperature of a few tens MeV ($\sim 10^{11}$–10^{12} K) should be enough to initiate photodetachment and further re-recombination with heavy nuclei produced in stellar nucleosynthesis for any type of bound state. However, the temperature inside the stars is usually lower, which may lead only to nuclear fusion processes in the shells of dark atoms.

Due to the strong interaction, dark atoms lose their energy and drift towards the center of the planet/star. Therefore, the maximum concentration of such particles in the Earth should be located somewhere in the core.

5. Dark Atoms Captured by Earth and Direct Dark Matter Search

In this section, we describe the phenomenology associated with dark atom interactions in an underground detector environment. In particular, with this aim, we consider here as benchmark the results already published by the highly radiopure NaI(Tl) DAMA set-ups, sensitive to both DM candidates giving rise to nuclear recoils or, as in the present case of dark atoms, to electromagnetic signals. The availability of published experimental results on dark matter annual and diurnal modulation signatures as well as some information on energy spectrum allow us to introduce a complete strategy for such kind of analyses.

The highly radiopure NaI(Tl) DAMA set-ups [10], located at the Gran Sasso underground laboratory (LNGS) in Italy, latitude 42°25′16″ N (42.42111° N) and longitudes 13°30′59″ E (13.51639° E)), were shielded from cosmic rays by about 3600 meters water equivalent (m.w.e.) of rock. The location, as well as the technological and operative procedures, provides a very low-background environment, which is crucial for rare event investigations. The sensitive target material of the second-generation DAMA/LIBRA consists of highly radiopure sodium iodide crystals doped with thallium (NaI(Tl)). The total target mass is about 250 kg, arranged in a 5 × 5 matrix of 25 detectors, each weighing 9.7 kg. Each crystal is coupled to two low-background photomultiplier tubes (PMTs) operating in coincidence at the single photoelectron level. The crystals are encapsulated in copper housing and placed within a multi-layer shield consisting of low-radioactivity copper, lead, cadmium foils, polyethylene, and paraffin, along with an external concrete shield from local rock; moreover, a three-level system for exclusion of radon present in trace in the laboratory environmental air is operative. This complex shielding drastically reduces the contribution from environmental background due to neutrons and gamma rays [10].

In the following subsection, the effect of the rock surrounding the DAMA NaI(Tl) set-up(s) is parametrized through dedicated modeling and Monte Carlo simulations. Then, the time dependence of a dark matter signal in the highly radiopure NaI(Tl) detectors is described, focusing on the model-independent signatures provided by annual and diurnal modulation effects.

5.1. Monte Carlo Simulations

We assume that the dark matter particles are dark atoms propagating from the solar neighborhood and penetrating the Earth during rotation of the solar system around the center of the Galaxy. The dark matter particles propagating inside the Earth slow down to the thermal velocity of the Earth's crust and diffuse towards its center. During this process, the bound states of the dark matter particles may occur so the particles can be detected by underground detectors such as that used in the DAMA/LIBRA experiment.

The particle propagation inside the Earth can be modeled using stochastic Monte Carlo method combined with several empirical assumptions. We assume that beam's propagation obeys an ideal exponential extinction law similar to optical analogy known as the Beer–Bouguer–Lambert absorption. According to this law, the beam intensity I decreases exponentially depending on the mean free path l. In our case, each beam is characterized by a directional vector $\vec{d}_{beam}$ in the spherical coordinate system with the origin at the detector. To keep the reference to the real coordinates, we use a geodetic coordinate system with the azimuthal angle φ measured counterclockwise from the East direction. The polar angle θ is measured relative to the normal vector to the Earth's surface. For convenience, the beams are indexed starting at the azimuthal axis, so the angle between the azimuthal axis and each beam direction is given by the expression $\theta_{beam} = \frac{\pi}{2} - \theta$. In a spherical coordinate system with regular angular beaming, the solid angle is formed by four adjacent beams and varies depending on the proximity to the poles. The flux of dark matter through a finite surface element (polygon) also varies depending on the direction of the arrival of the particles. The surface area of the solid angle formed by four neighboring beams can be calculated as follows:

$$S_{i,j} = R^2 \cdot \frac{2\pi}{n_\varphi} \left(\sin \frac{(i+1)\pi}{2n_\theta} - \sin \frac{i\pi}{2n_\theta} \right), \tag{25}$$

where $i = 0, 1, \ldots, n_\theta - 1$ and $j = 0, 1, \ldots, n_\varphi - 1$ are the elevation and azimuth division indices, respectively. Since all polygons of the same elevation have the same surface area, the j index, which describes azimuthal divisions, can be omitted.

The propagation of particles within each beam can be described as random processes. The Brownian motion of the dark matter particles can be modeled using modification of the Wiener random process $W(t)$, which is a continuous-time random process with the following set of properties: $W(0) = 0$, $W(t) - W(s)$ and $W(m) - W(t)$ are independent increments, the process is almost surely continuous, $W(t) - W(s)$ for $0 \leq s \leq t$ have normal distribution $\mathcal{N}(0, t - s)$.

We consider a three-dimensional case with the directions of arrival of the beam linked to the orientation and velocity of the Earth, determined through ephemerides. Since the direction of particle propagation changes during the thermalization process, after which the particles start to move towards the center of the Earth, we employ a combined Brownian motion with drift model, in which the particles move with thermal velocities given by a Maxwell–Boltzmann distribution with mean $\approx V_{drift}$. The mean value is estimated using Equation (3) from [60]:

$$V = \frac{g}{n\sigma v} \approx 80 S_3 A_{med}^{1/2} \text{ cm/s} \tag{26}$$

where g is the standard acceleration of gravity, $A_{med} \sim 30$ is the average atomic weight in terrestrial surface matter, $n = 2.4 \cdot 10^{24}/A$ is the number density of terrestrial atomic nuclei, σv is the rate of nuclear collisions, S_3 is the mass of the dark atom. The probability density function of the Maxwell–Boltzmann distribution is as follows:

$$f(x) = \sqrt{\frac{2}{\pi}} \frac{x^2}{a^3} e^{-\frac{x^2}{2a^2}}. \tag{27}$$

The histogram for the simulated drift velocity distribution is shown in Figure 2.

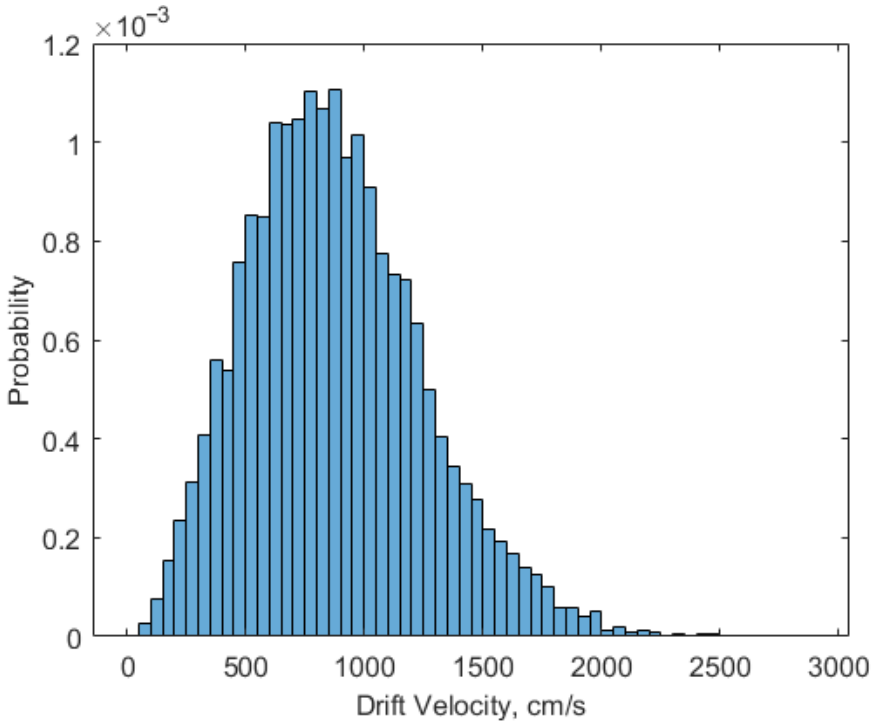

Figure 2. Simulated drift velocity distribution.

At the thermalization depth $d_{th} \approx 100$ m, the flow of particles is thermalized, and the process of diffusion towards the center of the Earth begins; thus, the direction of the flow changes, and the directional vector of the beam is pointed towards the center of the Earth. The average estimated drift timescale, based on [60], is expected to be $t_{dr} = 2.5 \cdot 10^2 S_3^{-1}$ s, while the exact time depends on the direction of arrival of the particle, entrance point into the surface, and the trajectory. The points of intersection of the beams with the Earth's surface are used to determine the starting points of the diffusion process.

For a set of N_p particles, the equations of motion can be defined using Brownian motion with drift:

$$\boldsymbol{BP}(x, y, z, t) = \sigma_{BM}^2 \boldsymbol{BM}(x, y, z, t) + \vec{V}_p^T \times \vec{V}_{drift} \cdot t, \tag{28}$$

where $\boldsymbol{BM}(x, y, z, t)$ represents the standard Brownian motion processes, described in terms of Wiener processes, x, y, z are the beam-specific coordinates of the particles; $\sigma_{BM}^2 = 1$ is the Brownian motion scale, $\vec{V}_p$ is a row vector of size N_p sampled from Maxwell–Boltzmann distribution, $\vec{V}_{drift} = (0, 0, -1)$ is the drift direction vector. The beam intensity is associated with the number of simulated particles within the Brownian motion model and can be calculated as follows:

$$I(\varphi, \theta_{beam}, d, t) = I_0(\varphi, \theta_{beam}, t) \cdot e^{\frac{-d}{l}}, \tag{29}$$

$$I_0(\varphi, \theta_{beam}, t) = n_{beam} \cdot V_{beam}(t) \cdot S_{\theta_{beam}, \varphi}, \tag{30}$$

$$V_{beam}(t) = \left|\vec{V}_{full}(t)\right| \cdot \cos\left(\vec{d}_{beam}, \vec{V}_{full}(t)\right), \tag{31}$$

where I is the beam intensity, I_0 is the initial beam intensity, d is the distance traveled by beam, and l is the mean free path, V_{beam} is the projection of system's velocity vector $\vec{V}_{full}(t)$ onto the beam, n_{beam} is the initial concentration.

The resulting dark atom concentration n at time t can be estimated as the number of particles inside the detector, divided by the volume of the detector:

$$n(t) = \frac{N_p(t)}{Vol}. \quad (32)$$

The detector geometry is modeled as the 5×5 set of 10.2 cm $\times$ 10.2 cm $\times$ 25.4 cm blocks unified into a single parallelepiped with the widest and highest facet facing geodetic north.

The detection process is influenced by many factors, such as topography, detector depth, detector geometry, position and velocity of the Earth, as well as the relative velocities of the Earth and the detector with respect to the moving particles (Figure 3). Local effects on the signal may occur due to the direction of the detector velocity vector and possible blocking of the beams by the terrain. These effects should be calculated using precise estimates of the coordinates and the velocities of all involved objects, and taking into account the reference frame of a specific epoch using ephemeris data.

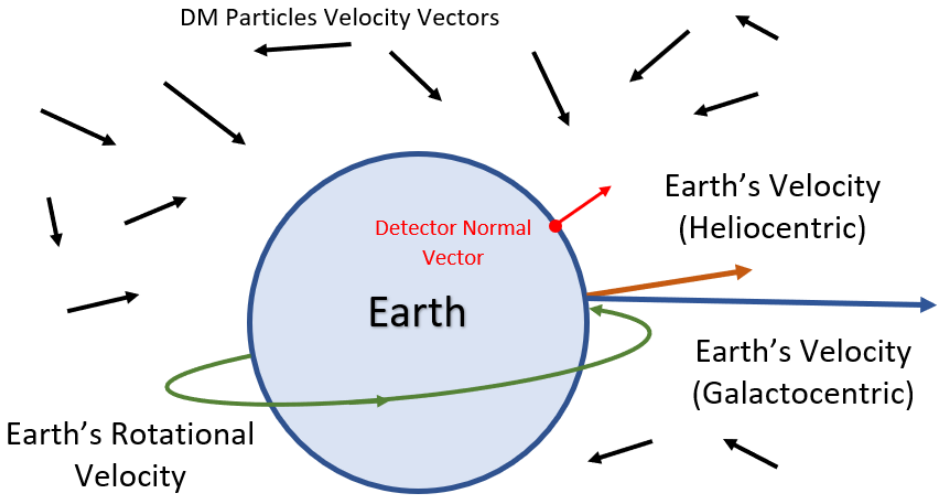

Figure 3. Schematic representation of the influence of the directions of relative velocities and of Earth's shadowing on the detection of dark matter particles.

5.2. Annual and Diurnal Modulations of the Signal

The concept of annual modulation as a dark matter signature arises from the motion of the Earth relative to the galactic dark matter halo. As the Earth orbits the Sun, its velocity relative to the dark matter halo changes, leading to a periodic modulation in the flux and velocity distribution of incoming dark matter particles.

The detector moves through the presumably non-rotating dark matter halo of the Milky Way. The velocity distribution of the Milky Way halo stars is close to gaussian with the velocity variance about 110 km/s (Brown et al., 2010) [99]. We can assume that the dark matter particles have the same velocity distribution as the observed halo objects; therefore, particles bombard a detector moving through the dark matter halo with the velocity of $\approx$240 km/s from all directions. During rotation of the Earth around the Sun and the rotation of the Earth around its axis, the velocity vector of the detector changes its value and the direction relative to the non-rotating dark matter halo. As the detector moves through the sea of the dark matter halo, the particles penetrate into the detector through all its faces. Therefore, neither the yearly velocity modulations of a detector caused by the rotation of the Earth around the Sun nor changing of orientation of the detector due to the diurnal rotation of the Earth can directly lead to oscillations of the signal. In the first case, a decrease in the flow of the dark matter particles through the leading face of a detector is compensated by an increase in the flow via the detector's back face and vice versa. Changing in orientation

of the vector of a detector due to the Earth's rotation which causes a decrease in the flow of the dark matter particles through the leading detector's face simultaneously increases the flow through other faces of the detector so the total flow of the particles into the detector remains constant. However, the situation changes if the beam entering the Earth's surface at different points on the surface can be affected by the geological details of the relief, leading to shadowing or even to a complete blocking of the flow, if the beams come from the opposite side of the planet in relation to the detector. This effect leads to annual and diurnal oscillations of the detected signal.

In order to take into account all possible velocity variations, we calculate the total velocity vector of the system. The laboratory velocity with respect to the galactic halo can be expressed as:

$$\vec{v}_{lab}(t) = \vec{v}_{LSR} + \vec{v}_{\odot} + \vec{v}_{rev}(t) + \vec{v}_{rot}(t), \tag{33}$$

where $\vec{v}_{LSR}$ is the Local Standard of Rest (LSR) velocity due to galactic rotation, $\vec{v}_{\odot}$ is the peculiar solar velocity with respect to the LSR, $\vec{v}_{rev}(t)$ is the Earth's orbital velocity around the Sun, and $\vec{v}_{rot}(t)$ is the rotational velocity of the detector associated to the Earth's rotation about its axis [100].

The annual velocity modulation arises primarily from the $\vec{v}_{rev}(t)$ term, which changes sign relative to the Sun's velocity in June (maximum flux) and December (minimum flux), while the diurnal modulation is given by the $\vec{v}_{rot}(t)$ velocity, as shown in Figure 4.

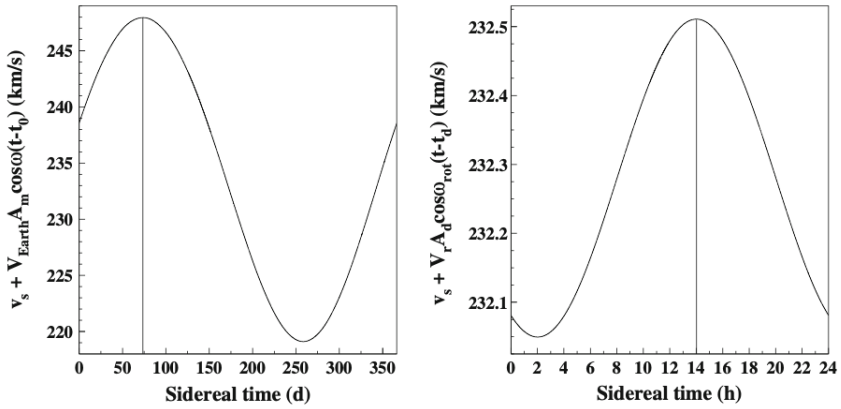

Figure 4. Velocity components and expected phase locations as a function of sidereal time (from Ref. [11]). (**Left**): velocity of the Earth in the galactic frame with starting point March 21 (around spring equinox). The contribution of diurnal rotation (the fourth term in Equation (33)) is dropped off. The maximum of the velocity (vertical line) is about 73 days after the spring equinox. (**Right**): sum of the Sun velocity in the galactic frame and of the rotation velocity of a detector at LNGS as a function of the sidereal time. The maximum of the velocity is about at 14 h (vertical line). For details, see ref. [11].

Beam directional vectors are converted to the Geocentric Celestial Reference System (GCRS). The time-dependent velocity vector of the lab $\vec{v}_{lab}(t)$ is calculated in GCRS at time t using ephemeris data. Then, the total velocity vector of the system $\vec{V}_{full}(t)$ can be written as follows:

$$\vec{V}_{full}(t) = \vec{v}_{lab}(t) + \vec{v}_{DM}, \tag{34}$$

where $\vec{v}_{DM}$ is the velocity of the dark matter particles according to [99].

Another factor directly related to Earth's topography that can have a significant impact on the particle detection process and lead to the observation of diurnal modulation is the length of the path that particles travel within the Earth's surface. During the day, as the detector rotates around the Earth's rotation axis, the potential arrival area of particles with the highest relative velocities also changes, driven by the Earth's velocity vector. At the same

time, terrain features rotate with the detector, causing particles to enter the Earth's crust at different points, angles, and velocities, consequently leading to time-dependent changes in their propagation paths. To account for these phenomena and the potential influence of terrain, a topographic map of the Earth can be used. In this work, we use a topographic map of the earth provided by NASA (https://visibleearth.nasa.gov/images/73934/topography, accessed on 15 August 2024). This map represents a pixel-by-pixel approximation of altitude as a function of latitude and longitude. A fragment of the topographic map covering the area of interest is shown in Figure 5. Using these data, we can reconstruct a three-dimensional map of the Earth's surface in the vicinity of the detector and apply a simplified ray tracing procedure to determine the entry points of the rays into the Earth's crust. The three-dimensional approximation is shown in Figure 6 in two projections.

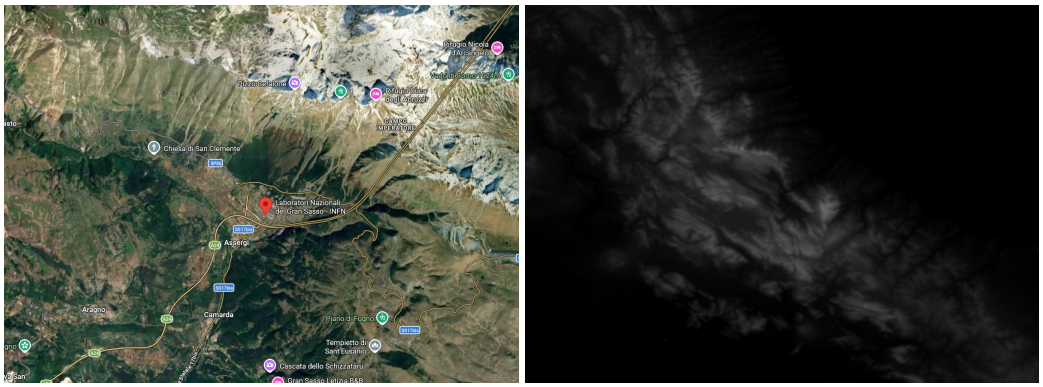

Figure 5. Satellite photography and topographic representation of the area around the Laboratori Nazionali del Gran Sasso: Google Maps image and satellite photography of the area (**left**); Black-and-white elevation map showing the height above sea level, where completely black indicates sea level (**right**).

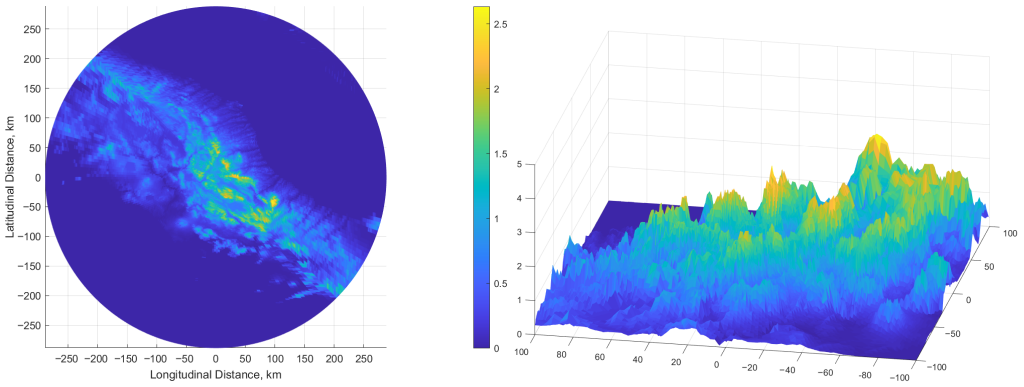

Figure 6. A three-dimensional reconstruction of the area around the detector. The color scale indicates altitude above sea level: top view (**left**); close-up view of the region around the detector (not to scale) (**right**).

For each azimuthal angle φ, there is a half-plane passing through the normal vector to the Earth's surface and the direction vector of each beam with the same φ; this half-plane is perpendicular to the azimuthal plane. For each such half-plane, we calculate the intersection points between the two-dimensional interpolated topographic approximation of the Earth's surface and the linear segments defined by the directional vectors $\overline{d}_{beam}$, representing beams (Figure 7). The first point of each segment is at the detector, and the second point lies on the surface of a semi-sphere of radius $R = 288$ km, which covers the entire area of interest.

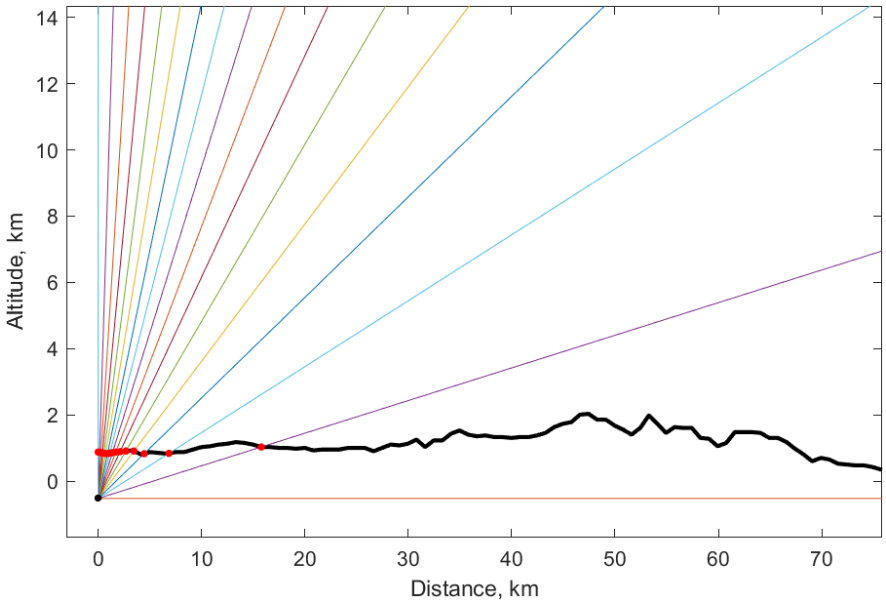

Figure 7. Schematic representation of beams passing through the Earth's surface: each colored line denotes the trajectory of beam propagation along its directional vector without taking into account thermalization: red dots denote the points of beam entry into the Earth's surface, black dot represents the detector; the thick black line denotes the relief of the Earth's surface.

Within the framework of the beam approximation approach, we determine the coordinates of dark matter particles as they propagate through the Earth's surface and record changes in concentration inside the detector, taking into account the direction of arrival of the particles, the distances traveled in the Earth's crust, and variations in flux caused by changes in the Earth's velocity and orientation, with reference to real coordinates and time.

6. Quantum Mechanical Description of the Bound States of Dark Atom with the Nuclei of Matter

6.1. Binding of the Nucleus of Substance to Dark Atom in the Total Effective Interaction Potential of the OHe-Nucleus System

The varied results from direct dark matter detection experiments highlight the complexities in interactions between dark matter particles and materials in underground detectors. The *X*-helium hypothesis offers—together with the existing experimental and theoretical astrophysical, nuclear, and particle physics differences and uncertainties, and the targets—one of the possible explanations of the different experimental results among various experiments on the direct search for dark matter particles. Here, it mainly arises because of the peculiarities of the interaction of dark atoms with the matter of underground detectors.

The deceleration of cosmic *X*He in the Earth's soil does not allow direct methods of detecting dark matter particles based on the search for the recoil effects of nuclei in collisions of WIMPs with the nuclei of ordinary matter. However, the interaction of slow *X*-helium atoms with nuclei can lead to their low-energy binding, which is explained by the following reaction:

$$A + (^4\mathrm{He}^{++}X^{--}) \rightarrow [A(^4\mathrm{He}^{++}X^{--})] + \gamma. \quad (35)$$

It is assumed that within the uncertainty limits of the parameters of nuclear physics, there is a range in which the binding energy in the *X*He-Na system is in the range of 2–4 keV [83], which is a rather subtle effect. The capture of dark atoms in this bound state

leads to a corresponding release of energy, which is observed as an ionization signal in the DAMA detector. The concentration of *X*He in the substance of underground detectors is determined by the equilibrium between the incoming cosmic flux of dark atoms and their diffusion to the center of the Earth. The presence of *X*-helium in the Earth's soil is rapidly regulated due to the kinematics of the interaction of dark atoms with matter, taking into account the incoming cosmic *X*He, and follows a change in this flow. Therefore, the rate of capture of dark atoms should experience annual modulations reflected in the annual modulations of the ionization signal from these reactions.

An inevitable consequence of the proposed interpretation is the appearance of anomalous superheavy sodium isotopes in the substance of the DAMA/NaI or DAMA/LIBRA detectors, the mass of which is approximately the mass of the *X* particle more than that of ordinary isotopes of these elements [60]. And the appearance of anomalous superheavy isotopes of iodine and thallium is unlikely, because it is disadvantageous for dark atoms to form low-energy bound states with these nuclei [60]. If the atoms of these anomalous sodium isotopes are not fully ionized, their mobility is determined by atomic cross-sections and becomes about nine orders of magnitude smaller than for *O*He (a special case of dark atoms when the charge of the particle *X* is -2) [60]. This ensures that they are stored in the detector. Therefore, mass spectroscopic analysis of this substance can provide additional verification for the possible presence of the *X*-helium nature of the DAMA result. Methods of such analysis should take into account the fragile nature of the bound states *X*He-Na, since their binding energy is only a few keV [60].

The ionization signal expected in detectors with a composition other than NaI can be in the energy range, mainly exceeding 2–6 keV [60]. It was shown in [60] that the rate of radiative capture σv of *O*He by a nucleus with atomic number A and charge number Z to the energy level E in the medium with temperature T, obtained by analogy with the neutron capture cross-section by a proton, is proportional to $\sigma v \propto \frac{Z^2 T}{A^{5/2}\sqrt{E}}$. Therefore, all other things being equal, at cryogenic temperatures and when *O*He interacts with heavy nuclei, the cross-section of such interaction will be suppressed. In addition, article [60] noted the high sensitivity of the results of numerical simulation of the interaction of *O*He with the nucleus to the values of uncertain nuclear parameters, taking into account that, for the selected range of nuclear parameters reproducing the results of DAMA/NaI and DAMA/LIBRA, it was shown that in *O*He-nucleus systems there are no bound levels for heavy nuclei, and therefore there is no ionization signal in detectors containing heavy nuclei (for example, xenon). The results of the interaction of *O*He with the iodine nucleus, presented below in this subsection and in Section 8 of this article, do not contradict the statements of article [60], since it follows that the energy levels of bound states of *O*He with the iodine nucleus are in the energy range significantly exceeding the energy of 2–6 keV modulo. At the same time, for certain parameters of the *O*He dark atom model, it is shown that the cross-section of the *O*He radiative capture by the Na nucleus into a bound state is orders of magnitude higher than the cross-section of the *O*He radiative capture into a bound state by the Iodine nucleus, which is consistent with the limitation for detecting high-energy gamma quanta in the DAMA experiment and naturally explains the selectivity of the signal from the material targets in underground experiments of direct search for dark matter particles.

Due to the unshielded nuclear charge of dark atom, there is a possibility of a strong nuclear interaction between *X*He atoms and the nuclei of matter, which can disrupt the bound state of dark atoms, potentially leading to the formation of anomalous isotopes, the distribution of which in the environment is strictly limited by experimental limits [101]. To solve this problem, the *X*He model assumes the presence of a shallow potential well and potential barrier within the effective interaction potential between the dark atom and

the nucleus (as shown in the Figure 8), which prevents the fusion of the components of the dark atom, i.e., the *n*–He nucleus and the *X* particle with nuclei of ordinary matter. This condition is crucial for the viability of the *X*-helium hypothesis.

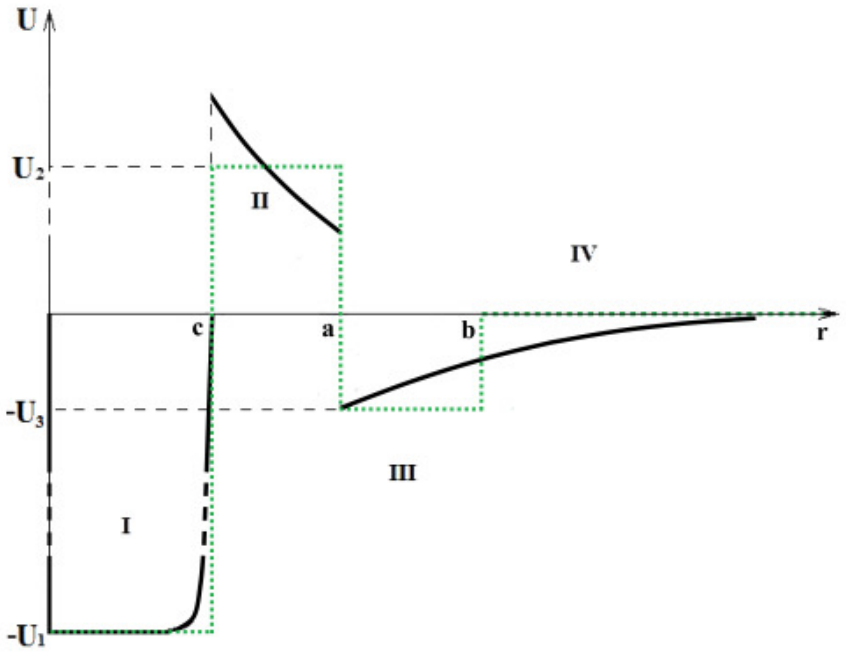

Figure 8. Hypothetical qualitative image of the shape of the effective interaction potential of *X*He dark atom with the nucleus of atom of matter [60].

This form of effective potential (see Figure 8) is mainly due to the competition between electromagnetic repulsion and the strong nuclear attraction of the nuclear shell of the dark atom and the nucleus of matter.

The total effective interaction potential of the *X*He–nucleus system can be interpreted as the total potential of the nucleus of matter when exposed to various forces from a dark atom, in the center of which is the origin of the coordinate system, when the nucleus of matter is slowly moving towards the dark atom, initially being at a large relative particle size distance from it.

Ultimately, the nucleus of matter moving at a slow thermal velocity (which is actually the relative velocity between the nucleus of matter and the dark atom in the detector), as a result of an inelastic capture reaction when interacting with a polarized dark atom, that is, dipole of *X*He, polarized due to the Stark effect in an external electric field created by the nucleus of matter itself, transitions to a low-energy bound state in a shallow potential well of the effective interaction potential of the *X*He-nucleus system. This leads to the release of energy in the form of an emitted photon, the energy of which is equal to the sum of the kinetic energy of the nucleus of matter and the binding energy in shallow well, which is observed as an ionization signal in the DAMA detector.

Modeling the interaction between dark atoms and the nuclei of ordinary matter is a three-body problem that does not have an exact analytical solution. Therefore, in order to understand the physical consequences of this scenario, determined by the effective interaction potential, an accurate quantum mechanical numerical model was developed for a three-body *X*He-nucleus system. The quantum mechanical numerical model of the interaction of the dark atom of *O*He with the nucleus of the substance, presented in article [102], models a system of three particles interacting through electrical, nuclear and centrifugal interactions. The methodology includes solving the Schrodinger equation for helium in the *O*He- nucleus system, at various fixed positions of the nucleus of

substance, $\vec{R}_{OA}$, relative to the dark atom. By taking into account the characteristics of both nuclear and electromagnetic interactions, this model makes it possible to accurately calculate the polarization of dark atom by calculating the dipole moment of a polarized *O*He atom for each fixed position of the nucleus of matter. In turn, dipole moments, depending on the distance between the nucleus and the dark atom, make it possible to restore the Stark potential, which describes the interaction of a polarized dark atom with the nucleus of matter, which plays a key role in forming the total effective interaction potential of the *O*He-nucleus system. This potential is equal to the sum of the following potentials: the Stark, centrifugal, nuclear, and electric interaction potential of an unpolarized dark atom with the nucleus $U^{e}_{\chi\mathrm{He}}$ (see Equation (23) in [102]), the last two potentials manifest themselves only at close distances between interacting particles, as they decrease exponentially with distance. Thus, in article [102], steps were taken towards a consistent quantum mechanical description of the interaction of dark atoms with unshielded nuclear attraction with the nucleus of an atom of matter.

Using the results of article [102], let us restore the total effective interaction potentials of the *O*He-Na and *O*He-I systems to find the energy levels and wave functions of the bound states of the *O*He dark atom with the nuclei of sodium and iodine in order to calculate the radiative capture cross-sections the nuclei of sodium and iodine into these bound states.

When solving the one-dimensional Schrodinger equation for the helium nucleus in the *O*He-nucleus system (see [102]) in order to calculate the wave functions of helium in the ground state of a polarized *O*He dark atom and to further use them to calculate the dipole moments of a polarized dark atom depending on the radius vector of the nucleus-substances, it is necessary to set the range of values of the radius vector of helium $\vec{r}$ with a fixed radius vector of the nucleus of the substance $\vec{R}_{OA}$. It is important for us to know the maximum negative value of the dipole moment, since the maximum depth of the Stark potential depends on it, which in turn determines the value of the energy level of the bound state of the nucleus of a substance with a dark atom in the potential well of the total effective interaction potential of the *O*He-nucleus system. $\vec{r}$ is a free parameter that determines the shape of the total helium interaction potential in the *O*He-nucleus system, U_{He}, in which for each given fixed radius vector of the nucleus of matter $\vec{R}_{OA}$ it is necessary solve the corresponding Schrodinger equation for helium. To solve this set of Schrodinger equations for each fixed position of the outer nucleus of matter slowly approaching the dark atom, it is also necessary to determine the interval for the radius vector of the nucleus $\vec{R}_{OA}$. This must be achieved taking into account the fact that before the interaction of the dark atom with the nucleus of matter begins, *O*He is already a bound quantum mechanical system. That is, the helium nucleus is initially bound to the particle O^{--} in a neutral *O*He atom, and when solving the Schrodinger equation for *He* in the *O*He-nucleus system, the initial condition for the helium wave function must be taken into account.

If we select the intervals of numerical values of the vectors $\vec{r}$ and $\vec{R}_{OA}$ such that they coincide or overlap with each other, then the solution of the stationary one-dimensional Schrodinger equation for helium in the *O*He-nucleus system in such $\vec{r}$ interval, with a fixed value of $\vec{R}_{OA}$, will always lead to a more likely occurrence of helium inside a deep potential well created by the nucleus of matter. However, the helium nucleus is initially located in the *O*He dark atom, which forms a bound quantum mechanical system before its interaction with the heavy nucleus begins. Therefore, it is necessary to take this condition into account and calculate the gradual increase in the polarization of the dark atom as the nucleus of matter approaches it, starting from some large distance. Therefore, the ranges of values of $\vec{r}$ and $\vec{R}_{OA}$ should be chosen so that for a certain value of $r^{*} = R^{*}_{OA} - R_{nuc} - R_{He}$, corresponding to a certain position of the nucleus of matter R^{*}_{OA}, where R_{nuc} and R_{He}

are the radii of the nuclei of matter and helium, respectively, which is the right boundary of the interval of the radius vector $\vec{r}$, a repolarization of the dark atom occurs when the dipole moment tends from the maximum negative value to the maximum positive value. In classical terms, this corresponds to the movement of helium from the position to the left of the particle O^{--} (maximum negative polarization OHe), when O^{--} is located between helium and the nucleus of matter, to the position to the right of O^{--} (maximum positive polarization OHe) due to the strong nuclear attraction of helium from the nucleus of matter. This ensures that helium, which is initially part of the dark atom, is gradually influenced by the approaching nucleus, as it approaches the dark atom, the probability of helium tunneling through the Coulomb barrier into the nucleus of matter increases and repolarization occurs.

We estimate the value of the radius vector of the nucleus of matter R^*_{OA} at which the dark atom is repolarized. That is, when the dipole moment of the polarized dark atom δ, caused by the Stark effect due to the alternating external electric field of the nucleus of matter, changes sign, tending from the maximum negative value to the maximum positive, it is possible to calculate the approximate dependence of the magnitude of the dipole moment δ on the distance between helium and the nucleus of matter.

The appearance of δ is the result of the action of the nuclear attractive force and the centrifugal and Coulomb repulsive forces from the nucleus of matter on helium in O-helium, while these forces are balanced by the Coulomb force of interaction between the particles of the dark atom, that is, between He, which is considered as a uniformly charged ball with a radius of R_{He}, and the particle O^{--} when the helium nucleus is displaced relative to the center of the dark atom by δ. Based on this, we can derive a semiclassical expression for evaluating δ:

$$\vec{\delta} = \left(\vec{F}_{\text{Coulomb}} + \vec{F}_{\text{Rot}} + \vec{F}_{Nuc} \right) \frac{R^3_{He}}{Z_{He} Z_{O^{--}} \alpha \hbar c}, \tag{36}$$

where $\vec{F}_{\text{Coulomb}}$, $\vec{F}_{\text{Rot}}$ and $\vec{F}_{Nuc}$ are the Coulomb, centrifugal and nuclear (Woods–Saxon type) forces of interaction between helium and the nucleus of matter, which are calculated through the action of the nabla operator on the corresponding potentials (see [102]), Z_{He} and $Z_{O^{--}}$ are the charge numbers of helium and the O^{--} particle, respectively, α is a fine structure constant (the expression used here is for the square of the elementary electric charge $e^2 = \alpha \hbar c$). The values of δ calculated using Formula (36) strongly depend on the radii of the nucleus of matter and helium, and on the diffuseness parameter of the nucleus of matter. For the values of the radius of the sodium nucleus, $R_{Na} = 1.15 \cdot A^{1/3}_{Na}$ fm, its diffuseness parameter $a_{Na} = 0.54$ fm, and the radius of helium $R_{He} = 1.02 \cdot A^{1/3}_{He}$ fm [103], estimating R^*_{OA} as $\vec{R}^*_{OA} = \vec{\delta} + \vec{R}_{HeA}$ for the maximum negative and positive values of δ, where R_{HeA} are the corresponding distances between the nuclei of helium and matter. This gives an approximate change of 8.5 fm $\lesssim R^*_{OA} \lesssim$ 18.5 fm. Since nuclear forces begin to act on approximately the same distance scale for different nuclei, the estimates for iodine are similar, although due to the larger radius, iodine begins to attract helium a little earlier, but also repels it more strongly due to the larger electric charge.

The shape of the total effective interaction potential of the OHe–nucleus system also depends on the spin of the O^{--} particle, since the centrifugal potential of the interaction of a dark atom with the nucleus depends on the magnitude of this spin [102]. At the same time, the value of the spin of the O^{--} particle is determined by the nature of the particle itself and is a model parameter [83].

In Section 8, using the derived formulas for the cross-sections of the radiative capture of the nuclei of substance by dark atom, the results of numerical analysis are presented,

showing at what values r^* (which is the boundary point of the interval of the radius vector of helium $\vec{r} = [-r^*, r^*]$ and is related to the position of the nucleus of matter, at which the dark atom is repolarized, as $R^*_{OA} = r^* + R_{nuc} + R_{He}$) and at what values of the O^{--} particle spin a low-energy bound state of dark atom with sodium nucleus is formed, the energy of which lies in the range from 2 keV to 6 keV and satisfies the limitations of the DAMA experiment for the count rate (see Equation (66)). It is also shown that the radiative capture cross-section of iodine nucleus into the bound state with *O*He is suppressed compared to that of sodium nucleus. The current section further shows examples of reconstructed total effective interaction potentials in the *O*He-Na and *O*He-I systems and the bound states of nuclei with a dark atom with certain energies and wave functions of these states corresponding to these effective interaction potentials.

Figures 9 and 10 show the restored total effective interaction potentials of the *O*He-Na and *O*He-I systems, respectively, at $\vec{r} = [-13, 13]$ fm for *O*He-Na and at $\vec{r} = [-11, 11]$ fm for *O*He-I. When restoring the potentials shown in Figures 9 and 10, the spin of the particle O^{--} was taken to be equal to $I_{O^{--}} = 1$. It can be seen from the figures that the shape of the total effective interaction potential of a dark atom with a nucleus is consistent with the expected theoretical shape of this potential. The total effective interaction potentials have potential wells with a depth of approximately 136 keV for the *O*He-Na system and 1620 keV for the *O*He-I system, and positive potential barriers in front of these wells with a height of more than 10 keV exceeding the thermal kinetic energy of the nucleus of matter at room temperature, which is estimated at about $4 \cdot 10^{-2}$ eV. The presence of this positive potential barrier makes it possible to preserve the integrity and stability of the dark atom, playing a key role in preventing direct fusion of helium or the O^{--} particle with the nucleus of matter.

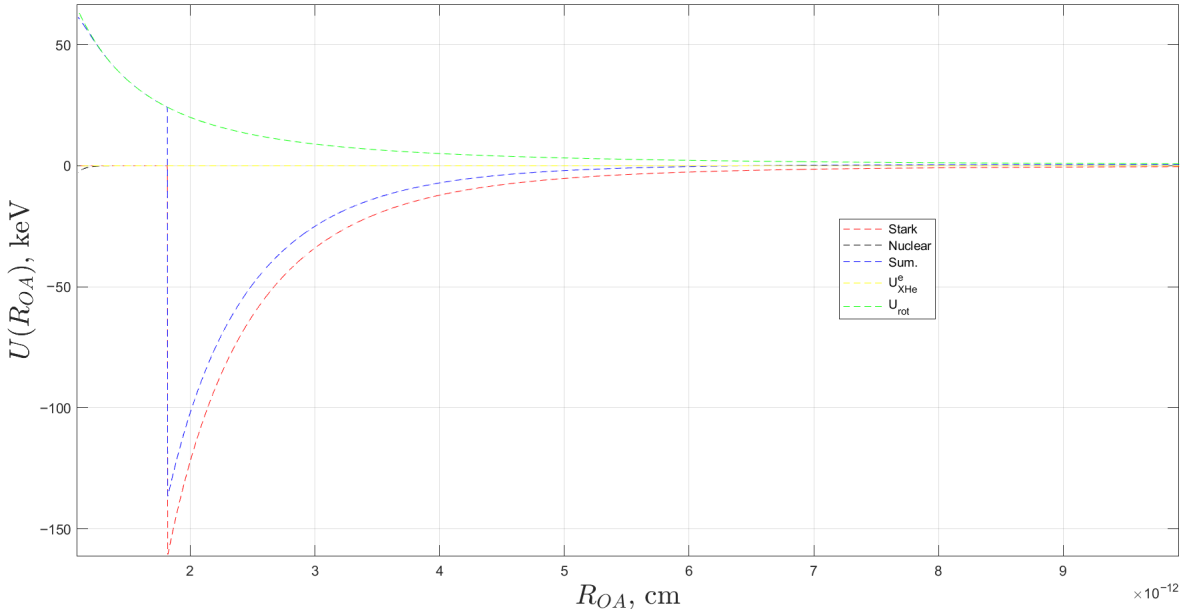

Figure 9. Various interaction potentials within the *O*He–Na system, presented as functions of the distance between the OHe dark atom and nucleus of Na, R_{OA}: the Stark interaction potential (red dotted line), the centrifugal interaction potential (green dotted line), nuclear potential (black dotted line), the electric interaction potential U^e_{XHe} of unpolarized dark atom with the nucleus (yellow dotted line) and the total effective interaction potential (blue dotted line). The case corresponds to the total angular momentum for the interaction between OHe and the sodium nucleus, equal to $\vec{J}_{\mathrm{OHe-Na}} = 5/2$. The results of paper [102] were used in the calculations.

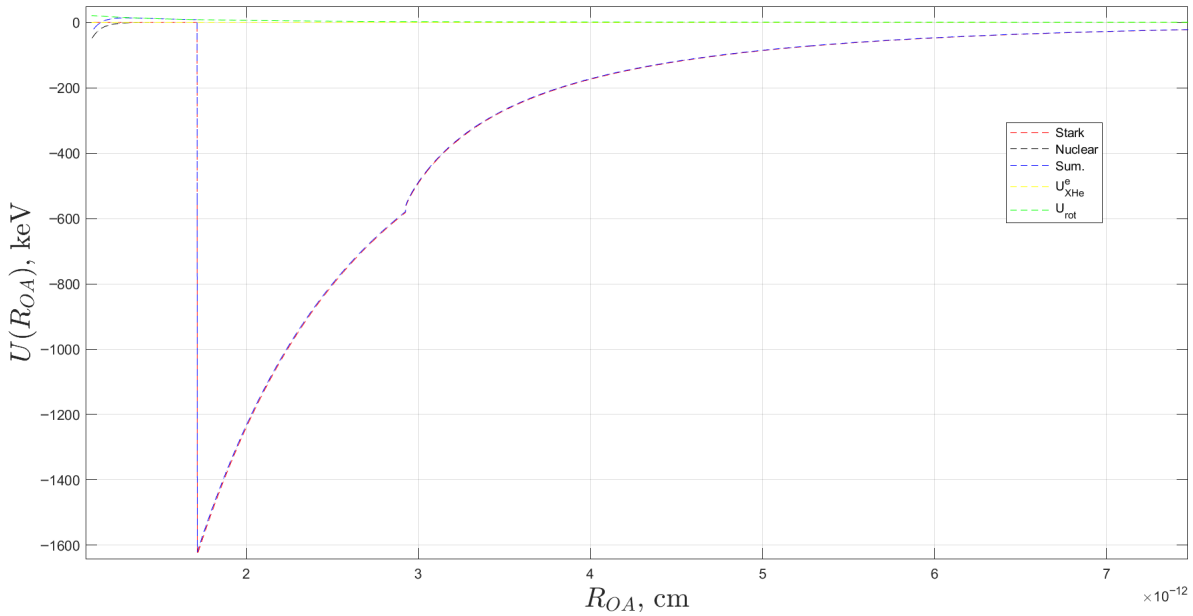

Figure 10. Various interaction potentials within the *O*He–I system, presented as functions of the distance between the *O*He dark atom and nucleus of Iodine, R_{OA}: the Stark interaction potential (red dotted line), the centrifugal interaction potential (green dotted line), nuclear potential (black dotted line), the electric interaction potential $U^{\mathrm{e}}_{\mathrm{XHe}}$ of unpolarized dark atom with the nucleus (yellow dotted line) and the total effective interaction potential (blue dotted line). The case corresponds to the total angular momentum for the interaction between *O*He and the iodine nucleus, equal to $\vec{J}_{\mathrm{OHe-I}} = 7/2$. The results of paper [102] were used in the calculations.

By solving the one-dimensional stationary Schrodinger equation for the free nuclei of sodium and iodine in the total effective interaction potentials of the systems *O*He-Na and *O*He-I, shown by blue dotted lines in Figures 9 and 10, respectively, we can obtain a discrete spectrum of the energies of the bound states of sodium and iodine in the potential well of the total effective potential, as well as the normalized wave functions of sodium and iodine in these bound states corresponding to these energies.

The result of this solution for the sodium nucleus is shown in Figure 11. It can be seen from the figure that in the potential well of the total effective interaction potential of the *O*He-Na system, there is only one bound state, which is the ground bound state in this potential with energy $E_{1_{Na}} \approx -2.4$ keV. In Figure 11, the blue solid line shows the total effective interaction potential of the *O*He dark atom with the sodium nucleus, and the red solid line shows the graph of the square of the modulus of the sodium wave function corresponding to the energy level of the ground and only bound state of sodium in this total effective interaction potential of the *O*He-Na system.

The result of solving the Schrodinger equation for the iodine nucleus in the effective interaction potential of the *O*He-I system is shown in Figure 12. It can be seen from the figure that there are several bound states in the potential well of the total effective interaction potential of the *O*He-I system. The figure shows the first five energy levels of the bound states (ground and four excited): $E_{1_I} \approx -1.07$ MeV, $E_{2_I} \approx -762$ keV, $E_{3_I} \approx -556$ keV, $E_{4_I} \approx -367$ keV and $E_{5_I} \approx -231$ keV. Thus, in Figure 12, the blue solid line shows the total effective interaction potential of the *O*He dark atom with the iodine nucleus, and the red solid lines show graphs of the square of the modulus of the wave functions of the first five bound states of iodine in this total effective interaction potential of the *O*He-I system.

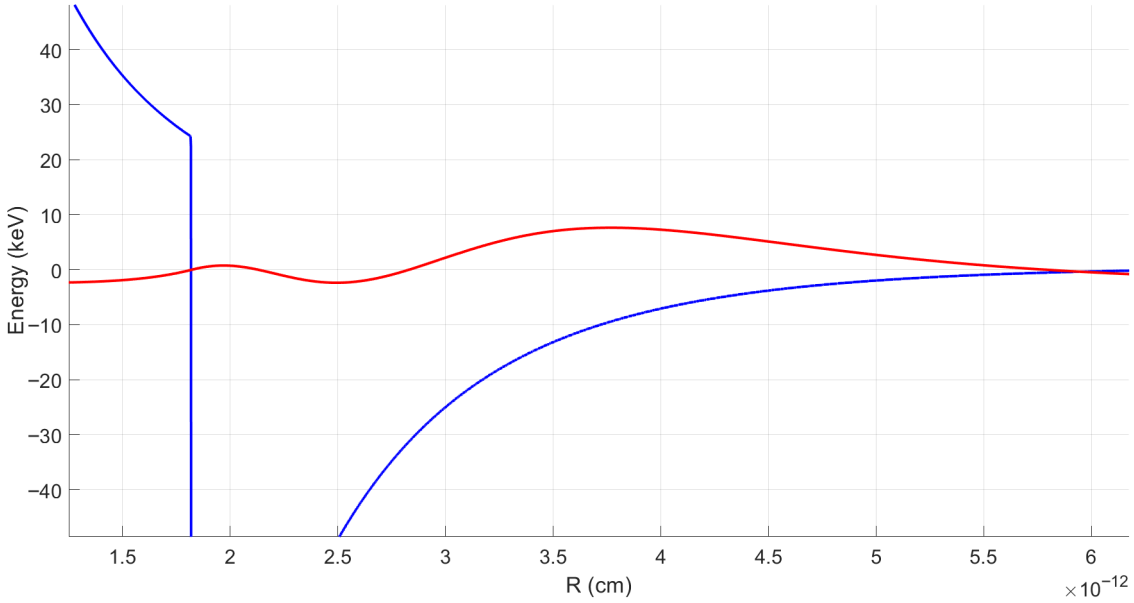

Figure 11. Graphs of the dependence of the total effective interaction potential of the *O*He dark atom with the sodium nucleus (blue solid line) and the square of the modulus of the sodium wave function (red solid line), corresponding to the energy level of the ground state of sodium in this total effective interaction potential of the *O*He-Na system, equal to $E_{1_{Na}} \approx -2.4$ keV, from the radius vector of sodium nucleus.

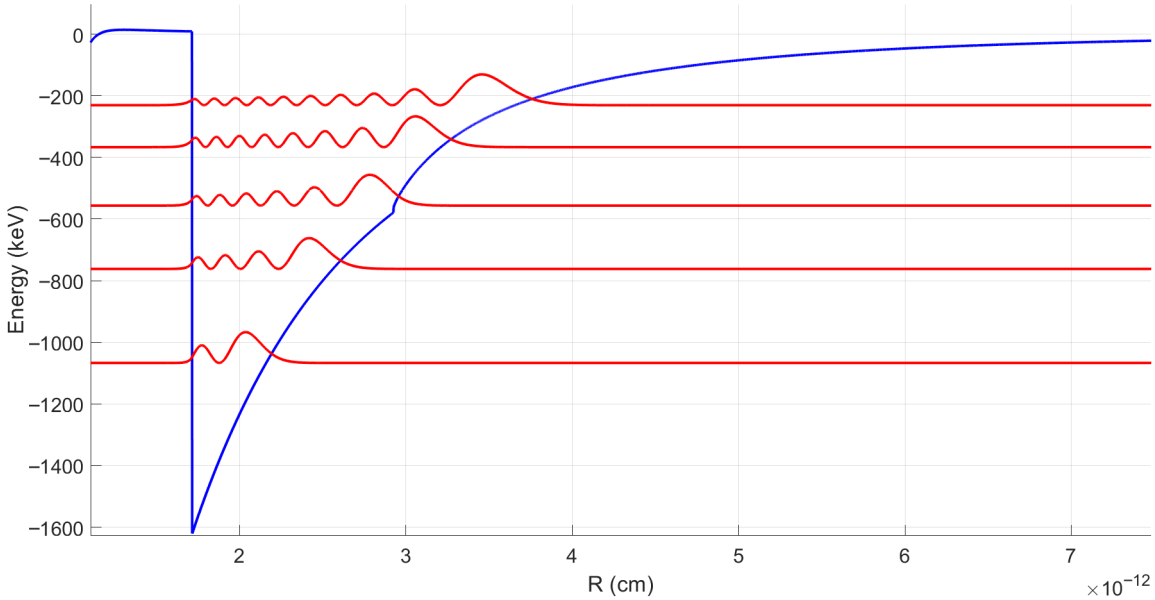

Figure 12. Graphs of the dependence of the total effective interaction potential of the *O*He dark atom with the iodine nucleus (blue solid line) and the square of the modulus of the wave functions of the first five bound states of iodine (red solid lines) corresponding to energy levels: $E_{1_I} \approx -1.07$ MeV, $E_{2_I} \approx -762$ keV, $E_{3_I} \approx -556$ keV, $E_{4_I} \approx -367$ keV and $E_{5_I} \approx -231$ keV in this total effective interaction potential of the *O*He-I system, from the radius of the iodine nucleus vector.

6.2. Calculation of the Radiative Capture Cross-Section in the OHe-Nucleus System

Let us use the obtained material, normalized by one wave function of sodium in the ground bound state of the *O*He-Na system, $\Psi^{(1)}_{f_{Na}}$, which we consider as the final state of sodium, along with the normalized by one wave functions of iodine in the ground bound state, $\Psi^{(1)}_{f_I}$, and the first excited state, $\Psi^{(2)}_{f_I}$, to calculate the capture cross-sections of sodium and iodine nuclei into these bound states.

In the initial state, the nucleus of matter represents a free particle described by the wave function $\Psi_{i_{nuc}}(r)$ (for sodium $\Psi_{i_{Na}}(r)$ and for iodine $\Psi_{i_I}(r)$), which is a solution to the Schrödinger equation for the nucleus of substance with relative thermal motion in the effective interaction potential $V_{eff}(r)$ of the *O*He-nucleus system:

$$\left[-\frac{\hbar^2}{2\mu}\nabla^2 + V_{eff}(r) - E\right]\Psi_{i_{nuc}}(r) = 0, \tag{37}$$

where μ is the reduced mass of the system *O*He-nucleus, $E = \frac{3}{2}k_bT$ is the energy of relative thermal motion in the center of mass system.

Since the potential $V_{eff}(r)$ is spherically symmetric, the wave function $\Psi_{i_{nuc}}(r)$ modified by this potential influence can be decomposed into partial waves (spherical harmonics) [104]:

$$\Psi_{i_{nuc}}(r) = \sum_{l=0}^{\infty}\sum_{m=-l}^{l}\frac{u_l(r)}{r}Y_{lm}(\theta,\varphi), \tag{38}$$

where $u_l(r)$ is the radial wave function and $Y_{lm}(\theta,\varphi)$ is spherical function.

Substituting (38) into Equation (37) and using the properties of orthogonality of spherical harmonics, we obtain the radial Schrodinger equation for each partial wave:

$$\left[-\frac{\hbar^2}{2\mu}\frac{d^2}{dr^2} + V_{eff}(r) + \frac{\hbar^2 l(l+1)}{2\mu r^2} - E\right]u_l(r) = 0, \tag{39}$$

where $\frac{\hbar^2 l(l+1)}{2\mu r^2}$ is a centrifugal potential that occurs naturally when variables are separated in spherical coordinates.

Thus, in the entire region of space where the effective interaction potential is not zero, the wave function of the initial state can be written as:

$$\Psi_{i_{nuc}}(r) = \sum_{l=0}^{\infty}(2l+1)i^l R_l^{\text{norm}}(r)P_l(\cos\theta), \tag{40}$$

where $R_l^{\text{norm}}(r) = N_l \cdot u_l(r)/r = N_l \cdot R_l(r)$ is the normalized radial component of the wave function, N_l is the normalization factor, $R_l(r) = u_l(r)/r$ is an unnormalized radial wave function, and $P_l(\cos\theta)$ is the Legendre polynomials.

The radial wave function $R_l^{\text{norm}}(r)$ is normalized in such a way that the condition is satisfied in the asymptotic domain ($r \to \infty$) [104]:

$$R_l^{\text{norm}}(r) = e^{i\delta_l}[\cos\delta_l\, j_l(k_{nuc}r) - \sin\delta_l\, n_l(k_{nuc}r)], \tag{41}$$

where $k_{nuc} = \frac{p_{nuc}}{\hbar} = \frac{m_{nuc}v}{\hbar}$ is the wave vector of the nucleus of substance, p_{nuc} and m_{nuc} are the momentum and mass of the nucleus of substance, respectively, and v is the relative velocity of interacting particles in the *O*He-nucleus system. $j_l(k_{nuc}r)$ are spherical Bessel functions, $n_l(k_{nuc}r)$ are spherical Neumann functions, and δ_l are the scattering phases, determined by the potential $V_{eff}(r)$ and containing all the information about scattering behavior for each partial wave with orbital angular momentum l.

For the numerical solution of Equation (39), the Numerov method is used, which ensures high accuracy of integration of second-order equations. Equation (39) is written as:

$$\frac{d^2u_l}{dr^2} = \frac{2\mu}{\hbar^2}\left[V_{eff}(r) + \frac{\hbar^2 l(l+1)}{2\mu r^2} - E\right]u_l(r) = F(r)u_l(r). \tag{42}$$

The Numerov method is implemented using the recurrent formula:

$$u_{l,i+1} = \frac{2u_{l,i} - u_{l,i-1} + \frac{\Delta r^2}{12}(F_{i-1}u_{l,i-1} + 10F_i u_{l,i})}{1 - \frac{\Delta r^2}{12}F_{i+1}}, \tag{43}$$

where Δr is the grid step, $u_{l,i} = u_l(r_i)$, $F_i = F(r_i)$.

The initial conditions for $l = 0$ and $l = 1$ are chosen as follows:

1. For $l = 0$: $u_0(r_{\min}) \approx r_{\min}$, $u_0(r_{\min} + \Delta r) \approx r_{\min} + \Delta r$.
2. For $l = 1$: $u_1(r_{\min}) \approx r_{\min}^2$, $u_1(r_{\min} + \Delta r) \approx (r_{\min} + \Delta r)^2$.

The phase shifts of δ_l are calculated by solving the radial Schrodinger Equation (39) and obtaining a numerical solution of $R_l(r)$ followed by comparing the numerical solution with the asymptotic form (41). Specifically, the phase shift is determined by calculating the logarithmic derivative L of the radial wave function at the point r_0, where the potential $V_{eff}(r)$ becomes negligible:

$$\tan\delta_l = \frac{k_{nuc} j_l'(k_{nuc}r_0) - j_l(k_{nuc}r_0) \cdot L}{k_{nuc} n_l'(k_{nuc}r_0) - n_l(k_{nuc}r_0) \cdot L}, \tag{44}$$

where $L = R_l'(r_0)/R_l(r_0)$ is the logarithmic derivative, j_l' and n_l' are the derivatives of spherical Bessel and Neumann functions.

Thus, normalization is performed by comparing the numerical solution of $R_l(r)$ in the asymptotic domain with the analytical expression (41) at the point r_0, where the potential of $V_{eff}(r)$ becomes negligible. Then the normalization factor is N_l:

$$N_l = \frac{e^{i\delta_l} \cdot [\cos\delta_l \, j_l(k_{nuc}r_0) - \sin\delta_l \, n_l(k_{nuc}r_0)]}{R_l(r_0)}. \tag{45}$$

For the sodium nucleus, there is a single energy level in the range of 1–6 keV in the total effective interaction potential, which allows only an E1 transition from the initial state of sodium with $l_i = 1$ to the final bound state with $l_f = 0$. At thermal energies, the orbital moment of the free nucleus is practically zero, the wave function of the initial state is mainly an s-wave, but there is also a small admixture of a p-wave in the initial state of the free nucleus. Therefore, we decompose the wave function of the free nucleus into partial waves, that is, into radial wave functions that depend on the orbital moment and are the solution of the Schrodinger equation in the effective interaction potential for the energy of relative thermal motion $E = \frac{3}{2}k_bT$ in the center of mass *O*He-Na system. After that, we take the second term of the decomposition of the wave function of the free sodium nucleus into partial waves, that is, a p-wave with $l_i = 1$. Thus, there is a possibility that the sodium nucleus will transition from the initial state of the p-wave to the final bound state. This transition is suppressed due to the fact that the p-wave is only a small addition to the s-wave of the free nucleus at thermal energies.

On the other hand, for the iodine nucleus, there are several deeply bound states in the effective interaction potential with the dark atom (including the ground state with an energy of -1.07 MeV and the first excited state with an energy of -762 keV), which allow for two distinct most probable E1 transitions:

1. From the initial state of iodine with $l_i = 1$ to the ground bound state with $l_f = 0$ (energy -1.07 MeV).
2. From the initial state of iodine with $l_i = 0$ to the first excited bound state with $l_f = 1$ (energy -762 keV).

According to Fermi's Golden Rule, the probability of transition per unit of time from the initial state $|i\rangle$ to the set of final states $|f\rangle$ is determined by the following expression:

$$\Gamma_{i\to f} = \frac{2\pi}{\hbar}\left|\langle f|\hat{H}_{\text{int}}|i\rangle\right|^2 g(E_f), \tag{46}$$

where $\langle f|\hat{H}_{\text{int}}|i\rangle$ is the matrix element of the interaction operator, $\hat{H}_{\text{int}}$, for the electrical transition between the final and initial states, and $g(E_f)$ is the density of final states at energy E_f.

Fermi's Golden Rule relates the probability of a transition to the density of the final states. In the process of nucleus capture by a dark atom with photon emission, the density of the final states is determined by the emitted photon. In the process we consider, the nucleus of matter passes from a free state to a bound state with dark atom, while a photon with energy is emitted:

$$E_\gamma = T_{\text{nuc}} + I_{\text{OHe}-\text{nuc}} \approx I_{\text{OHe}-\text{nuc}}, \tag{47}$$

where $T_{\text{nuc}} = \dfrac{p_{nuc}^2}{2m_{nuc}} \approx 4\cdot 10^{-2}$ eV is the kinetic thermal energy of the nucleus in the free state and $I_{\text{OHe}-\text{nuc}}$ is the energy of the bound state of the nucleus of matter with the *O*He dark atom.

Since the system initially consists of free nucleus and *O*He dark atom, while the final state comprises the bound *O*He-nucleus system and a photon, the final states are determined by the photon parameters. This is because the initial state of the nucleus exists in the continuum (as a free particle), whereas the final state is a discrete bound state. However, the transition is physically possible only through photon emission, whose parameters form a continuum of states. Thus, the total density of final states is governed precisely by the photon, since the *O*He-nucleus bound state is fixed (discrete), whereas the photon can occupy various momentum and directional states.

The bound *O*He-nucleus system possesses discrete energy after nucleus capture, thus its contribution to $g(E_f)$ corresponds to a single state (Dirac delta function). In contrast, the emitted photon, with energy virtually identical to the binding energy of the nucleus with the *O*He dark atom, $I_{\text{OHe}-\text{nuc}}$, can be emitted in any direction with fixed energy (when neglecting the recoil of the *O*He-nucleus system). This determines the angular dependence of the final state density. Consequently, the number of final states per unit energy interval per unit volume for photon emission into solid angle $d\Omega$, accounting for the two possible spin projections of the photon due to the transverse nature of electromagnetic waves, is given by the following expression in three-dimensional space:

$$g(E_\gamma) = 2\frac{d}{dE_\gamma}\left(\int \frac{d^3\vec{q}_\gamma}{(2\pi)^3}\right) = \frac{E_\gamma^2}{4\pi^3 c^3\hbar^3}d\Omega, \tag{48}$$

where $|\vec{q}_\gamma| = \dfrac{E_\gamma}{c\hbar}$ is the wave vector of the photon.

The cross-section of the radiative capture of the nucleus of matter into the *O*He-nucleus bound state is expressed by the following formula:

$$\sigma_{\text{OHe}-\text{nuc}} = \frac{\Gamma_{i\to f}}{j}, \tag{49}$$

where j is the falling flux of nuclei of matter.

For the radiative capture process, the initial state is described by the scattering wave function, which must be normalized to a single flux so that the flux density in the incident wave is:

$$j = \frac{\hbar k_{NA}}{\mu} = v, \tag{50}$$

where v is the relative velocity of the interacting particles. It is equal to the thermal velocity of the nucleus of substance towards the dark atom in the center of mass system since in the process under consideration, due to the large mass of the dark atom compared to the mass of nucleus, the center of mass system coincides with the laboratory system in which the dark atom rests.

Substituting $\Gamma_{i\to f}$ into the formula for the cross-sections, we get:

$$\sigma_{\mathrm{OHe-nuc}} = \frac{2\pi}{\hbar}\frac{1}{v}\left|\langle f|\hat{H}_{\mathrm{int}}|i\rangle\right|^2 g(E_\gamma) = \frac{2\pi}{\hbar}\frac{1}{v}\left|\langle f|\hat{H}_{\mathrm{int}}|i\rangle\right|^2 \frac{E_\gamma^2}{4\pi^3 c^3 \hbar^3} d\Omega. \tag{51}$$

The transition of the nucleus of substance to a bound state with dark atom occurs when the nucleus interacts with electromagnetic radiation. The Hamilton operator, which defines the electric multipole transition of the order J of the nucleus to a bound state, $\hat{H}_{\mathrm{int}}$, in the dipole approximation, is determined by decomposing the vector potential of the electromagnetic field into functions with a certain moment and parity. And for the long-wavelength approximation, which is typical for the process of radiation capture of the nucleus of matter into a low-energy bound state with dark atom with photon emission that we consider, since $(q_\gamma \cdot r) \approx 10^{-4} << 1$, the electric multipole transition operator of the order J is given by the expression [105]:

$$\hat{H}_{\mathrm{int}} = -A_0 \sqrt{\frac{2\pi(J+1)}{J[(2J+1)!!]^2}} q_\gamma^J \hat{Q}_{Jm}, \tag{52}$$

where $\hat{Q}_{Jm} = eZ_{nuc} r^J Y_{Jm}(\theta, \phi)$ is the operator of the static electric multipole moment, Z_{nuc} is the charge number of the nucleus of a substance ($Z_{Na} = 11$ for sodium and $Z_I = 53$ for iodine), and $A_0 = \sqrt{\frac{2\pi c\hbar}{q_\gamma}}$ is the amplitude of the vector potential of the electromagnetic wave, which is usually selected such that it corresponds to the presence of one quantum per unit volume.

We take into account the use of Expression (40) and considering the wave function of the initial state as a partial wave with an orbital moment l_i. Therefore, the matrix element of the transition operator between the final and initial states, $\langle f|\hat{H}_{\mathrm{int}}|i\rangle$, is given by the following expression, where the matrix element splits into radial and angular parts:

$$\langle f|\hat{H}_{\mathrm{int}}|i\rangle = -A_0 \sqrt{\frac{2\pi(J+1)}{J[(2J+1)!!]^2}} q_\gamma^J eZ_{nuc} \langle l_f|Y_{Jm}(\theta,\phi)|l_i\rangle \cdot I_{\mathrm{radial}}, \tag{53}$$

where $I_{\mathrm{radial}} = \int_0^\infty \Psi^{*(n)}_{f_{nuc}}(r) \cdot r^{J+2} \cdot (2l_i+1) i^{l_i} \cdot R^{\mathrm{norm}}_{l_i}(r) dr$ is the radial part of the matrix element and $\langle l_f|Y_{Jm}(\theta,\phi)|l_i\rangle$ is the angular part of the matrix element.

The angular part of the matrix element for the transition $l_i = J \to l_f = 0$ is defined as follows:

$$\langle 0|Y_{Jm}(\theta,\phi)|J\rangle = \int Y_{00}(\theta,\phi) \cdot Y_{Jm}(\theta,\phi) \cdot P_J(cos(\theta)) d\Omega = \frac{1}{\sqrt{(2J+1)}}. \tag{54}$$

On the other hand, the angular part of the matrix element for the transition $l_i = 0 \to l_f = J$ is equal to:

$$\langle J|Y_{Jm}(\theta,\phi)|0\rangle = \int Y_{J0}(\theta,\phi)\cdot Y_{Jm}(\theta,\phi)\cdot P_0(cos(\theta))d\Omega = 1. \quad (55)$$

Then, the square of the modulus of the matrix element of the static electric multipole moment operator $\hat{Q}_{Jm}$ for transitions $l_i = J \to l_f = 0$ and $l_i = 0 \to l_f = J$ is equal, respectively:

$$|\langle 0||\hat{Q}_{Jm}||J\rangle|^2 = \frac{e^2 Z_{nuc}^2}{(2J+1)}\left|\int_0^\infty \Psi_{f_{nuc}}^{*(1)}(r)\cdot r^{J+2}\cdot(2J+1)i^J\cdot R_J^{\rm norm}(r)dr\right|^2, \quad (56)$$

$$|\langle J||\hat{Q}_{Jm}||0\rangle|^2 = e^2 Z_{nuc}^2\left|\int_0^\infty \Psi_{f_{nuc}}^{*(2)}(r)\cdot r^{J+2}\cdot R_0^{\rm norm}(r)dr\right|^2. \quad (57)$$

Substituting expressions of the perturbation matrix element $\langle f|\hat{H}_{\rm int}|i\rangle$ for transitions to the ground bound state *O*He-nucleus $l_i = J \to l_f = 0$ and to the excited bound state *O*He-nucleus $l_i = 0 \to l_f = J$ in Formula (51) for the cross-section of the radiative capture of the nucleus, taking into account the fact that $e^2 = \alpha\hbar c$, where α is a fine structure constant, we obtain:

$$\sigma_{\rm OHe-nuc}^{J\to 0} = \frac{8\pi q_\gamma^{2J+1}\alpha c Z_{nuc}^2}{v}\frac{(J+1)(2J+1)}{J[(2J+1)!!]^2}\left|\int_0^\infty \Psi_{f_{nuc}}^{*(1)}(r)\cdot r^{J+2}\cdot i^J\cdot R_J^{\rm norm}(r)dr\right|^2, \quad (58)$$

$$\sigma_{\rm OHe-nuc}^{0\to J} = \frac{8\pi q_\gamma^{2J+1}\alpha c Z_{nuc}^2}{v}\frac{(J+1)}{J[(2J+1)!!]^2}\left|\int_0^\infty \Psi_{f_{nuc}}^{*(2)}(r)\cdot r^{J+2}\cdot R_0^{\rm norm}(r)dr\right|^2. \quad (59)$$

Eventually, the final expressions for the rates of radiative capture of the nucleus of matter from the initial state of a free particle with an orbital moment of $l_i = 1$ to the final ground bound state in the potential well of the total effective interaction potential of the *O*He-nucleus system with an orbital moment of $l_f = 0$ and from the initial state with an orbital moment of $l_i = 0$ to a finite excited bound state with an orbital moment of $l_f = 1$ are given by the following expressions:

$$(\sigma_{\rm OHe-nuc}^{1\to 0}\cdot v) = \frac{16\pi}{3}\alpha c\frac{E_\gamma^3}{c^3\hbar^3}Z_{\rm nuc}^2\left|\int_0^\infty \Psi_{f_{nuc}}^{*(1)}(r)\cdot r^3\cdot i\cdot R_1^{\rm norm}(r)dr\right|^2, \quad (60)$$

$$(\sigma_{\rm OHe-nuc}^{0\to 1}\cdot v) = \frac{16\pi}{9}\alpha c\frac{E_\gamma^3}{c^3\hbar^3}Z_{\rm nuc}^2\left|\int_0^\infty \Psi_{f_{nuc}}^{*(2)}(r)\cdot r^3\cdot R_0^{\rm norm}(r)dr\right|^2. \quad (61)$$

7. Dark Atoms and Experimental DAMA Results as Benchmark for Procedure Developing

Over the years, the use of NaI(Tl) detectors in DAMA has undergone two main phases: DAMA/NaI (seven annual cycles) and DAMA/LIBRA (2003–2024). After the first stage, dubbed DAMA/LIBRA–phase1, with a 2 keV energy threshold, in 2010 DAMA/LIBRA underwent a major upgrade, replacing the PMTs with high-quantum-efficiency Hamamatsu R6233MOD tubes, reducing the software energy threshold to 1 keV. This second phase is known as DAMA/LIBRA–phase2 [9]. In late 2021, a further upgrade of DAMA/LIBRA–phase2 configuration, termed phase2-empowered, began with the specific aim of lowering the software energy threshold below 1 keV while sustaining high acceptance efficiency. All PMTs were provided with miniaturized low-background preamplifiers and new high-voltage dividers; the front-end electronics chain was enhanced by employing 14-bit digitizers with improved vertical resolution. These changes improve

energy resolution, reduce electronic noise, and enhance discrimination of *single-hit* scintillation events (i.e., those events in which just one detector of many actually "fires") near the software energy threshold.

The DAMA/NaI and DAMA/LIBRA experiments have reported over two decades of evidence for a model-independent annual modulation signal that respects all the requirements of presence of dark matter particles in the galactic halo. The residual counting rates of the two phases of DAMA/LIBRA are reported in Figure 13.

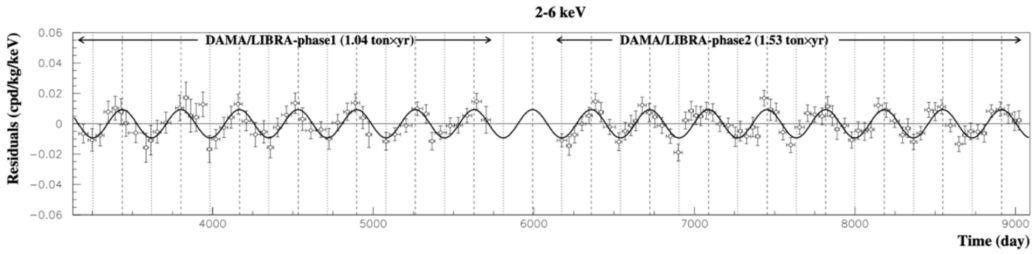

Figure 13. Experimental residual rate of the *single-hit* scintillation events measured by DAMA/LIBRA–phase1 and DAMA/LIBRA–phase2 in the (2–6) keV energy intervals as a function of the time. The superimposed curve is the co-sinusoidal functional form $A\cos\omega(t - t_0)$ with a period $T = 2\pi/\omega = 1$ year, a phase $t_0 = 152.5$ day (2 June), and a modulation amplitude, A, equal to the central value of the best fit. The dashed vertical lines correspond to the maximum expected for the DM signal (2 June), while the dotted vertical lines correspond to the expected minimum. For details, see Ref. [9].

Within the framework of the dark atom model, the presence of such an annual modulation is also expected; therefore, to validate the model on the one hand, and to assess the similarity with the experiment on the other hand, a simulation was carried out using the stochastic Monte Carlo method. For 11 years, corresponding to the second phase of the DAMA/LIBRA experiment, numerical modeling was performed using the procedure described in Section 5. The results are presented in Figure 14.

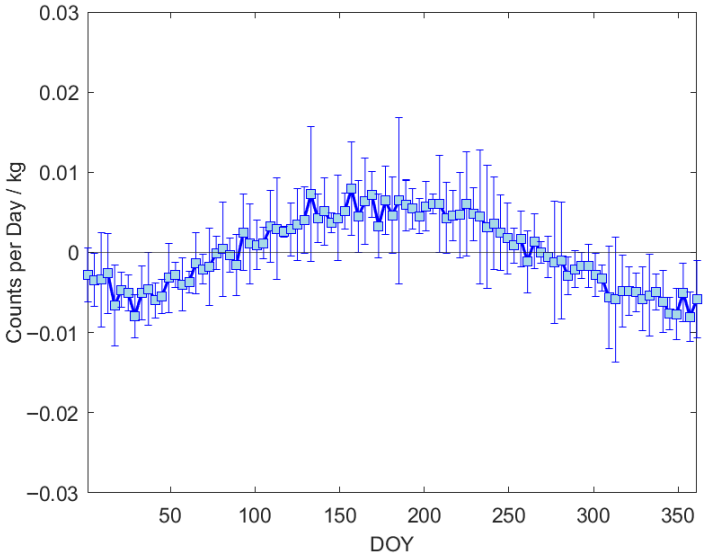

Figure 14. Results of Monte Carlo simulation for the annual modulation of the residual count rate as a function of the day of the year (DOY), averaged over 11 years for the period from 2011 to 2022. Error bars represent the variance.

Importantly, DAMA has extensively checked for possible systematic effects or background sources that could mimic the annual modulation. No such effects, correlated with temperature, radon levels, cosmic muons, or other environmental variables, have been

able to explain the observed modulation within the required phase and energy range [8]. It should be noted that the hardware configuration, the specific hardware and software procedures employed, and overall design features of DAMA significantly differ from those of COSINE-100 and ANAIS-112. Given these differences and the arguments reported in Section 1, the DAMA results, covering both the annual and diurnal modulation signatures, as well as additional analyses, are used in this paper for studies of the dark atom model across its possible detection strategies.

While the DAMA collaboration reports a highly significant annual modulation effect, the search for a diurnal modulation remains consistent with null results within the present sensitivity [11]; see also later. In the following, both annual and diurnal results are quantified in terms of dark atoms.

7.1. Annual Modulation

The DAMA/NaI and DAMA/LIBRA experiments have reported consistent evidence for an annual modulation signal satisfying all the requirements of the model-independent dark matter signature [8,9,100].

The expected counting rate for dark matter interactions in a detector should have a cosine-like modulation:

$$S(t) = S_0 + S_m \cos \omega(t - t_0), \tag{62}$$

where S_0 is the constant component, S_m is the modulation amplitude, $\omega = 2\pi/T$ with $T = 1$ year, and $t_0 \simeq 2$ June is the expected phase.

Let us consider the process in which a DM particle constituted by dark atom (O) is captured either by Na or Iodine nucleus in a NaI(Tl) detector:

$$\begin{aligned} O + {}^{23}\mathrm{Na} &\rightarrow {}^{23}\mathrm{Na} + \gamma\text{'s} \\ O + {}^{127}\mathrm{I} &\rightarrow {}^{127}\mathrm{I} + \gamma\text{'s} \end{aligned} \tag{63}$$

The O particles become thermalized as they traverse the layers of rock above an underground experiment, such as DAMA/LIBRA. As a result, their velocity is approximately equal to the thermal velocity of the rock. If the γ-rays produced in the reactions of Equation (63) have energies around ∼1–6 keV, these dark matter particles could account for the groundbreaking annual modulation result observed in DAMA/NaI and DAMA/LIBRA.

The capture rate of Equation (63) can be written as:

$$S = \epsilon \frac{\rho_O}{M_O} (\langle v_1 \sigma_1 \rangle + \langle v_2 \sigma_2 \rangle) N_T \tag{64}$$

where ρ_O is the density of O particles, with mass M_O, in proximity of the detectors, v_i is the relative velocity between O particle and ith nucleus ($i = 1, 2$ for Na and Iodine, respectively), and σ_i is the capture cross section of the process of Equation (63). As mentioned above, v_i are of the order of thermal velocities. However, since M_O is much higher than the nuclei masses, v_i are mainly the thermal velocities of the Na and Iodine nuclei. The number of target N_T is the same for Na and Iodine nuclei: $N_T = 4.015 \times 10^{24}$ nuclei per kg of NaI(Tl); finally, ϵ is the efficiency to detect the γ-rays produced in the reactions of Equation (63). Due to the large mass of the DAMA/LIBRA detectors (approximately 9.7 kg each), we can assume that low-energy γ-rays are fully absorbed within the detector. Therefore, the only factor that could play a role is the energy threshold, which is 1 keV for DAMA/LIBRA–phase2. For instance, if the γ-ray energy is 3 keV, considering the energy resolution of the detectors, we lose 1.7% of events due to the 1 keV threshold. However, for the purposes of this paper, we assume that $\epsilon = 1$.

As already discussed, the velocity of the O particles striking the top of the mountain varies throughout the year because of Earth's revolution around the Sun. This variation leads to a different accumulation of O particles near the NaI(Tl) detectors in the underground laboratory. We can parameterize this effect as follows:

$$\rho_O(t) = \rho_O^0 + \Delta\rho_O \cos\omega(t - t_0) \tag{65}$$

where ρ_O^0 is the time-independent density, $\Delta\rho_O$ is its modulation amplitude, $\omega = \frac{2\pi}{T}$ with $T = 1$ year and t_0 is the phase of the annual modulation approximately equal to 2 June. This justifies Equation (62).

The experimental modulation amplitudes, S_m, can be extracted by the data of DAMA/NaI and DAMA/LIBRA; they are summarized in Figure 15. A clear modulation is present in the lowest energy region, while S_m values compatible with zero are present just above. See ref. [9]. Specifically, considering the energy range between 1 keV and 6 keV, one obtains:

$$S_m = (6.95 \pm 0.45) \times 10^{-2} \text{ counts}/(\text{day} \cdot \text{kg})$$
$$S_0 < 0.5 \text{ counts}/(\text{day} \cdot \text{kg}) \tag{66}$$

where the first value is obtained by integrating the modulation amplitudes of Figure 15 over the energy range from the energy threshold to 6 keV.

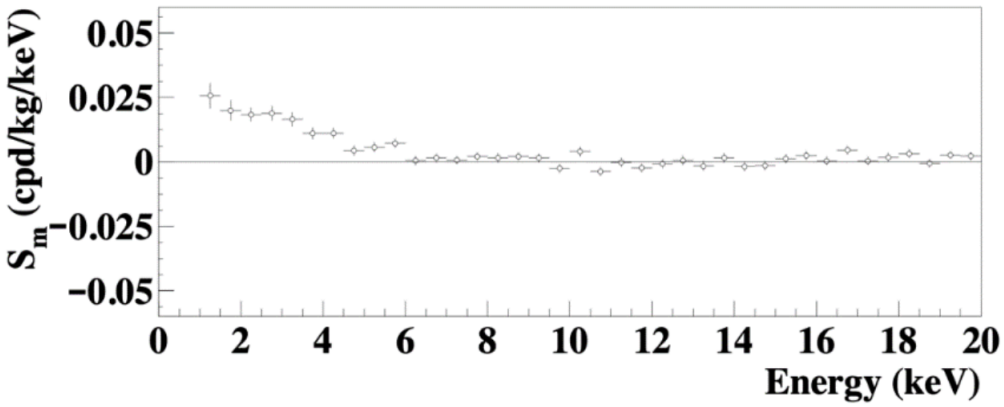

Figure 15. Modulation amplitudes, S_m, for the whole data sets: DAMA/NaI, DAMA/LIBRA–phase1 and DAMA/LIBRA–phase2 (total exposure: 2.86 ton × yr) above 2 keV; below 2 keV only the DAMA/LIBRA–phase2 exposure (1.53 t × yr) is available and used. The energy bin ΔE is 0.5 keV. A clear modulation is present in the lowest energy region, while S_m values compatible with zero are present just above. See ref. [9].

The upper limit is instead derived from the unmodulated signal constraints provided in ref. [106,107], where the following upper limits on the unmodulated signal are given: <0.8 counts/(day · kg · keV) in 1–2 keV range, <0.24 counts/(day · kg · keV) in 2–3 keV range, <0.12 counts/(day · kg · keV) in 3–4 keV range. Thus, assuming a γ-ray energy of 2.5 keV and including the energy resolution of the detectors, the most conservative limit is obtained from the third energy range.

Finally, considering that the time dependence of the rate is given only by the density parameter for the dark atoms model considered here, we can write:

$$\frac{S_m}{S_0} = \frac{\Delta\rho_O}{\rho_O^0} > 0.139. \tag{67}$$

This lower limit must be taken into account when selecting the range of the possible free parameters of the model.

In conclusion, the annual modulation results of DAMA/NaI and DAMA/LIBRA point out the following value of the capture rate in the dark atoms model considered here:

$$\frac{\Delta\rho_O}{M_O}(\langle v_1\sigma_1\rangle + \langle v_2\sigma_2\rangle) = (2.00 \pm 0.13) \times 10^{-31}\ \mathrm{s}^{-1}. \tag{68}$$

7.2. Diurnal Modulation

While the annual modulation is driven by the Earth's revolution, the Earth's daily rotation introduces a smaller diurnal modulation. The expected amplitude of this effect is suppressed relative to the annual modulation by approximately a factor of $\simeq$0.016 at the Gran Sasso latitude [11,100].

The DAMA collaboration has released an analysis where the DAMA/LIBRA–phase1 data set, corresponding to 1.04 ton $\times$ years of exposure, was analyzed in therms of diurnal modulation in both solar and sidereal time [11]. The analysis searched for time-dependent residuals in the counting rate of *single-hit* low-energy events. No significant diurnal modulation was observed at the present sensitivity.

This null result is consistent with expectations, since the amplitude of the diurnal modulation predicted from the observed annual modulation is below the sensitivity of DAMA/LIBRA–phase1. Thus, while the diurnal analysis provides an important cross-check, the non-observation is not in conflict with the annual modulation result.

The laboratory velocity with respect to the Galactic frame $\vec{v}_{lab}(t)$ is the sum of several contributions as detailed in Equation (33). Typical speeds are the Sun's velocity $v_s = |\vec{v}_{LSR} + \vec{v}_\odot| \approx 232\ \mathrm{km\,s}^{-1}$, the Earth revolution velocity $v_{rev} = |\vec{v}_{rev}| \approx 29.8\ \mathrm{km\,s}^{-1}$ and the rotational speed at the detector latitude $v_{rot} = |\vec{v}_{rot}|$, that is, the rotational speed at the equator ($0.47\ \mathrm{km\,s}^{-1}$) reduced by $\cos\varphi$ at latitude φ.

The event rates expected in many models depend mainly on the magnitude of $\vec{v}_{lab}(t)$, $v_{lab}(t) = |\vec{v}_{lab}(t)|$. Expanding to first order in the small time-dependent velocities yields a time-dependent modulation of the counting rate in a given energy bin k [11,100]:

$$S_k(t) \simeq S_{0,k} + \left.\frac{\partial S_k}{\partial v_{\mathrm{lab}}}\right|_{v_s} [v_{rev} A_m \cos\omega(t - t_0) + v_{rot} A_d \cos\omega_{\mathrm{rot}}(t - t_d)], \tag{69}$$

where $S_{0,k}$ is the constant component, A_m and A_d are geometry-dependent coefficients (of order unity; $A_m \approx 0.489$, $A_d \approx 0.671$ for typical Galactic parameters), ω is the annual angular frequency, ω_{rot} the sidereal daily frequency, and t_0 and t_d are the corresponding phases. As shown in Figure 4, the annual term produces the familiar 2 June maximum, while the diurnal term has a sidereal-phase maximum near local sidereal time $\sim$ 14 h for detectors at LNGS longitude (depending weakly on Galactic rotation speed v_0).

Because both annual and diurnal amplitudes arise from the same velocity-derivative term, their ratio is largely model-independent and depends chiefly on the ratio of v_{rot} to v_{rev} and on geometry factors:

$$R_{\mathrm{dy}} \equiv \frac{S_d}{S_m} \simeq \frac{v_{rot} A_d}{v_{rev} A_m} \approx 0.0214 \cos\varphi\,, \tag{70}$$

where φ is the laboratory latitude. For LNGS ($\varphi \simeq 42.45^\circ$), this yields $R_{\mathrm{dy}} \approx 0.016$. Thus, if an annual modulation amplitude S_m is observed, the expected diurnal amplitude S_d can be estimated model-independently by multiplying by R_{dy}. Considering the full data set DAMA/NaI, DAMA/LIBRA–phase1 and phase2, the annual modulation result in the (2–6) keV window is $S_m \simeq 0.00996$ cpd/kg/keV [9], and the expected diurnal amplitude is $\sim 1.6\times10^{-4}$ cpd/kg/keV.

To probe the diurnal variation, the data of DAMA/LIBRA considered in ref. [11] (1.04 ton × years) were grouped in one-hour bins of either solar and sidereal time. The residual rate for each hour bin is computed by subtracting the 24 h average rate for that day (i.e., removing the daily mean) and then averaging over detectors, energy bins, and annual cycles. These residuals are reported in Figure 16. By construction, the annual modulation (with a period of one year) is largely washed out in this averaging, since data collection is approximately uniform over the diurnal hours throughout the year; its systematic contribution to the 24 h average is negligible ($\ll 10^{-4}$ of the daily mean).

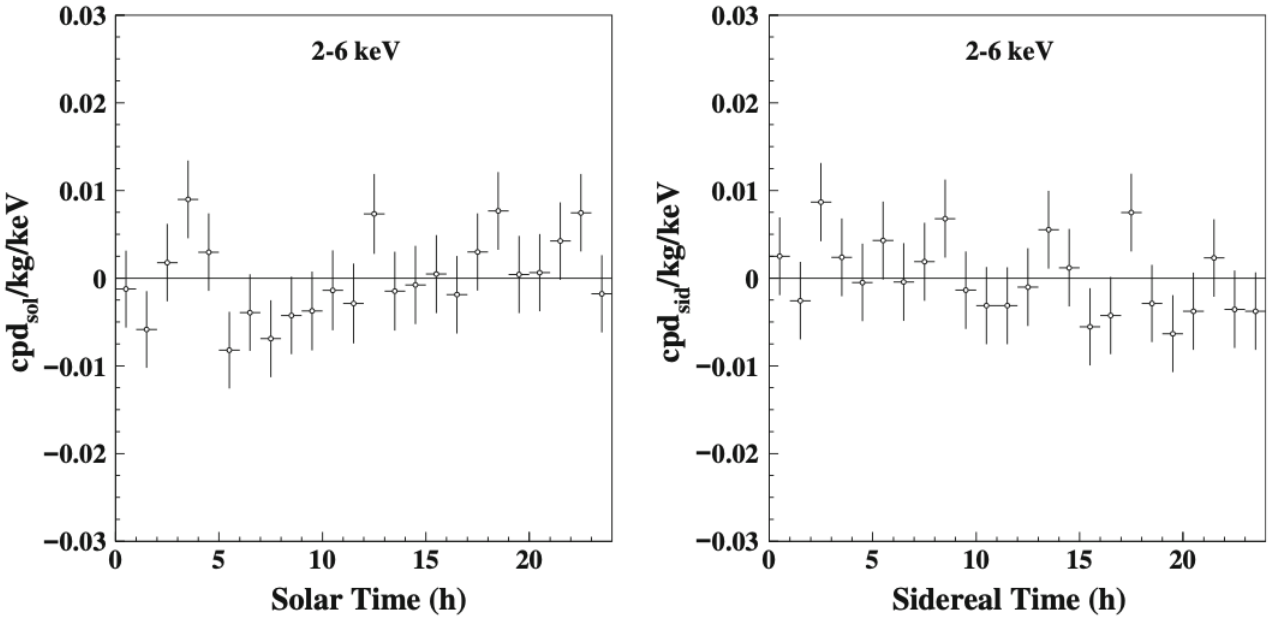

Figure 16. Experimental model-independent diurnal residual rate of the *single-hit* scintillation events in the (2–6) keV energy interval for the data set considered in ref. [11] (1.04 ton × years) as a function of the solar (**left**) and sidereal (**right**) hour.

The used data set of DAMA/LIBRA–phase1 found no statistically significant diurnal variation in *single-hit* low-energy events in sidereal time. The achieved result can be summarized as follows:

- In the (2–6) keV energy interval binned with 1 h bins, the χ^2 test returned a value (χ^2/d.o.f. $= 21.2/24$) compatible with random fluctuations, and the run test likewise did not reject randomness.
- A direct cosine fit for sidereal time with fixed phase at 14 h yielded $A_d^{\rm exp} = -(1.0 \pm 1.3) \times 10^{-3}$ cpd/kg/keV, consistent with zero. Using the Feldman–Cousins approach, an upper limit of $A_d^{\rm exp} \leq 1.2 \times 10^{-3}$ cpd/kg/keV (90% C.L.) was quoted.
- The experimental uncertainty $\sigma(A_d)$ derived from the data is $\sim 1.3 \times 10^{-3}$ cpd/kg/keV, consistent with theoretical sensitivity estimates given typical background rates and exposure [100].

These results imply that the diurnal amplitude expected from the observed DAMA annual amplitude result ($\sim 1.6 \times 10^{-4}$ cpd/kg/keV) is far below the detection threshold of the considered data set, which could exclude diurnal amplitudes at the $\sim 10^{-3}$ cpd/kg/keV scale but not down to the $\sim 10^{-4}$ level required by the model-independent expectation.

This fact is confirmed by the simulation carried out using the stochastic Monte Carlo method described in Section 5, as can be seen in Figure 17 which reports the results of Monte Carlo simulation for the daily modulation of the residual count rate as a function of solar time (*left*) and Greenwich Mean Sidereal Time (*right*).

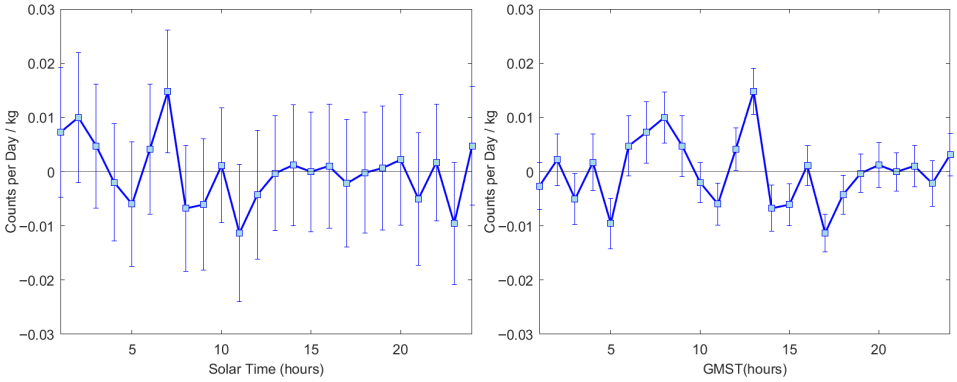

Figure 17. Results of Monte Carlo simulation for the daily modulation of the residual count rate as a function of solar time (**left**) and Greenwich Mean Sidereal Time (**right**). Error bars represent the variance.

In conclusion, following the same procedure as in Equation (68) and considering that the energy interval is $\Delta E = 4$ keV, the results of diurnal modulation point out an upper limit on the diurnal modulation amplitude of the counting rate in the considered model:

$$\frac{\delta\rho_O}{M_O}(\langle v_1\sigma_1\rangle + \langle v_2\sigma_2\rangle) \leq 1.4 \times 10^{-32}\ \mathrm{s}^{-1} \tag{71}$$

where $\delta\rho_O$ is the diurnal modulation amplitude expected from the dark atom candidates considered.

7.3. High-Energy Gamma Rays

As discussed above, dark atoms can generate high-energy gamma rays within the NaI(Tl) detectors through their interactions and subsequent bindings with Iodine nuclei. For simplicity, we assume that the bound states formed between dark atoms and Iodine nuclei emit gamma rays with energy E_γ at a rate R_γ. These gamma rays are detected by the NaI(Tl) detectors with an efficiency η, resulting in S counts in the photo-peak at energy E_γ. Accordingly, the production rate of gamma rays can be expressed as:

$$R_\gamma = \frac{S}{\eta W N_I}, \tag{72}$$

where W is the total exposure and $N_I = 4.015 \times 10^{24}$ is the number of Iodine nuclei per kilogram of detector material.

No anomalous gamma-ray emissions in the hundreds-to-thousands keV range have been observed, allowing us to place constraints on the dark atom model. In this section, we evaluate these constraints.

Also to this end, we refer only to the material published by the DAMA collaboration in ref. [12], which reports a search for gamma-ray emissions in the 90–450 keV range using a subset of the DAMA/NaI data (with a total exposure of W = 34,866 kg $\times$ day). The analysis reported there [12] was aimed at identifying possible exotic processes involving ^{127}I and ^{23}Na nuclei. Table 8 lists, for each peak considered in ref. [12], the excluded peak area S and the corresponding upper limits on the gamma-emission rate from Iodine nuclei R_γ.

Table 8. Limits of R_γ evaluated from a set of DAMA/NaI data [12]. The limits are given at 90% C.L.

E_γ (keV)	Efficiency η	Area of the Peak S	R_γ $(10^{-31}\,\mathrm{s}^{-1})$
90.8	0.99	<3149	<2.63
236.1	0.89	<3418	<3.18
408.2	0.72	<3061	<3.52
441.1	0.60	<3009	<4.15
451.2	0.61	<2974	<4.03

Conservatively, therefore, one can conclude that the total gamma-emission rate in the ≃90–500 keV energy region is $R_\gamma \leq 4 \times 10^{-31}\ \mathrm{s}^{-1}$. It should be emphasized that this limit remains valid in the case of monochromatic gamma-ray emission from the binding of dark atoms to Iodine nuclei. In contrast, a wider gamma-ray energy distribution yields substantially weaker limits, possibly reduced by orders of magnitude.

7.4. Summary on the DAMA Annual Modulation and Other Constraints

Finally, the results of DAMA/NaI and DAMA/LIBRA–phase1,2 described in Sections 7.1–7.3, can be summarized as follows. The annual modulation results point out the following value of the modulation amplitude of the counting rate in the dark atom model:

$$\frac{\Delta\rho_O}{M_O}(\langle v_1\sigma_1\rangle + \langle v_2\sigma_2\rangle) = (2.00 \pm 0.13) \times 10^{-31}\ \mathrm{s}^{-1}, \tag{73}$$

with the upper limit on the unmodulated signal:

$$\frac{S_m}{S_0} = \frac{\Delta\rho_O}{\rho_O^0} > 0.139. \tag{74}$$

The results of diurnal modulation point out an upper limit on the diurnal modulation amplitude of the counting rate in the dark atom model:

$$\frac{\delta\rho_O}{M_O}(\langle v_1\sigma_1\rangle + \langle v_2\sigma_2\rangle) \leq 1.4 \times 10^{-32}\ \mathrm{s}^{-1}, \tag{75}$$

and the total gamma-emission rate in the energy region of hundreds of keV to MeV is $R_\gamma \leq 4 \times 10^{-31}\ \mathrm{s}^{-1}$.

8. Constraints of the Dark Atom Model Parameters Derived by Applying DAMA Published Results as a Benchmark

It is necessary to determine the values of the parameter r^*, which defines the position of the nucleus of the substance $R^*_{OA} = r^* + R_{nuc} + R_{He}$ at which repolarization of the dark atom occurs and which satisfies the physically justified range of values for the position of nucleus of substance during repolarization of the dark atom of OHe: 8.5 fm $\lesssim R^*_{OA} \lesssim$ 18.5 fm, defined in Section 6.1 using Formula (36), and the values of the O^{--} particle spin for which low-energy bound states of OHe dark atoms with sodium nuclei are formed in the energy range of 1 keV to 6 keV, satisfying the count rate constraints of the DAMA experiment.

Numerical analysis using the quantum mechanical model of dark atom–nucleus interaction, developed for the specific case of the XHe dark atom hypothesis (where the electric charge of the X particle is -2), i.e., for the O-helium dark atom, including calculation of the sodium nucleus radiative capture rate via Formula (60), demonstrates that within the uncertainties of nuclear and atomic physics parameters, low-energy bound states of OHe with sodium nuclei in the 1 keV to 6 keV range are formed and satisfy the DAMA/LIBRA

count rate constraints (66) for the following parameters of the *O*He-Na system and the O^{--} particle:

1. For parameter $r^* = 12$ fm and O^{--} particle spin $I_{O^{--}} = 3/2$, a bound state of the *O*He dark atom with the Na nucleus is formed with energy level $E_\gamma \approx -1.84$ keV and sodium nucleus radiative capture rate $(\sigma^{1\to0}_{OHe-Na} \cdot v) \approx 3 \times 10^{-30}$ cm^3/s. Numerical calculation of the count rate using Formula (64) for this capture rate yields values closely matching those required by the DAMA/NaI and DAMA/LIBRA experimental results (66) for O^{--} particle mass satisfying $M_O \geq 4.2$ TeV. Specifically, for mass $M_O = 4.2$ TeV, the numerical calculation gives $R_{numerical} \approx 0.498 + 3.21 \times 10^{-2} \cos(\omega(t - t_0))$ counts/(day·kg).
2. For parameter $r^* = 13$ fm and O^{--} particle spin $I_{O^{--}} = 1$, a bound state of the *O*He dark atom with the Na nucleus is formed with energy level $E_\gamma \approx -2.38$ keV and sodium nucleus radiative capture rate $(\sigma^{1\to0}_{OHe-Na} \cdot v) \approx 1.6 \times 10^{-30}$ cm^3/s. Numerical calculation of the count rate (64) for this capture rate yields values closely matching the DAMA/NaI and DAMA/ LIBRA experimental constraints (66) for O^{--} particle mass satisfying $M_O \geq 2.22$ TeV. Specifically, for mass $M_O = 2.22$ TeV, the numerical calculation gives $R_{numerical} \approx 0.496 + 3.19 \times 10^{-2} \cos(\omega(t - t_0))$ counts/(day·kg).

In the interaction of an iodine nucleus with an *O*He dark atom for an O^{--} particle spin of $I_{O^{--}} = 1$ or $3/2$, the energy of the ground bound state *O*He–I is approximately $E_{1_I} \approx -1.07$ MeV at $r^* = 11$ fm and $E_{1_I} \approx -950$ keV at $r^* = 12$ fm, while the energy of the first excited bound state *O*He–I is approximately $E_{2_I} \approx -760$ keV at $r^* = 11$ fm and $E_{2_I} \approx -690$ keV at $r^* = 12$ fm. The calculation of the radiative capture rate of iodine into the ground bound state *O*He–I, $l_i = 1 \to l_f = 0$ using Formula (60) at $r^* = 11$ fm yields $(\sigma^{1\to0}_{OHe-I} \cdot v) \approx 1.4 \times 10^{-31}$ cm^3/s and at $r^* = 12$ fm yields $(\sigma^{1\to0}_{OHe-I} \cdot v) \approx 1.5 \times 10^{-31}$ cm^3/s. The calculation of the radiative capture rate of iodine into the first excited bound state *O*He–I, $l_i = 0 \to l_f = 1$, using Formula (61) at $r^* = 11$ fm yields $(\sigma^{0\to1}_{OHe-I} \cdot v) \approx 8 \times 10^{-32}$ cm^3/s and at $r^* = 12$ fm yields $(\sigma^{0\to1}_{OHe-I} \cdot v) \approx 7 \times 10^{-32}$ cm^3/s. It is evident that the radiative capture cross-sections of iodine are suppressed compared to the radiative capture of the sodium nucleus.

Numerical calculation of the count rates for the obtained iodine radiative capture rates using Formula (64) for an O^{--} particle mass of $M_O = 2$ TeV gives a time-independent signal amplitude of $R^{1\to0}_{numerical} \approx 1.5 \times 10^{-31}$ s^{-1} for the $l_i = 1 \to l_f = 0$ transition and $R^{0\to1}_{numerical} \approx 7 \times 10^{-32}$ s^{-1} for the $l_i = 0 \to l_f = 1$ transition. This satisfies the constraint from the DAMA/NaI and DAMA/LIBRA experiments on the total gamma-ray emission rate in the energy range from hundreds of keV to MeV, which is $R_\gamma \leq 4 \times 10^{-31}$ s^{-1}. Consequently, if an excited bound state of *O*He–I is formed, the transition of the iodine nucleus from the excited bound state to the ground bound state, emitting a photon with energy $\Delta E_I = E_{2_I} - E_{1_I} \approx -310$ keV at $r^* = 11$ fm or $\Delta E_I = E_{2_I} - E_{1_I} \approx -260$ keV at $r^* = 12$ fm, will also be suppressed.

In the future, for the most accurate and physically consistent description of the interaction between a dark atom and a nucleus, it will be necessary to consider dark atom models with an electric charge of the *X* particle greater than -2. Therefore, to improve the accuracy of calculating the polarization dipole moments of the dark atom and consequently to more precisely reconstruct the total effective interaction potential of *X*He with the nucleus and calculate the radiative capture cross-section, it is planned to refine the numerical quantum mechanical model by accounting for the non-point-like nature of the interacting particles in the *X*He–nucleus system. Specifically, it is essential to include the distribution of electric charge and nucleons in the interacting nuclei, the deformation of the nucleus, and its orientation relative to the dark atom when calculating nuclear and electromagnetic potentials.

9. Conclusions

This article provides a comprehensive description of the dark atom scenario as a viable explanation for the phenomenon of dark matter and signs of its direct detection. The dark atom model is built upon the existence of a stable, multi-charged X^{-2n} particle that, in the early Universe, forms neutral dark atoms by binding with n primordial ^{4}He nuclei via the ordinary electromagnetic Coulomb force.

We consistently reviewed the theoretical underpinnings of this framework, beginning with the possible origins of multi-charged stable particles in extensions of the Standard Model, such as Walking Technicolor. The cosmological evolution of dark atoms was described, focusing on the critical balance between baryon asymmetry and the X^{-2n} particle excess provided by sphaleron transitions, and the subsequent capture by helium during Big Bang nucleosynthesis. This process sets important constraints on the mass and charge of the X^{-2n} particle and influences the primordial abundances of light elements.

A central part of our analysis is dedicated to the phenomenology of dark atoms in the context of DM direct detection experiments. A numerical Monte Carlo model was developed to simulate the capture and propagation of dark atoms through the Earth, accounting for terrain effects, thermalization, and diffusion toward the center of Earth. This simulation also provides physical basis for investigating dark matter annual and diurnal modulations signature in underground setups.

As a benchmark analysis, the model predictions were quantitatively compared with the long-standing DAMA/NaI and DAMA/LIBRA observations. The dark atom model naturally accommodates the robust annual modulation effect in the 1–6 keV energy range, yielding a specific relationship between the modulation amplitude and the dark atom capture rate. Furthermore, the predicted diurnal modulation amplitude, suppressed by a factor consistent with the Earth's rotational velocity, remains below the current sensitivity of DAMA, which is in agreement with their null result. Constraints from the non-observation of high-energy gamma rays associated with the binding of dark atoms to iodine nuclei were also evaluated and found to be compatible with the model for a wide range of parameters.

To address the key challenge of how a neutral, composite dark atom can interact to produce a low-energy signal, we developed a quantum-mechanical description of the bound-state formation between an *O*He dark atom ($n = 1$) and nuclei (Na and I). By reconstructing the total effective interaction potential, which includes nuclear, Coulomb, centrifugal, and Stark contributions, we demonstrated the existence of potential wells capable of supporting bound states with binding energies in the keV range for sodium. The calculated radiative capture cross-sections for sodium are larger than for iodine, for which they are suppressed, offering a natural explanation for the target-material dependence observed in direct detection experiments.

In summary, the dark atom model, here reviewed in various aspects and details, provides a self-consistent and phenomenologically extensive framework able to account for the published DAMA results on annual and diurnal modulation signatures and on some energy spectrum behavior, as well as for absence of an annual modulation effect in detectors based on heavy nuclei while remaining compatible with other constraints. The model's viability hinges on a specific set of parameters related to the mass, charge, and spin of the X^{-2n} particle, as well as the nuclear physics features of the OHe–nucleus system.

Future theoretical works should refine the quantum mechanical calculations for higher charges ($n > 1$), incorporate more realistic description of nuclear structures, and pursue dedicated and comprehensive study of the open issues related to the dark atom scenario.

https://doi.org/10.3390/universe12040116

Author Contributions: Conceptualization, M.K.; Formal analysis, P.B., R.B., V.B., T.B., A.K., V.K., A.M. and D.S.; Investigation, P.B., R.B., V.B., T.B., A.K., M.K., V.K., A.M. and D.S.; Writing—original draft, P.B., R.B., V.B., T.B., A.K., M.K., V.K., A.M. and D.S.; Writing—review and editing, P.B., R.B., V.B., T.B., A.K., M.K., V.K., A.M. and D.S. All authors have read and agreed to the published version of the manuscript.

Funding: The work of T.E.B. was performed in Southern Federal University with financial support of grant of Russian Science Foundation № 25-07-IF. The research of A.K., V.K. and D.O.S. was carried out in the Southern Federal University with financial support from the Ministry of Science and Higher Education of the Russian Federation (State contract FENW-2026-0028). The work of A.M. was carried out with the financial support provided by the Russian Ministry of Science and Higher Education, project "Fundamental and applied research of cosmic rays", No. FSWU-2023-0068.

Data Availability Statement: No new data were created or analyzed in this study.

Acknowledgments: We thank the referees for careful reading of the manuscript and their interest to our work, which helped to improve the presentation.

Conflicts of Interest: The authors declare no conflicts of interest.

References

1. Sannino, F.; Tuominen, K. Orientifold theory dynamics and symmetry breaking. *Phys. Rev. D* **2005**, *71*, 051901. [CrossRef]
2. Hong, D.K.; Hsu, S.D.; Sannino, F. Composite Higgs from higher representations. *Phys. Lett. B* **2004**, *597*, 89–93. [CrossRef]
3. Dietrich, D.D.; Sannino, F.; Tuominen, K. Light composite Higgs from higher representations versus electroweak precision measurements. Predictions for LHC. *Phys. Rev. D* **2005**, *72*, 055001. [CrossRef]
4. Dietrich, D.D.; Sannino, F.; Tuominen, K. Light composite Higgs and precision electroweak measurements on the Z resonance: An update. *Phys. Rev. D* **2006**, *73*, 037701. [CrossRef]
5. Gudnason, S.B.; Kouvaris, C.; Sannino, F. Dark matter from new technicolor theories. *Phys. Rev. D* **2006**, *74*, 095008. [CrossRef]
6. Khlopov, M.Y.; Kouvaris, C. Strong interactive massive particles from a strong coupled theory. *Phys. Rev. D* **2008**, *77*, 065002. [CrossRef]
7. Beylin, V.A.; Bikbaev, T.E.; Khlopov, M.Y.; Mayorov, A.G.; Sopin, D.O. dark atoms of Nuclear Interacting Dark Matter. *Universe* **2024**, *10*, 368. [CrossRef]
8. Bernabei, R.; Belli, P.; Bussolotti, A.; Cappella, F.; Caracciolo, V.; Cerulli, R.; Dai, C.J.; d'Angelo, A.; Di Marco, A.; Ferrari, N.; et al. The DAMA project: Achievements, implications and perspectives. *Prog. Part. Nucl. Phys.* **2020**, *114*, 103810. [CrossRef]
9. Bernabei, R.; Belli, P.; Bussolotti, A.; Caracciolo, V.; Cappella, F.; Cerulli, R.; Dai, C.J.; d'Angelo, A.; Ferrari, N.; Incicchitti, A.; et al. Further Results from DAMA/LIBRA-phase2 and Perspectives. *Nucl. Phys. At. Energy* **2021**, *22*, 329. [CrossRef]
10. See Publications List in the DAMA Web Site. Available online: https://dama.web.roma2.infn.it/ (accessed on 31 December 2025).
11. Bernabei, R.; Belli, P.; Cappella, F.; Caracciolo, V.; Castellano, S.; Cerulli, R.; Dai, C.J.; d'Angelo, A.; d'Angelo, S.; Di Marco, A.; et al. Model independent result on possible diurnal effect in DAMA/LIBRA–phase1. *Eur. Phys. J. C* **2014**, *74*, 2827. [CrossRef]
12. Belli, P.; Bernabei, R.; Dai, C.J.; He, H.L.; Ignesti, G.; Incicchitti, A.; Kuang, H.H.; Ma, J.M.; Montecchia, F.; Ponkratenko, O.A.; et al. New limits on the nuclear levels excitation of ^{127}I and ^{23}Na during charge non-conservation. *Phys. Rev. C* **1999**, *60*, 065501. [CrossRef]
13. Carlin, N.; Cho, J.Y.; Choi, J.J.; Choi, S.; Ezeribe, A.C.; França, L.E.; Ha, C.; Hahn, I.S.; Hollick, S.J.; Hong, S.B.; et al. Combined Annual Modulation Dark Matter Search with COSINE-100 and ANAIS-112. *Phys. Rev. Lett.* **2025**, *135*, 121002. [CrossRef]
14. Aprile, E.; Aalbers, J.; Abe, K.; Ahmed Maouloud, S.; Althueser, L.; Andrieu, B.; Angelino, E.; Antón Martin, D.; Armbruster, S.R.; Arneodo, F.; et al. WIMP Dark Matter Search using a 3.1 tonne × year Exposure of the XENONnT Experiment. *Phys. Rev. Lett.* **2025**, *135*, 221003. [CrossRef]
15. Albakry, M.F. et al. [SuperCDMS Collaboration]. Search for low-mass electron-recoil dark matter using a single-charge sensitive SuperCDMS-HVeV Detector. *arXiv* **2026**, arXiv:2509.03608.
16. Milligan, L.J. [on behalf of the SABRE South Collaboration]. The SABRE South Experiment at the Stawell Underground Physics Laboratory. In Proceedings of the 42nd International Conference on High Energy Physics (ICHEP2024), Prague, Czech Republic, 18–24 July 2024.
17. Acharya, B. et al. [MoEDAL Collaboration]. The Physical Programme of the MoEDAL Experiment at the LHC. *Int. J. Mod. Phys. A* **2014**, *29*, 1430050. [CrossRef]
18. Acharya, B. et al. [MoEDAL Collaboration]. Search for Highly Ionizing Particles in pp Collisions during LHC Run 2 using the Full MoEDAL Detector. *Phys. Rev. Lett.* **2025**, *134*, 071802. [CrossRef]

19. Aad, G. et al. [ATLAS Collaboration]. Search for long-lived charged particles using large specific ionisation loss and time of flight in 140 fb^{-1} of pp collisions at $\sqrt{s}$ = 13 TeV with the ATLAS detector. *J. High Energy Phys.* **2025**, *2025*, 140.
20. Altakach, M.M.; Lamba, P.; Masełek, R.; Mitsou, V.A.; Sakurai, K. Discovery prospects for long-lived multiply charged particles at the LHC. *Eur. Phys. J. C* **2022**, *82*, 848. [CrossRef]
21. Hayrapetyan, A. et al. [CMS Collaboration]. Search for heavy long-lived charged particles with large ionization energy loss in proton-proton collisions at $\sqrt{s}$ = 13 TeV. *J. High Energy Phys.* **2025**, *2025*, 109.
22. Haas, A.; Hill, G.; Izaugirre, E.; Yavin, I. Looking for milli-charged particles with a new experiment at the LHC. *Phys. Lett.* **2015**, *746*, 117. [CrossRef]
23. Aalbers, J. et al. [LZ Collaboration]. First constraints on Atmospheric Milli-charged Particles with the LUX-Zeplin Experiment. *Phys. Rev. Lett.* **2025**, *134*, 241802. [CrossRef]
24. Adams, D.Q. et al. [CUORE Collaboration]. Search for Fractionally Charged Particles with CUORE. *Phys. Rev. Lett.* **2024**, *133*, 241801. [CrossRef] [PubMed]
25. Burdin, S.; Fairbairn, M.; Mermod, P.; Milstead, D.; Pinfold, J.; Sloan, T.; Taylor, W. Non-collider searches for stable massive particles. *Phys. Rep.* **2015**, *582*, 1–52. [CrossRef]
26. Munoz, V.; Arguelles, G.; Kelly, K. Searching for milli-charged particles production in cosmic ray showers. In Proceedings of the 37th International Cosmic Ray Conference (ICRC 2021), Online, 12–23 July 2021.
27. Knurenko, S.; Petrov, I. Studies of ultra-high energy cosmic rays by the Yakutsk air shower array based on the Cherenkov light detector technique. *Adv. Space Res.* **2024**, *74*, 9. [CrossRef]
28. Wu, H.; Hardy, E.; Song, N. Searching for heavy milli-charged particles from the atmosphere. *Phys. Rev. D* **2024**, *110*, 115037. [CrossRef]
29. Juger, S.; Kvedaraite, S.; Perez, G.; Savoray, I. Bounds and Prospects for Stable Multiply Charged Particles at the LHC. *J. High Energy Phys.* **2019**, *2019*, 41. [CrossRef]
30. Cacciapaglia, G.; Kollias, K.; Deandrea, A.; Sannino, F. Grand-unification Theory Atlas: Standard Model and Beyond. *arXiv* **2025**, arXiv:2507.06368. [CrossRef]
31. Barcelo, R.; Masip, M.; Moreno-Torrez, M. Little Higgs models with a light T-quark. *Nucl. Phys. B* **2007**, *782*, 159. [CrossRef]
32. Wang, L.; Yang, J.-M.; Zhang, Y.; Zhu, P.; Zhu, R. A concise review of some Higgs-related new physics models in light of current experiments. *Universe* **2023**, *9*, 178. [CrossRef]
33. Beylin, V.; Khlopov, M.; Kuksa, V.; Volchanskiy, N. Hadronic and Hadron-Like physics of Dark Matter. *Symmetry* **2019**, *11*, 587. [CrossRef]
34. Volchanskiy, N.; Beylin, V.; Kuksa, V. Models of hypercolor based on symplectic gauge group with three heavy vectorlike hyperquarks. *Int. J. Mod. Phys. D* **2019**, *28*, 1941002. [CrossRef]
35. Herrera, J.; Benavides, R.; Ponce, W. Flavor changing neutral currents with a fourth family of quarks. *Phys. Rev. D* **2008**, *78*, 073008. [CrossRef]
36. Benavides, R.; Ponce, W.; Giraldo, Y. $SU(3)_C xSU(3)_L xU(1)_X$ models with four families. *Phys. Rev. D* **2010**, *82*, 013004. [CrossRef]
37. Bachiry, V.; Azizi, K.; Sultansoy, S. Properties of bound states containing fourth family quarks. *J. Phys. Conf. Ser.* **2012**, *347*, 012027.
38. Shrock, R. Variants of the Standard Model with electroweak singlet quarks. *Phys. Rev. D* **2008**, *78*, 076009. [CrossRef]
39. Beylin, V.; Kuksa, V. Dark Matter in the Standard Model Extension with Singlet Quark. *Adv. High Energy Phys.* **2018**, *2018*, 8670954. [CrossRef]
40. Banerjee, A.; Franzosi, D.; Ferretti, G. Modelling vector-like quark in partial compositeness framework. *J. High Energy Phys.* **2022**, *2022*, 200. [CrossRef]
41. Buckley, A.; Butterworth, J.; Corpe, L.; Huang, D.; Sun, P. New sensitivity of current LHC measurements to vector-like quarks. *SciPost Phys.* **2020**, *9*, 069. [CrossRef]
42. Banerjee, A.; Bergeaas Kuutmann, E.; Ellajosyula, V.; Enberg, R.; Ferretti, G.; Panizzi, L. Vector-like quarks: Status and new directions at the LHC. *SciPost Phys. Core* **2024**, *7*, 079. [CrossRef]
43. Adhikary, A.; Olechowski, M.; Rosiek, J.; Ryczkowski, M. Theoretical constraints on models with vectorlike fermions. *Phys. Rev. D* **2024**, *110*, 075029. [CrossRef]
44. Benbric, R.; Berrouj, M.; Boukidi, M.; Kahime, K. Exploring vectorlike top-quarks pair production via charged Higgs decay in multi-b jets and opposite-sign dilepton final states at the LHC. *Eur. Phys. J. C* **2025**, *85*, 500. [CrossRef]
45. Leonardi, R.; Panella, O.; Fano, L. Doubly charged heavy leptons at LHC via contact interactions. *Phys. Rev. D* **2014**, *90*, 035001. [CrossRef]
46. Barducci, D.; Deandrea, A.; Moretti, S.; Panizzi, L.; Prager, H. Characterizing dark matter interacting with extra charged leptons. *Phys. Rev. D* **2018**, *97*, 075006. [CrossRef]
47. Glashow, S.L. A sinister extension of the Standard Model to $SU(3)xSU(2)xSU(2)'xU(1)$. *arXiv* **2005**, arXiv:hep-ph/0504287.
48. Fargion, D.; Khlopov, M.; Stephan, C. Dark Matter with invisible light from heavy double-charged lepton of almost-commutative geometry. *Class. Quantum Gravity* **2006**, *23*, 7305–7354.

49. Foadi, R.; Frandsen, M.; Ryttov, T.; Sannino, F. Minimal Walking Technicolor: Setup for collider physics. *Phys. Rev. D* **2007**, *76*, 055005. [CrossRef]
50. Kainulainen, K.; Virkajarvi, J.; Tuominen, K. Weakly interacting dark matter from the minimal walking technicolor. *J. Cosmol. Astropart. Phys.* **2010**, *2010*, 029. [CrossRef]
51. Gudnason, S.; Kouvaris, C.; Sannino, F. Towards walking technicolor: Effective thories and dark matter. *Phys. Rev. D* **2006**, *73*, 115003. [CrossRef]
52. Pasechnik, R.; Beylin, V.; Kuksa, V.; Vereshkov, G. Chiral-symmetric technicolor with standard model Higgs boson. *Phys. Rev. D* **2013**, *88*, 075009. [CrossRef]
53. Bellazini, B.; Csaki, C.; Serra, J. Composite Higgses. *Eur. Phys. J. C* **2014**, *74*, 2766. [CrossRef]
54. Chivukula, R.S.; Walker, T.P. Technicolor cosmology. *Nucl. Phys. B* **1990**, *329*, 445. [CrossRef]
55. Cacciapaglia, G.; Frandsen, M.T.; Huang, W.-C.; Rosenlyst, M.; Sørensen, P. Techni-composite Higgs models with symmetric and anti-symmetric dark matter candidates. *Phys. Rev. D* **2022**, *106*, 075022. [CrossRef]
56. Doff, A.; Natale, A.; Rodrigues, P. Light composite Higgs from an effective action for Technicolor. *Phys. Rev. D* **2008**, *77*, 075012. [CrossRef]
57. Dugan, M.J.; Georgi, H.J.; Kaplan, D.B. Anatomy of a Composite Higgs Model. *Nucl. Phys. B* **1985**, *254*, 299. [CrossRef]
58. Agashe, K.; Loutino, R.; Pomarol, A. The minimal composite Higgs model. *Nucl. Phys. B* **2005**, *719*, 165. [CrossRef]
59. Alanne, T.; Franzosi, D.B.; Frandsen, M. Partially composite Goldstone Higgs boson. *Phys. Rev. D* **2017**, *96*, 095012. [CrossRef]
60. Khlopov, M.Y.; Mayorov, A.G.; Soldatov, E.Y. Towards nuclear physics of OHe dark matter. *Bled Work. Phys.* **2011**, *12*, 94.
61. Harvey, J.A.; Turner, M.S. Cosmological baryon and lepton number in the presence of electroweak fermion-number violation. *Phys. Rev. D* **1990**, *42*, 3344–3349. [CrossRef]
62. Beylin, V.A.; Khlopov, M.Y.; Sopin, D.O. Asymmetric Dark Matter in Baryon Asymmetrical Universe. *Symmetry* **2024**, *3*, 311. [CrossRef]
63. D'Onofrio, M.; Rummukainen, K.; Tranberg, A. Sphaleron Rate in the Minimal Standard Model. *Phys. Rev. Lett.* **2014**, *113*, 1079–7114. [CrossRef]
64. Aad, G. et al. [ATLAS Collaboration]. Search for heavy long-lived multi-charged particles in the full LHC Run 2 pp collision data at $\sqrt{s}$ = 13 TeV using the ATLAS detector. *Phys. Lett. B* **2023**, *847*, 138316. [CrossRef]
65. Pitrou, C.; Coc, A.; Uzan, J.-P.; Vangioni, E. Precision big bang nucleosynthesis with improved Helium-4 predictions. *Phys. Rep.* **2018**, *754*, 1–66. [CrossRef]
66. Gorbunov, D.S.; Rubakov, V.A. *Introduction to the Theory of the Early Universe Hot Big Bang Theory*; World Scientific: Singapore, 2011.
67. Pospelov, M. Particle Physics Catalysis of Thermal Big Bang Nucleosynthesis. *Phys. Rev. Lett.* **2007**, *98*, 231301. [CrossRef]
68. Kohri, K.; Takayama, F. Big bang nucleosynthesis with long-lived charged massive particles. *Phys. Rev. D* **2007**, *76*, 063507. [CrossRef]
69. Kamimura, M.; Kino, Y.; Hiyama, E. Big Bang Nucleosynthesis Reactions Catalyzed by a Long Lived Negatively Charged Leptonic Particle. *Prog. Theor. Phys.* **2009**, *121*, 1059. [CrossRef]
70. Akhmedov, E.; Pospelov, M. BBN catalysis by doubly charged particles. *J. Cosmol. Astropart. Phys.* **2024**, *2024*, 028. [CrossRef]
71. Akhmedov, E. Nuclear fusion catalyzed by doubly charged scalars: Implications for energy production. *Phys. Rev. D* **2022**, *106*, 035013. [CrossRef]
72. Cahn, R.N.; Glashow, S.L. Chemical Signatures for Superheavy Elementary Particles. *Science* **1981**, *213*, 607–611. [CrossRef]
73. Antognini, A.; Kottmann, F.; Pohl, R. Laser spectroscopy of light muonic atoms and the nuclear charge radii. *SciPost Phys. Proc.* **2021**, *5*, 021. [CrossRef]
74. Angeli, I.; Marinova, K.P. Table of experimental nuclear ground state charge radii: An update. *At. Data Nucl. Data Tables* **2013**, *99*, 69–95. [CrossRef]
75. Schuhmann, K. et al. [The CREMA Collaboration]. The helion charge radius from laser spectroscopy of muonic helium-3 ions. *Science* **2025**, *388*, 6749. [CrossRef]
76. Krauth, J.J.; Schuhmann, K.; Ahmed, M.A.; Amaro, F.D.; Amaro, P.; Biraben, F.; Chen, T.-L.; Covita, D.S.; Dax, A.J.; Diepold, M.; et al. Measuring the *alpha*-particle charge radius with muonic helium-4 ions. *Nature* **2021**, *589*, 527–531. [CrossRef] [PubMed]
77. Friar, J.L. The Structure of Light Nuclei and Its Effect on Precise Atomic Measurements. In *Precision Physics of Simple Atomic Systems*; Springer: Berlin/Heidelberg, Germany, 2003; pp. 59–79.
78. Rodkin, D.M.; Tchuvil'sky, Y.M. Two-dimensional extrapolation procedure for an ab initio study of nuclear size parameters and the properties of the halo nucleus ^{6}He. *Phys. Rev. C* **2022**, *106*, 034305. [CrossRef]
79. Shen, S.; Elhatisari, S.; Lähde, T.A.; Lee, D.; Lu, B.N.; Meißner, U.G. Emergent geometry and duality in the carbon nucleus. *Nat. Commun.* **2023**, *14*, 2777. [CrossRef] [PubMed]
80. Li, H.; Ong, H.J.; Fang, D.-L.; Mazur, I.A.; Shin, I.J.; Shirokov, A.M.; Vary, J.P.; Yin, P.; Zhao, X.; Zuo, W. Ab initio study of Z(N) = 6 magicity. *Chin. Phys. C* **2024**, *48*, 124103. [CrossRef]

81. Shen, S.; Elhatisari, S.; Lee, D.; Meißner, U.-G.; Ren, Z. Ab Initio Study of the Beryllium Isotopes ^{7}Be to ^{12}Be. *Phys. Rev. Lett.* **2025**, *134*, 162503. [CrossRef]
82. Kotelnikov, I.A.; Milstein, A.I. Electron radiative recombination with a hydrogen-like ion. *Phys. Scr.* **2019**, *94*, 055403. [CrossRef]
83. Khlopov, M. What comes after the Standard Model? *Prog. Part. Nucl. Phys.* **2020**, *116*, 103824. [CrossRef]
84. Mack, G.D.; Beacom, J.F.; Bertone, G. Towards closing the window on strongly interacting dark matter: Far-reaching constraints from Earth's heat flow. *Phys. Rev. D* **2007**, *76*, 043523. [CrossRef]
85. Wandelt, B.D.; Dave, R.; Farrar, G.R.; McGuire, P.C.; Spergel, D.N.; Steinhardt, P.J. Self-Interacting Dark Matter. *arXiv* **2000**, arXiv:astro-ph/0006344.
86. Erickcek, A.L.; Steinhardt, P.J.; McCammon, D.; McGuire, P.C. Constraints on the interactions between dark matter and baryons from the x-ray quantum calorimetry experiment. *Phys. Rev. D* **2007**, *76*, 042007. [CrossRef]
87. Khlopov, M.Y. Composite dark matter from 4th generation. *Jetp Lett.* **2006**, *83*, 1–4. [CrossRef]
88. Niedermann, F.; Sloth, M.S. Radiation exposure from the dark. *Jcap Lett.* **2025**, *2025*, 042. [CrossRef]
89. Xu, W.-L.; Yang, J.M.; Zhao, J. Scattering of non-relativistic finite-size particles and puffy dark matter direct detection. *arXiv* **2025**, arXiv:2510.10641. [CrossRef]
90. Xu, X.; Farrar, G. Resonant scattering between dark matter and baryons: Revised direct detection and CMB limits. *Phys. Rev. D* **2023**, *107*, 095028. [CrossRef]
91. Dunsky, D.; Hall, L.J.; Harigaya, K. CHAMP cosmic rays. *J. Cosmol. Astropart. Phys.* **2019**, *2019*, 015. [CrossRef]
92. Akerib, D.S.; Al Musalhi, A.K.; Alder, F.; Almquist, J.C.; Amarasinghe, S.; Ames, A.; Anderson, T.J.; Angelides, N.; Araújo, H.M.; Armstrong, J.E.; et al. Search for New Physics via Low-Energy Electron Recoils with a 4.2 Tonne× Year Exposure from the LZ Experiment. *arXiv* **2025**, arXiv:2511.17350.
93. Abbamonte, P.; Albert, A.; Alves, D.S.M.; Anczarski, J.; Aralis, T.; Böhm, T.U.; Boyd, C.; Chen, J.; Chu, P.-H.; Cook, M.S.; et al. SPLENDOR: A novel detector platform to search for light dark matter with narrow-gap semiconductors. *arXiv* **2025**, arXiv:2507.17782. [CrossRef]
94. Dick, W.J.; Greenlees, G.W.; Kaufman, S.L. Search for Anomalous Isotopes of Sodium. *Phys. Rev. Lett.* **1984**, *53*, 431. [CrossRef]
95. Hemmick, T.K.; Elmore, D.; Gentile, T.; Kubik, P.W.; Olsen, S.L.; Ciampa, D.; Nitz, D.; Kagan, H.; Haas, P.; Smith, P.F.; et al. Search for low-Z nuclei containing massive stable particles. *Phys. Rev. D* **1990**, *41*, 2074. [CrossRef]
96. Verkerk, P.; Grynberg, G.; Pichard, B.; Spiro, M.; Zylberajch, S.; Goldberg, M.E.; Fayet, P. Search for superheavy hydrogen in sea water. *Phys. Rev. Lett.* **1992**, *68*, 1116. [CrossRef]
97. Mueller, P.; Wang, L.-B.; Holt, R.J.; Lu, Z.-T.; O'Connor, T.P.; Schiffer, J.P. Search for Anomalously Heavy Isotopes of Helium in the Earth's Atmosphere. *Phys. Rev. Lett.* **2004**, *92*, 022501. [CrossRef]
98. Aver, E.; Berg, D.A.; Hirschauer, A.S.; Olive, K.A.; Pogge, R.W.; Rogers, N.S.J.; Salzer, J.J.; Skillman, E.D. A comprehensive chemical abundance analysis of the extremely metal poor Leoncino Dwarf galaxy (AGC 198691). *Mon. Not. R. Astron. Soc.* **2022**, *510*, 3226. [CrossRef]
99. Brown, W.R.; Geller, M.J.; Kenyon, S.J.; Diaferio, A. Velocity Dispersion Profile of the Milky Way Halo. *arXiv* **2010**, arXiv:0910.2242v1. [CrossRef]
100. Belli, P.; Cerulli, R. Sensitivity of Solid-Scintillator Detectors to Dark Matter. *Physics* **2021**, *3*, 128–143. [CrossRef]
101. Cudell, J.R.; Khlopov, M.Y.; Wallemacq, Q. The nuclear physics of OHe. *Bled Work. Phys.* **2012**, *13*, 10–27.
102. Bikbaev, T.; Khlopov, M.; Mayorov, A. Quantum Mechanical Numerical Model for Interaction of dark atom with Atomic Nucleus of Matter. *Physics* **2025**, *7*, 8. [CrossRef]
103. Scamps, G.; Lacroix, D.; Adamian, G.G.; Antonenko, N.V. Polarization of the nuclear surface in deformed nuclei. *Phys. Rev. C* **2013**, *88*, 064327. [CrossRef]
104. Balashov, V.V. *Quantum Theory of Collisions: A Textbook*, 3rd ed.; Moscow University Press: Moscow, Russia, 2023; p. ill.
105. Davydov, A.S. *Theory of the Atomic Nucleus*; Nauka: Moscow, Russia, 1958. (In Russian)
106. Bernabei, R.; Belli, P.; Bussolotti, A.; Cappella, F.; Caracciolo, V.; Cerulli, R.; Dai, C.J.; d'Angelo, A.; Di Marco, A.; He, H.L.; et al. First model independent results from DAMA/LIBRA–phase2. *Nucl. Phys. At. Energy* **2018**, *19*, 307–325. [CrossRef]
107. Bernabei, R.; Belli, P.; Cappella, F.; Caracciolo, V.; Cerulli, R.; Dai, C.J.; d'Angelo, A.; Di Marco, A.; He, H.L.; Incicchitti, A.; et al. Improved model-dependent corollary analyses after the first six annual cycles of DAMA/LIBRA–phase2. *Nucl. Phys. At. Energy* **2019**, *20*, 317–348. [CrossRef]